Doctoral Dissertation
Doctoral Program in Electrical, Electronics and Communications Engineering
(33^{rd} cycle)

Smart Electronic Pen for Continuous Monitoring of Anaesthetics

Simone Aiassa
* * * * * *

Supervisors
Prof. Danilo Demarchi, Supervisor
Prof. Sandro Carrara, Co-supervisor

Doctoral Examination Committee:
Prof. Roland Thewes, Referee, Technical University of Berlin
Prof. Sara Ghoreishizadeh, Referee, University College London
Prof. Gabriella Olmo, Politecnico di Torino
Prof. Jun Ohta, Nara Institute of Science and Technology
Prof. Alena Simalatsar, University of Applied Sciences and Arts Western Switzerland Valais

Politecnico di Torino
May 19, 2021

I hereby declare that, the contents and organisation of this dissertation constitute my own original work and does not compromise in any way the rights of third parties, including those relating to the security of personal data. Content and images included in this work may be extracted by original author publication, in agreement with copyright and permission of each publisher, please, refer to Section 1.4 and Table 1.1 for a detailed reference list. All the images credit its original author in the caption, in agreement with the copyright and permission of each author.

. . . . . .

Simone Aiassa

Torino, May 19, 2021

A Iva

Summary

General anaesthesia is a challenging medical procedure inducing a reversible state of unconsciousness in patients during surgery to facilitate operations. The sedation is achieved by infusion of a perfectly balanced cocktail of pharmacological compounds. The delivery rate of this cocktail has to be continuously monitored to achieve and maintain the desired level of sedation to avoid complications and side effects related to over-dosage or under-dosage. Today, PharmacoKinetics and PharmacoDynamics (PK/PD) models regulate, via Target Controlled Infusion (TCI) pumps, the delivery of anaesthetics, and the patient is continuously monitored via BiSpectral (BiS)-index, a weighted sum of ElectroEncephaloGraphic (EEG) features. This approach comes with some limitations since PK/PD models are only statistically accurate since they are experimentally derived from observation on a population of individuals, and EEG suffers from measurement artifacts.

To overcome these limitations, we propose to close the loop between anaesthesiologist and patient with Therapeutic Drug Monitoring (TDM). Continuous monitoring of anaesthetics infusion helps anaesthesiologists to define personalized dose towards safer surgery. This thesis presents a newly required different part of the system to keep under control the concentration of anaesthetics in the body of the patient, which it was missing up today: the smart electronic pen for continuous monitoring of anaesthetics. Namely, the pen includes in a single device a unique electrochemical sensor, leveraging on new measurement methods, in a custom embedded device. The sensor built is a needle-shaped electrochemical cell fully characterized for direct detection of anaesthetics (propofol) in undiluted human serum. Several methods are specially developed in this thesis, including Sampling Rate Optimization (SRO), Total Charge Detection in Cyclic-voltammetry (TCDC), and Propofol Fouling Machine-learning (PFM) smart processing. The proposed device is a battery-operated single Printed Circuit Board (PCB) with wireless communication. It includes a novel quasi-digital potentiostat in a pen-shaped case for easy use in the surgery room.

The proposed smart electronic pen achieves the four primary goals as required towards a closed-loop system for TDM of anaesthetics: portability, real-time detection, automatic smart processing, and continuous monitoring. The developed technology is low-power, wireless, and small size compared to the state-of-the-art

to facilitate mobility into the surgery room. The system provides real-time detection with the first needle-shaped propofol sensor. Moreover, and for the first time in this work, machine learning approaches successfully compensated non-linearities of the electrochemical sensor, allowing smart processing. Finally, the sensor, methods, and electronics introduced in this thesis allow continuous monitoring of anaesthetics.

Acknowledgements

This work was supported by Politecnico di Torino and Compagnia di San Paolo under the initiative "Joint research projects with top universities". I would like to thank my supervisors, Danilo Demarchi and Sandro Carrara, for their invaluable supervision, support, and constant pushing. Francesca Stradolini, Abuduwaili Tuoheti, Ivan Ny Hanitra, and Francesca Criscuolo worked with me on this project, and I must share with them this result. I would like to thank Giovanni De Micheli, who kindly hosted me in his lab, and Maurizio Martina, who always believed in me. I also thank Paolo Motto Ros and Alessandro Sanginario for their mentorship and friendly help. My appreciation goes out to my colleagues, Umberto Garlando, Fabio Rossi, Rossana Terracciano, all the Mines, and VLSI-lab members who shared with me this path. Thank you Eleonora Testa, Giovanni Resta, Giulia Meuli and LSI family for all the time spent together. Finally, I must acknowledge all the students who worked on this project, who made this thesis possible, Francesco Grassi, Davide Tunzi, Gabriele Sandri, José David González Martínez, Sinan Yilmaz, and Tiberiu Totu.

Contents

List of Figures

List of Tables

List of Acronyms

ADC	Analog to Digital Converter
ANN	Artificial Neural Network
APAP	N-Acetyl-Para-AminoPhenol, paracetamol
BIS	BISpectral index
BLE	Bluetooth Low Energy
CA	Chrono-Amperometry
CE	Counter Electrode
CMOS	Complementary Metal Oxide Semiconductor
COTS	Commercial-Off-The-Shelf
CV	Cyclic Voltammetry
DAC	Digital to Analog Converter
DBS	Dried Blood Spot sampling
DC	Duty Cycle
DOA	Depth Of Anaesthesia
DPV	Differential Pulse Voltammetry
EEG	ElectroEncephaloGram
FPGA	Field Programmable Gate Array
FSCV	Fast Scan Cyclic Voltammetry
GA	General Anaesthesia
GATT	Generic ATTribute profile
GPIO	General Purpose Input/Output
GUI	Graphical User Interface
LOD	Limit of Detection
LOQ	Limit of Quantisation
MCU	MicroController Unit
MEC	Minimum Effective Concentration
MEMS	MicroElectroMechanical Systems
ML	Machine Learning
MPA	Multiple Pulsed Amperometry
MTC	Maximum Tolerated Concentration
OCP	Open-Circuit Potential
OTA	Operational Transconductance Amplifiers

PBS	Phosphate Buffer Saline
PCB	Printed Circuit Board
PD	PharmacoDinamics
PGE	Pencil Graphite Electrode
PK	PharmacoKinetics
PPM	Pulse Position Modulation
PWM	Pulse Width Modulation
QD	Quasi Digital
QDE	Quasi Digital stream of Events
RBF	Radial Basis Function
RE	Reference Electrode
RTC	Real-Time Counter
RTD	Resistance Temperature Detector
SC	Switch Capacitors
SEM	Scanning Electron Microscope
SMD	Surface Mount Technology
SNR	Signal to Noise Ratio
SPE	Screen Printed Electrode
SR	Scan Rate
SVM	Support Vector Machine
TCDC	Total Charge Detection in Cyclic voltammetry
TCI	Target Controlled Infusion
TDM	Therapeutic Drug Monitoring
TIA	Trans-Impedance Amplifier
TIVA	Total IntaVenous Anesthesia
VDCM	Variable Duty-Cycle Method
VF	Voltage Follower
WE	Working Electrode

Chapter 1

Introduction

In healthcare industries, personalised medicine is taking great relevance. Personalised medicine aims to revolutionary transform the medical practices with a patient's personalization of therapies since the variability in response to drugs is determined by numerous personal factor [1], providing the correct drug with dose and timing tailored to the patient [2]. In this framework, general anaesthesia is a necessary surgery medical procedure that requires the administration of a perfectly balanced cocktail of drugs: hypnotic, analgesic, and muscle relaxant [3]. The usage of prediction models to estimate the proper dosage presents today high errors due to the patient's diversity. Differently, the Therapeutic Drug Monitoring (TDM) aims to measure the actual drug concentration in the patient's body to meet the personal requirements with a dynamic adjustment of the anaesthetics infusion [4]. The need for TDM of anaesthetics opens the demand for systems for direct, continuous, in-situ measurement of the concentration of anaesthetics [5]. Electrochemical investigation can be adopted to measure the typical therapeutic compounds (e.g., Propofol, Midazolam, and Paracetamol), and electrochemical techniques showed excellent capability in biomedical devices for direct determination of drugs. In this thesis, a complete and entirely novel system based on electrochemical techniques for the continuous monitoring of anaesthetics in TDM practices towards safer anaesthesia is developed and detailed.

Chapter 1 introduces the TDM techniques (Section 1.1), properties and advantages, and links it to the general anaesthesia (Section 1.2) and its current practice and limitation. Section 1.3 depicts a general overview around biosensors and electrochemical sensors as best candidates as a set of sensors and methods for detecting anaesthetics. The full outline and the main research contribution are underlined in Section 1.4.

1.1 Therapeutic Drug Monitoring

PharmacoKinetics (PK) is the study of the interaction of a drug with a living organism in pharmaceutics. The metabolism of a patient processes the substance way before it reaches the target site since phenomena of absorption, distribution, molecular catalysis, and excretion occur [6]. Figure 1.1a represents a graphical example of the PK model. It is essential to define the Minimum Effective Concentration (MEC) and the Maximum Tolerated Concentration (MTC) in pharmacokinetics. The drug concentration should always remain between these two values to consider beneficial the drug's effect in the so-called therapeutic range. Under the MEC, the drug efficacy is not beneficial, while over MTC, the drug is toxic [7].

PK expresses the relation between the quantity of drug injected in a given patient's body (the dose) and the quantity of drug reaching the pharmacological target. On the other hand, PharmacoDynamics (PD) describes the relationship between the drug concentration and the out-coming effects once the substance reached the target, as presented in Figure 1.1b. Under stationary pharmacokinetic conditions, the pharmacodynamics may describe with low uncertainty the drug's effect on patients. The most common mathematical PD models are, for example, linear model, long-linear model, fixed effect model, Emax-model, and sigmoid Emax-model [8]. In most cases, the PK conditions are not stationary, and more complex models are required to consider the dissociation between dose-concentration and observed effect.

The combination of pharmacokinetics and pharmacodynamics is the PK/PD model, which is generally a set of mathematical equations describing the pharmacological effect of a single drug administered dose in time, as shown by Figure 1.1c. The PK/PD model establishes the dose-concentration/drug-response relationships in the attempt of predicting the behaviour in time of the drug dose, indicating the time-course of a drug and its real benefit [9]. PK/PD-modelling is essential during the drug development process. Moreover, PK/PD may be used to predict, adjust, and optimise patients' treatments in pharmacotherapy [8].

TDM, in general, is the measurement of a chemical or physical parameter that is directly related to the clinical effect of a specific prescribed drug in a patient under cure [4]. TDM is in strict relation with PK, PD, and PK/PD models. The primary scope is the efficacy assessment and the safety of drugs in clinical settings to provide patients with optimal therapies. The TDM introduced in the seventies a mathematical approach to link pharmacokinetics and patient outcome [10]. In the beginning, the drug monitoring practices were encouraged by increasing awareness in the relation between drug concentration and its effect that corresponds to the mapping of drug pharmacokinetic characteristics [11]. Nowadays, the TDM is still encouraged by the massive growth in computing performances that had been seen in recent years [12]. Finally, the advent of point-of-care, easy to use and cheap biosensing technology will bring TDM towards the next stage of clinical practice in

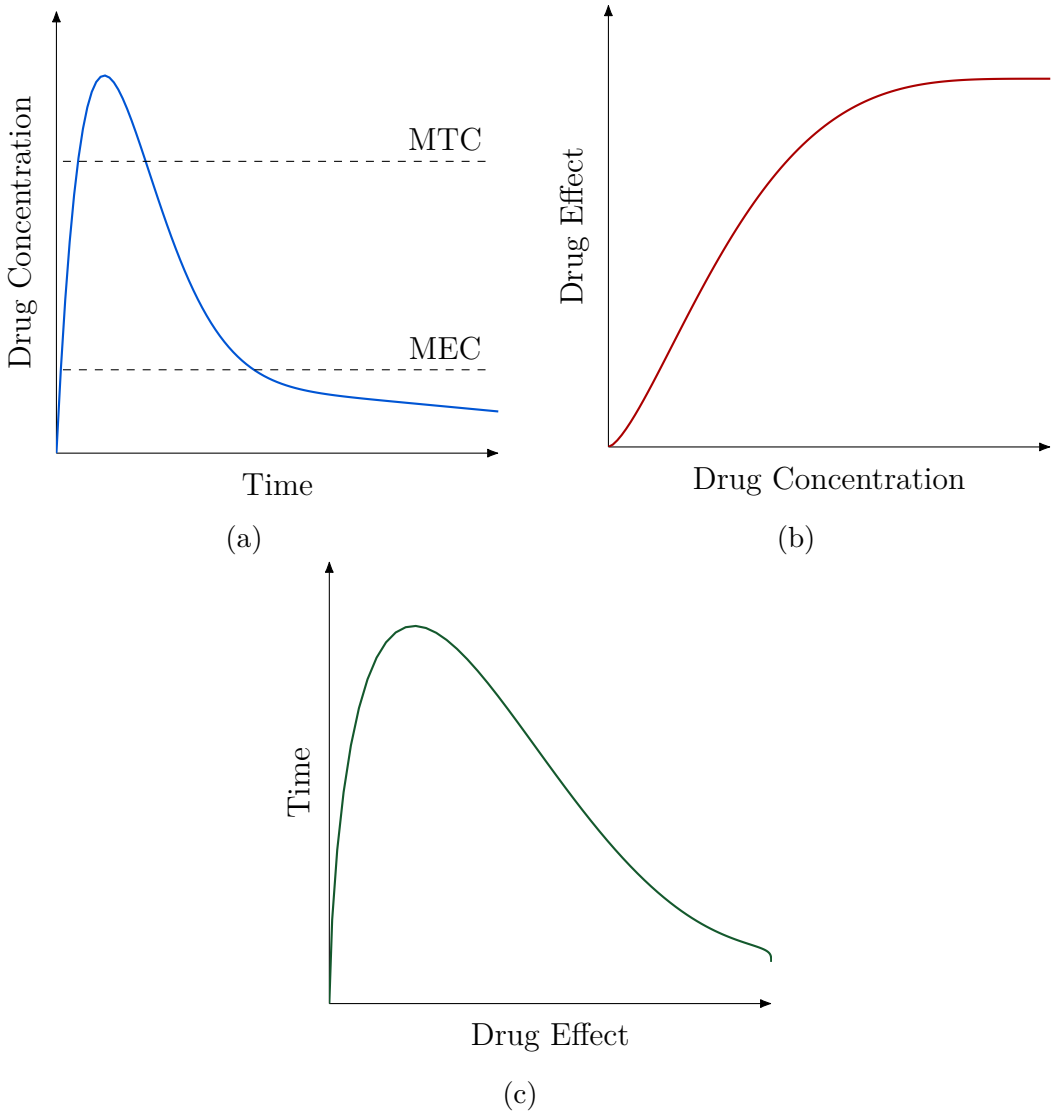

Figure 1.1: PK model (a) and PD model (b), may be combined to obtain the PK/PD model (c).

the future [13].

Since the generality of the definition of TDM, this approach refers to several different techniques to relate the therapeutic effects of drug monitoring. TDM was be exploited in monitoring the long-time effects of drugs, measuring so the outcome of drugs on a weekly or monthly basis for long-time treatments. For example, TDM is seen as a tool for clinical consultations helped patients with juvenile myoclonus epilepsy treated with antiepileptic drugs [14], and [15] reported the case of a patient affected by cerebral aspergillosis safely TDM-based treated with high-dose voriconazole for over one year.

Another aspect of TDM is referred to for the sake of this thesis. In fact, TDM also refers to the personalisation of the drug dose by continually maintaining the blood drug concentrations inside the therapeutic window. With this approach, it is possible to develop an automatic system that can continuously control the feedback loop of the dosage of drugs. Worth noting that, as previously mentioned with the introduction of PK and PD models, the quantity of drug inserted in the vein of patients (by syringe or similar instruments) is not the actual dose concentration reaching the target site. The relation between the effect and dose may vary in time according to several physiological phenomena. The direct control of drug concentration in-situ (for example, in the bloodstream) may provide an efficient application of TDM systems for personalised medicine [16]. For example, in cancer therapies, new TDM algorithms of patients' dose adjustment to reduce side-effect and optimise primary effects were investigated for several cytotoxic cancer drugs like methotrexate, busulfan, and 5-flurouracil [17]. Critically ill patients were cure through TDM-guided continuous infusion of piperacillin/tazobactam to cure sepsis with early antibiotics treatments [18]. Real-time monitoring of sedative drug concentrations (such as midazolam and sufentanil) was proved to be beneficial to avoid inadequate sedation and its complications in intensive care units for mechanically ventilated patients [19].

1.2 General Anaesthesia

The word anaesthesia can be translated by ancient Greek to *loss of sensation*. Anaesthesia refers to a temporary and reversible state of unconsciousness induced by drugs to patients to avoid their response to external stimuli or pain. Three different types of anaesthesia exist, which are local anaesthesia, sedation, and general anaesthesia.

- Local anaesthesia inhibits just part of the body of the patient. The goal is to avoid pain in the target area without losing consciousness. It is generally applied in all cases when it is possible to reach the nerves by sprays, drops, ointments, or injections. Regional anaesthesia refers to local anaesthetics injected near the nerves that supply a larger or deeper body area. Spinal and epidural injections can be used for operations on the lower body.
- Sedation is a weak suppression of the nervous system. A small amount of anaesthetics makes the patient mentally and physically relaxed, in a sleep-like state, without consciousness loss.
- General Anaesthesia (GA) is a state of controlled unconsciousness. The patient is not able to feel or remember what is surrounding him. The anaesthetic drugs are injected into a vein, or anaesthetic gases are administered by inhalation. The GA is essential for a huge variety of operations, and it is the most

Figure 1.2: Team of surgeons performing operations on anaesthetised patient. Designed by wavebreakmedia_micro/Freepik. Reprinted with permission.

challenging type of anaesthesia since it is not possible to receive feedback from the patient.

In GA, two different types of sedation exist; inhalation anaesthesia and Total IntaVenous Anesthesia (TIVA). In TIVA, the GA is induced with a combination of anaesthetic agents administered through intravenous injection. It was firstly reported to have been practice by G. von Wahrendorff in 1642, injecting opium in the veins of a dog, and in the 1660s, J. D. Major and J. S. Elsholtz tested it for the first time on a human [20]. These experimental injections were not successful, and only in the 1800s the injection of anaesthetics starts to been used successfully. During twenty century the inhalation anaesthesia has been preferred against TIVA since the respiratory route of administration allows rapid and convenient adjustment [21]. Nevertheless, over the last thirty years, this situation had been changed thanks o the advent of new technologies. Those changes have transformed TIVA into an attractive alternative to more traditional inhalation anaesthesia methods [22], the reason why this thesis focuses only on TIVA GA.

The sedation is obtained by a precise and controlled mix of drugs. While many drugs can be used intravenously to produce anaesthesia or sedation, the most common are barbiturates, benzodiazepines, and propofol. The concentrations of these compounds must be accurately maintained in the patient's body avoiding side effects [23]. Barbiturates, like thiamylal, thiopental, presents ultra-short-acting and are rarely used in anaesthesia. In GA, the preferable benzodiazepine is midazolam. Etomide and ketamine are used as anaesthetics only in emergency settings

and with sick patients because it produces fewer adverse physiological effects while presenting unpleasant experience for the patient, with vivid dreaming and illusions on top [24]. Propofol (2,6-diisopropylphenol) is a highly lipophilic hypnotic agent commonly administered to induce and maintain anaesthesia, which ensures fast and predictable time of effect [25]. It produces its hypnotic action by an augmentation of the inhibitory function of the synaptic transmission binding with the receptors of the gamma-amino-butyric acid, which are typically involved in the regulation of anxiety, vigilance, memory, and muscle tension and are the most abundant fast inhibitory neurotransmitter receptors [26]. Propofol is today the golden standard in anaesthesiology, it is a widely adopted anaesthetic [27], and it is considered the preferable solution with respect to inhalations drugs in general anaesthesia [28].

Propofol, barbiturates, and benzodiazepines do not present any pain-relieving properties, and it is required to mix them with analgesics [24]. While opioids can produce unconsciousness, they do so unreliably. With significant side effects [29], they are so frequently used in combination with anaesthetics to relieve the pain of patients before, during, or after surgery. Fentanyl is the most commonly used opioid in GA. Acetaminophen, also known as paracetamol (APAP) (N-acetyl-p-amino-phenol), is a largely used analgesic and antipyretic drug. It can increase the pain threshold, inhibiting the cyclooxygenase isoforms, which are involved in the synthesis of the prostaglandins [30]. It is highly recommended ad analgesics due to its light side effects. Paracetamol is often administered in place of opioids to alleviate the so-called pain of propofol injection that still affects 90 % of patients [31].

The last component of the anaesthetic cocktail is the muscle relaxant, a neuromuscular blocking drug used after a patient is rendered unconscious to facilitate intubation or surgery by paralysing skeletal muscles [32]. Those practice is starting to be limited since recent studies had shown that the use of neuromuscular blockers during general anaesthesia is associated with an increased risk of postoperative pulmonary complications [33]. The most common cocktail of drugs in anaesthesia is so composed of:

- Anaesthetic: propofol.
- Analgesic: paracetamol.
- Muscle relaxant: midazolam.

Worth noting that propofol and paracetamol are used in combination, and propofol is the most dangerous compound in this cocktail, leading to Michael Jackson's death in 2009 [34], among many other cases. For those reasons, this thesis mainly focuses on paracetamol, propofol, and their interaction.

1.2.1 Risks of Anaesthesia

Anaesthesia, especially GA, presents temporary and less severe side effects like confusion and memory loss. However, this is more common in the elderly, dizziness, difficulty in urination, bruising or soreness, nausea and vomiting, shivering, and feeling cold. The side effects are related to possible unbalance in the composition of drugs infused in the patient's body. Figure 1.3 shows the most common side-effects associated with errors in the determination of the cocktail of drugs.

Most of the patients experience at least one of these side effects [38], but those phenomena tend to occur straight after the anaesthesia. Otherwise, a study analysed the case of claims reported in the US, highlighting that most frequent injuries claimed after anaesthesia were death (18.3 %), pain (10.9 %), organ damage (12.7 %), nerve damage (13.5 %), teeth damage (20.8 %) [39].

Unintended intraoperative awareness is a rare state of awareness during surgery, with an incidence of 0.02 % [40]. In those cases, patients are conscious of the environment, and in some cases, they are feeling pain, and due to the effects of the muscle relaxants, they cannot signal their state of consciousness. This traumatic

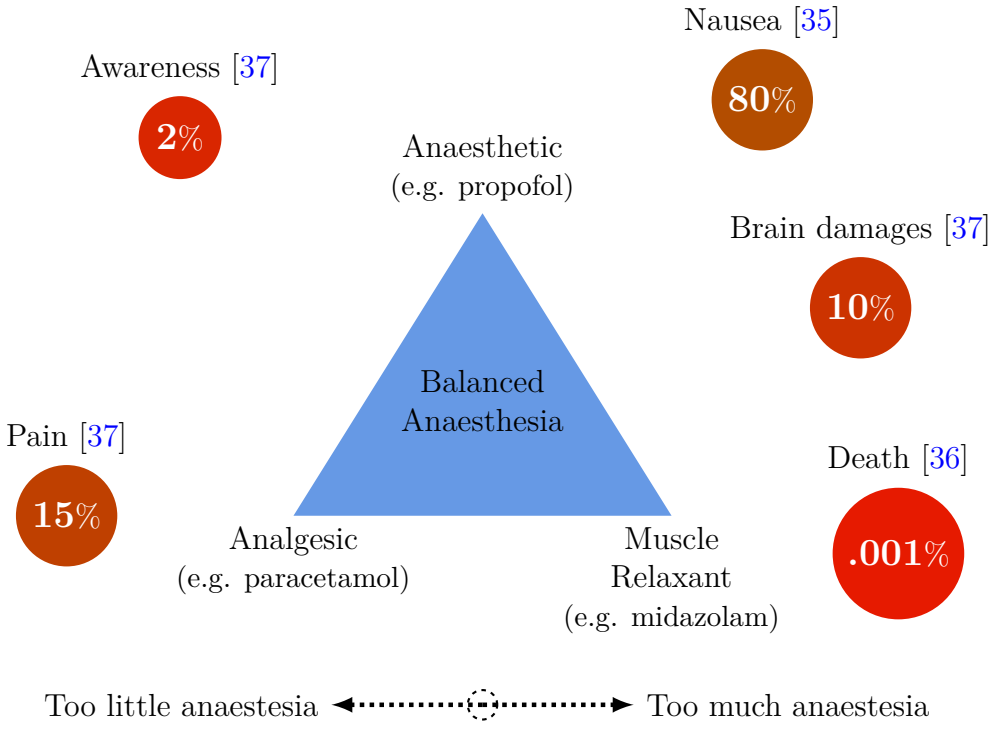

Figure 1.3: The anaesthesia is based upon a perfect balance of drugs and the most common side-effects are directly related to over/under dosage estimation. Data from [35, 36, 37].

event sometimes leads to psychological or psychiatric consequences, such as post-traumatic stress disorders [41]. The general sense of pain is a less severe undesired effect related to under-dosage of anaesthetic compounds and has been reported to occur quite frequently, in around 15 % [37]. While unintended intraoperative awareness and pain are related to under-dosage, overdosing must also be prevented to avoid serious GA complications. These effects range from postoperative nausea, which is the most common effect of anaesthesia, to critical ones like brain damage and death, which are, luckily, extremely rare. Vomiting, or at least experiencing nausea, is extremely common after GA. Namely, it has been reported by 80 % of the patients [35]. The death rate is hardly evaluated due to the difficulties of forensic pathology to distinguish between deaths related or unrelated to anaesthetics [42]. Recent studies had been reported that the risk of death for anaesthesiology malpractices is approximately 0.001 % in patients with moderate systemic diseases [36].

1.2.2 Current Practices and their Limitation

Nowadays, the increase in popularity of TIVA is related partially to the improvement of PK/PD models for the drugs used in GA. Meanwhile, the real driving force of this change is the technological advance in infusion pumps. Target Controlled Infusion (TCI) pumps incorporate hardware and software to control the anesthesia automatically. TCI follows a mathematical model to approximate and predict the concentration of drugs in the plasma. The software elaborates an advanced algorithm based on the PK model of the target drug, allowing dynamic drug-dosage adjustments to achieve and maintain a certain level of sedation in the patient [43]. A loading bolus dose is given first to achieve a desired drug concentration at the target site. The infusion rate helps in maintaining a steady-state plasma concentration of the drug [44]. The TCI system estimates the initial bolus dose and calculates the duration of subsequent infusion to maintain the desired concentration [45]. TCI pumps for propofol leverage on two mathematical models to estimate the drug evolution: the Marsh model and Schnider models. Both models contain numerous parameters; some considered fixed, other variables according to the patient's age, patient's total weight, lean body mass, and height [45].

Today, prediction models represent the golden standard to estimate the proper dosage of anaesthetics, but they still show high errors due to the patient's heterogeneity [46]. Even if TCI systems are commercially available and widely used to administer anaesthesia, they still present some limitations. In fact, all TCI pumps implement PK/PD models, which are experimentally derived from observation of drug effects on a population of individuals being so only statistically accurate. They cannot reproduce all the interaction presents in the body of any individual. Therefore there will always be patients with a metabolism unpredicted by the TCI pump [47].

Figure 1.4: BIS index system monitoring a patient under anaesthesia. Reprinted with permission from [49]. "Hybrid intelligent system to perform fault detection on bis sensor during surgeries" from J.-L. Casteleiro-Roca et al. is licensed under CC BY 4.0.

The Depth Of Anaesthesia (DOA) is the metric to express the patient's anesthesia. One of the main challenges in TIVA practices is DOA evaluation and its monitoring. According to the individual response, the accurate assessment of DOA may improve anaesthesiology practice, helping to calibrate the delivery of anaesthetics. ElectroEncephaloGram (EEG) signal has been investigated as an indicator of DOA since most common anaesthetics have an inhibitory effect on brain receptors leading to a progressive diminution of the EEG activity with increasing drug concentrations [48]

One of the most widely used indices for DOA monitoring in Europe is the so-called BiSpectral index (BIS), introduced in 1994 by Aspect Medical Systems [50]. The BIS index is a weighted sum of several EEG parameters. Namely, BIS is evaluated statistically, combining the contribution of key EEG signal features (bispectral analysis and others) recorded every 15 s or 30 s [51]. The BIS index ranges

between zero and one hundred, where one hundred means the patient is awake, while zero represents that the EEG signal is iso-electric. The sedation is performed maintaining the BIS over a value of seventy, while to ensure hypnosis in GA, the BIS is maintained between forty-five and sixty [52]. Even though BIS monitoring is a widely used DOA monitoring tool, which helps the anaesthesiologist regulate the anaesthesia dosage in induction, maintenance, and emergence phases, the BIS index still presents some limitations. Indeed, the relation between DOA and BIS is not uniform in patients, artefacts highly influence the evaluation of BIS with EEG, and the measuring introduces a high latency [53].

1.3 Biosensors and Electrochemical Sensors

Biosensor refers to a variety of devices able to detect or measure biological compounds for monitoring concentrations of biomolecules, typically for applications in medicine [54], environment monitoring [55], or in production-control or quality-control in industry [56], water quality measurements, prosthetic devices, and drug discoveries [57]. The term biosensor defines a device that combines a biological component with a physicochemical system for the detection of a chemical substance [58]. Namely, the biosensor outputs the presence and the quantity of the target molecule [59].

Biosensors provide low-cost, efficient, and easy-to-use devices for fast measure and monitoring of patients [60, 61]. According to the definition, the world of biosensors is an extensive collection of devices intimately integrating a biological system (e.g., a protein) with a physical substrate typically required by the sensing used technique, which exploits different working principles depending on the different target molecules [62, 63]. Just to list some examples, biosensors could leverage on electrochemistry [64], acoustic techniques [65], surface plasmon resonance [66], or luminescent principles [67]. Much work has been done on metabolites sensing, and it was possible to identify human pathogen through real-time in vitro metabolites detection [68]. For example, a composite modified glassy carbon electrode was proposed to determine the presence of an amino acid essential in neuroregulation (Tryptophan) [69]. Electrochemical methods allow the detection of beta-amyloid peptides and aggregates [70], and peptides were used to functionalise the sensor surfaces to detect antibodies [71]. In Microelectromechanical Systems (MEMS) technologies, assay system based sensor helps in rapid analysis of C-reactive proteins [72]. MEMS are indeed a significant breakthrough because they enable fast detection of several biomarkers [73, 74]. MicroRNAs gained consideration due to their importance in early-stage diagnosis [75]. This section is adapted with permission from Springer Nature Customer Service Centre GmbH: [76] © 2020 Springer Science Business Media.

This thesis focuses on sensing technologies for drugs, in particular electrochemical sensors and amperometric techniques. Recent years had shown a grown in the interest in this type of sensors, which are easier to cope with standard electronics and low-cost electronic devices. Glucose sensors are one of the most popular analytes in the scientific literature, and today glucose sensors are occupying around 85% of the biosensor market [77]. In those decades, the efforts done on glucose detection brought significant scientific and technological innovations in the continuous monitoring of diabetes [78]. Today, the technology is pushing towards the limits to develop drinkable technology sub-millilitre size [79]. These efforts and the results of this application encourage the researcher to develop new technology based on this innovation for helping and contributing to the monitoring of other diseases and medical procedures.

In pharmaceutical applications, several electrochemical sensors have been presented for the detection of pharmacological compounds and drugs. Bioelectrodes nanostructured with multi-walled carbon nanotube and gold nanoparticle presented high sensitivity and limit detection in measuring electroactive etoposide anti-cancer drug [80]. Another anti-cancer drug, 5-fluorouracil, has been detected with a silver nanocomposite-based electrochemical sensor [81]. Recently, a nanostructured silver doped electrode was presented as a sensor for the detection of cetirizine anti-inflammatory drug [82]. Anti-anginal drugs have been detected with a sensor coated with graphene nanocomposite material [83]. Also, antibiotics, in particular Ofloxacin drug, have been detected in urine samples [84]. Again multi-walled carbon nanotubes electrochemical sensor has also been used to detect anti-malarial drug [85]. Section 2.1 presents detailed state-of-the-art sensors designed for the detection and measurement of anaesthetics.

1.3.1 Electrochemical Techniques

The electrochemical reaction occurs in the electrochemical cell, consisting of electronic conductors (electrodes) immersed in an ionic conductor (electrolyte). The most common configurations of the electrochemical cells are with two electrodes (Figure 1.5a) and with three electrodes (Figure 1.5b). In the two-electrode configuration, the electrochemical cell comprises one Working Electrode (WE) and one Reference Electrode (RE). It is possible to add the auxiliary electrode or Counter Electrode (CE), creating the three-electrode configuration.

The electrochemical reaction may exhibit a current flowing due to an applied potential, and it is composed of two components, non-Faradaic and Faradaic. The non-Faradaic current is related to a displacement of charge, while the Faradaic current takes place from oxidisation or reduction of solution species. The overall chemical reaction in the cell is based on two half-reactions happening at the interface between electrode and electrolyte, as a consequence of the potential difference. The WE is the electrode at which half of the reaction occurs, while the

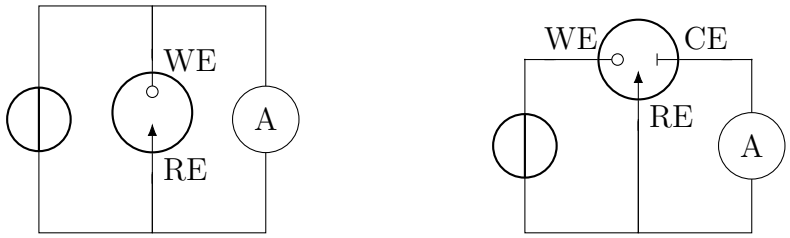

(a) (b)

Figure 1.5: The electrochemical cell, with two electrodes (a) and three electrodes (b); the addition of Counter Electrode (CE) is required to detect current while driving the voltage across Reference Electrode (RE) and Working Electrode (WE).

RE maintains a fixed and known potential to standardise the other half of the cell. Controlling the potential across WE and RE and driving it to negative potentials, the energy of electrons increases up to a higher level where it will be transferred from the electrode to the electrolyte. In this case, a reduction current from the electrode to the solution occurs. On the other hand, if the energy of electrons is decreased by imposing a more positive potential, the electrons of the electrolyte will be energetically facilitated to flow from the solution to the electrode creating an oxidation current. In the two-electrode configuration, the RE acts both as an electron supplier and as a reference. For this reason, the addition of CE in the three-electrode configuration enables the current flows between the WE and the CE, avoiding any resistive current emerging from the potential applied between WE and RE [64]. Most importantly, eliminating the current on the RE electrode establishes better control on the potential supplied by WE.

The high stability of RE potential may be reached by creating a redox system with buffered or saturated concentrations. Commonly adopted aqueous reference electrodes are hydrogen-based, saturated calomel, copper-copper, and silver chloride [86]. A silver chloride electrode (Ag/AgCl) is a type of reference electrode commonly used in electrochemical analysis and measurements. This electrode has a smaller temperature coefficient of potential, it can be built compactly, and it has widely replaced the saturated calomel electrode for environmental reasons. The electrode functions as a redox electrode, and the equilibrium is between the silver metal (Ag) and its salt—silver chloride (AgCl). This aqueous electrode needs a glass chamber to contain the KCl solution. Ag/Ag+ RE might be preferred to avoid leakages. For limiting contamination in the test solution, bare metal wires (typically silver or platinum) as a pseudo-reference electrode are also widely adopted. The potential of Ag or Pt wires, although being not indeed known (for each RE), will not drift in time [64].

The CE is often fabricated from electrochemically inert materials. Moreover, to enhance current flow and avoid current density displacement, the counter electrode

needs to present a low resistivity. It has to be designed with an active area more extensive than the WE. This size difference ensures that the reaction takes place on the WE and the flow of electrons is facilitate passing through the CE, avoiding any accumulation of charge or potential inversion related to limited diffusion. Carbon, platinum, or gold best suited to be used as CE due to low resistivity and being inert materials. The WE is where all the game takes place. For this reason, the composition of the working surface may be diversified; it may present an infinite number of modified, coated, pretreated or enhanced types of material surfaces that this thesis would not be able to cover.

The potential of the cell, which corresponds to the potential difference between WE and RE can be expressed by the Nernst equation:

$$E = E_0 + \frac{RT}{nF} ln\left[\frac{C_{Red}}{C_{Ox}}\right] \tag{1.1}$$

where E_0 is the standard RedOx potential, R is the gas constant, T the absolute temperature, n the number of electrons exchanged in the RedOx reaction, F the Faraday constant, and C_{Red}, C_{Ox} are the concentration of the reduced and oxidised species, respectively. The RedOx equilibrium, which corresponds to the potential E, is achieved when the concentration of reduced species is equal to the concentration of oxidised species in open potential conditions (i.e., the potential E is not eternally driven). The concentration of the species C_{Red}, C_{Ox} may form a gradient due to a driving diffusion force transporting the analyte towards the electrode surface or the bulk solution. The Nernst equation describes the concentration gradient established between the solution near the electrode surface and the bulk solution depending on the applied potential. If a system follows the Nernst equation, the electrode reaction is often said to be thermodynamically or electrochemically reversible (or Nernstian) [87]

It is possible to combine Faraday's law of electrolysis (Equation 1.2) with Fick's first law of diffusion (Equation 1.3) and Fick's second law of diffusion (Equation 1.4) to briefly explain the phenomena happening at the electrode/electrolyte interface. Faraday's law of electrolysis describes the mass m according to the charge Q, the molar mass M, the Faraday's constant F, and the valence number z. Meanwhile, the first Fick's law expresses the flux J in relation to a gradient of concentration C in space and the coefficient of diffusion D of media. The second Fick's law predicts how diffusion causes the concentration to change with respect to time.

$$m = \frac{QM}{Fz} \tag{1.2}$$

$$J = -D\frac{\partial C(x,t)}{\partial x} \tag{1.3}$$

$$\frac{\partial C(x,t)}{\partial t} = \frac{\partial^2 C(x,t)}{\partial x^2} \tag{1.4}$$

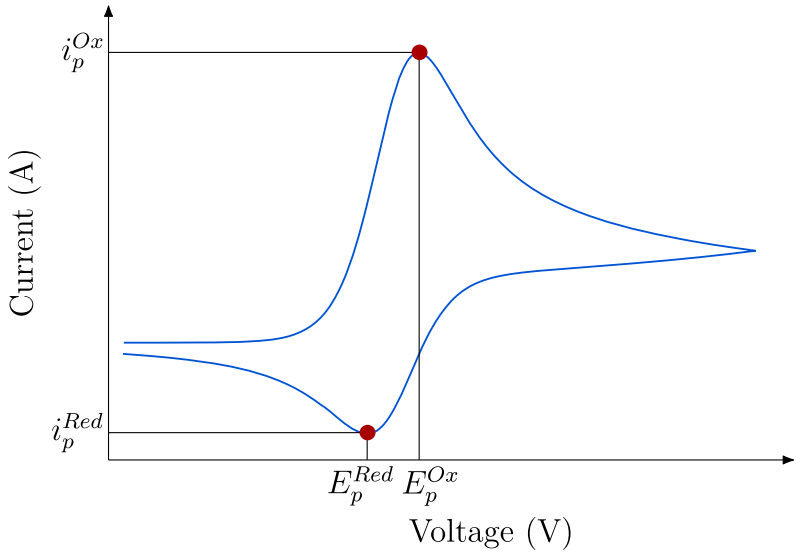

Figure 1.6: Example of cyclic voltammogram, the x-axis displays the voltage, while the y-axis the current. The voltammogram may presents a duck-shaped with oxidation and reduction peak, with i_p^{Ox} and i_p^{Red} current at E_p^{Ox} and E_p^{Red} equilibrium potential, respectively.

Combining Faraday's (Equation 1.2) and both Fick's laws (Equation 1.3, Equation 1.4), it is possible to express the current i flowing through the electrochemical cell proportionally to the initial analyte concentration C_0 according to the Cotrell equation [88]:

$$i = \frac{nFAC_0\sqrt{D}}{\sqrt{\pi t}} \tag{1.5}$$

where n is the number of electrons involved in the reduction/oxidisation of the target molecule, F is the Faraday's constant, A is the active area of WE, D is the diffusion coefficient, and t the time.

The so-called voltammogram is produced by applying a scan in the potential to the electrochemical cell. The voltammogram is one of the most popular visual representations of redox. It describes the electrochemical cell's behavior, depicting on the x-axis the input voltage and the y-axis the output current (Figure 1.6). Cyclic Voltammetry (CV) is a powerful electrochemical technique exploited to analyse oxidation and reduction processes [89]. The CV presents duck-shape and current peaks. The peak position is related to the equilibrium described by the Nernst equation (Equation 1.1). The Scan Rate (SR) describes how fast the applied potential is scanned. Higher currents are observed with higher SR due to a decrease in the size of the diffusion layer [89]. For electrochemically reversible electron transfer processes involving freely diffusing redox species, The Randles-Ševčík equation [90, 91]

expresses the peak current i_{peak} relating it to the concentration C of the analyte:

$$i_p = 0.4463 \cdot nFAC\sqrt{\frac{nFvD}{RT}} \tag{1.6}$$

As previously, n is the number of electrons involved, F is the Faraday's constant, A is the active area of WE, v is the SR, D is the diffusion coefficient, R is the gas constant, and T the temperature.

1.3.2 Electronics for Electrochemical Sensors

This thesis focus on amperometric sensing techniques. In this case, the potentiostat is the most important electronic component, which is the set of a circuit designed to drive the voltage between WE and RE and read the current flowing in the electrochemical cell (see Section 1.3.1). Figure 1.7 reports the two possible circuit implementations of a potentiostat for amperometric measurement on a three-electrode electrochemical cell. Namely, the grounded-WE (Figure 1.7a), grounded-CE (Figure 1.7b) topologies place the actual ground of the system connected to the WE, CE, respectively. All the different circuit implementation recall Figure 1.5b, moving the actual position of the electrical reference (the ground) only. In all the cases, the applied supply voltage V is forced between WE and RE nodes, and in all the cases, the target CE current i is measured detecting the flow of electrons between WE and CE. In both cases, the current on the node RE is forced to zero. The two different circuit implementations can be implemented using standard amplifiers or with more complex circuitry. The grounded-WE has been the most popular and most frequently used due to its simplicity of implementation through standard operational amplifiers. In contrast, grounded-CE has been primarily used in multi-electrode systems. The configuration with the ground connected to the counter electrode is the least implemented [92].

There are two types of potentiostat in practice: the first one is the potentiostat intended as a lab instrument and used as an analysis tool in a laboratory environment by a researcher. Meanwhile, the second one is the potentiostat designed as a circuit integrated into a sensor for direct detection. Figure 1.8 reports the basic circuit diagram of a standard commercial lab potentiostat, which drives and reads the cell taking into consideration the ideal electrochemical cell. As can be seen in Figure 1.8 (which is taken directly by the instrument data sheet [93]), the CE is connected to a control amplifier (CA) which forces current to flow through the cell. The current value is measured using a Current Follower (LowCF) or a shunt Current Reader (HighCR), depending on its level, low or high current, respectively. The potential difference is measured through a Differential Amplifier (Diffamp) between RE and S, usually shorted to WE. The four-electrode cell setup is rarely used in applications where it is required to measure the resistive potential difference between RE and S in well-defined interfaces. The signal is fed into the

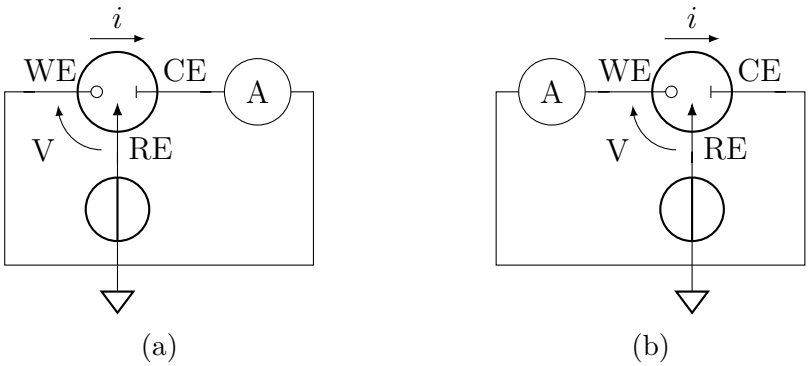

Figure 1.7: The two possible equivalent circuit implementation of a potentiostat: Grounded-WE (a), Grounded-CE (b).Namely, the only difference is the actual position of the electrical reference (ground).

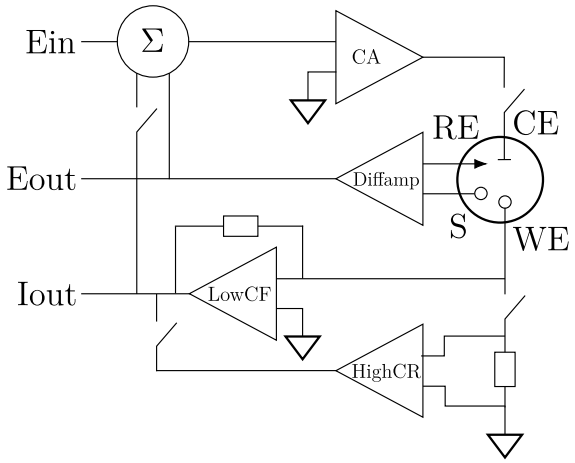

Figure 1.8: Basic circuit diagram of a commercial lab potentiostat/galvanostat from Methrom [93].

Summation Point (Σ), which, together with the waveform set (Ein), will be used as an input for the control amplifier [93].

Figure 1.9 reports the most common circuit implementation of a potentiostat for amperometric measurements to be integrated in an electronic device. In this case, only two operational amplifier may be used in the grounded-WE configuration (Figure 1.7a). The first operational amplifier (A_1) acts as voltage follower and drives the potential across the nodes WE and RE, forcing V_{in} on RE. The second amplifier (A_2) is the transimpedance amplifier. A_2 converts the current i to the voltage V_{out} according the equation:

$$V_{out} = i \cdot R_f \tag{1.7}$$

The target current (i) is the current exiting the CE in the electrochemical cell,

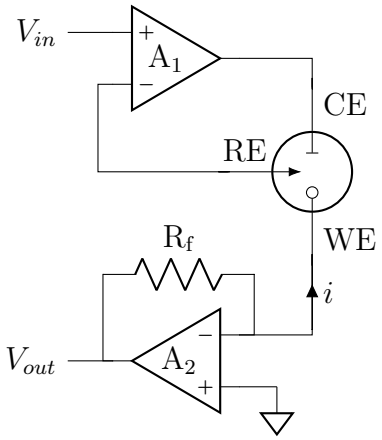

Figure 1.9: Basic circuit implementation of potentiostat integrated in a sensor for direct detection. A_1 drives the voltage V_{in}, while A_2 converts the current i into V_{out}.

and the circuit reproduces the one shown in Figure 1.7a. The voltage V_{out} may be easily sampled by an Analog to Digital Converter (ADC) to provide a fast read of the Faradaic current flowing in the electrochemical cell. The integrated configuration (Figure 1.9) requires a complete optimisation related to the properties of the electrochemical cell and the target analyte. Specifically, the circuit must be fully aware of the range of values of both the potential V_{in} and the current i.

1.3.3 Metrics and Design Goals

The design and the development of a sensor depend mainly on the requirements of the final application. Several metrics may be taken into account during the design. Selectivity, specificity, sensitivity, and Limit of Detection (LOD) are the most important, and they are taken into account in this thesis.

Selectivity and specificity Both selectivity and specificity are related to the ability of the sensor to distinguish the target analyte, among others. Selectivity covers more broadly the ability to determine one analyte among others selectively. Meanwhile, specificity is related to the unequivocal detection of a target in the presence of other expected components [94]. The most common assessment method of selectivity and specificity includes clinical trials and interference studies. The interference studies may be performed by testing the sensor with samples in which the most common interference analytes have been synthetically introduced [95].

Sensitivity Biosensor is composed of a transducer, which is the part of the sensor translating the input information (quantity of analyte) into an electrical signal [96].

The sensitivity express this relation. Most of the sensor presents a linear relationship between the concentration of the target molecule and the output electrical signal. In those cases, the sensitivity is represented numerically as the angular coefficient (slope) in the relation between concentration and electrical signal. The sensitivity must be taken into account during the design of the electronics of the sensor. If the sensitivity is too low, it may be hard to discriminate low concentrations of the analyte. For this reason, the sensitivity is strictly related to the limit of detection.

Limit of Detection The LOD is the minimum quantity of target analyte that a sensor can detect. Several methods to determine and characterise this value are available in the literature. In this thesis, according to the International Union of Pure and Applied Chemistry (IUPAC) standard, LOD is defined as:

$$LOD = \frac{3\sigma_{blank}}{S} \tag{1.8}$$

where σ_{blank} is the standard deviation from the signal obtained from the blank. Factor three maintains the required confidence level of 99.7 % between the observed signal and the blank response [97]. The blank is the solution in the absence of the target analyte.

The thesis uses those metrics to define and prove results. Many other figures of merit may be used to determine the capability of an electrochemical sensor, such as Limit of Quantisation (LOQ), linearity, and dynamic range. The focus on those features is low since partially related to the others. In the case of linearity, this thesis proves that not all the sensors must present a linear response in order to work correctly (see Section 3.4).

1.4 Thesis Outline and Research Contribution

Figure 1.10 presents the outline of this thesis. A completely novel piece of technology is required to close the loop between patient and anaesthesiology with TDM. In Chapter 2, the thesis describes the composition, design, and characterisation of new electrochemical sensors to detect drugs. These sensors are required to reliably detect and discover the concentration of anaesthetics present in the patient's body and act as a transducer converting the unknown concentration of drug into an electrical signal. Knowing and having developed the sensor, the next step is developing, optimizing, and validating measurement methods. These methods are discussed in Chapter 3, and they are necessary to understand how to transform a sensor for the detection of anaesthetics into a measurement device. Chapter 4, finally, describes and detail the design, hardware and software implementation of the proposed smart electronic pen and the embedded device, which copes with the new

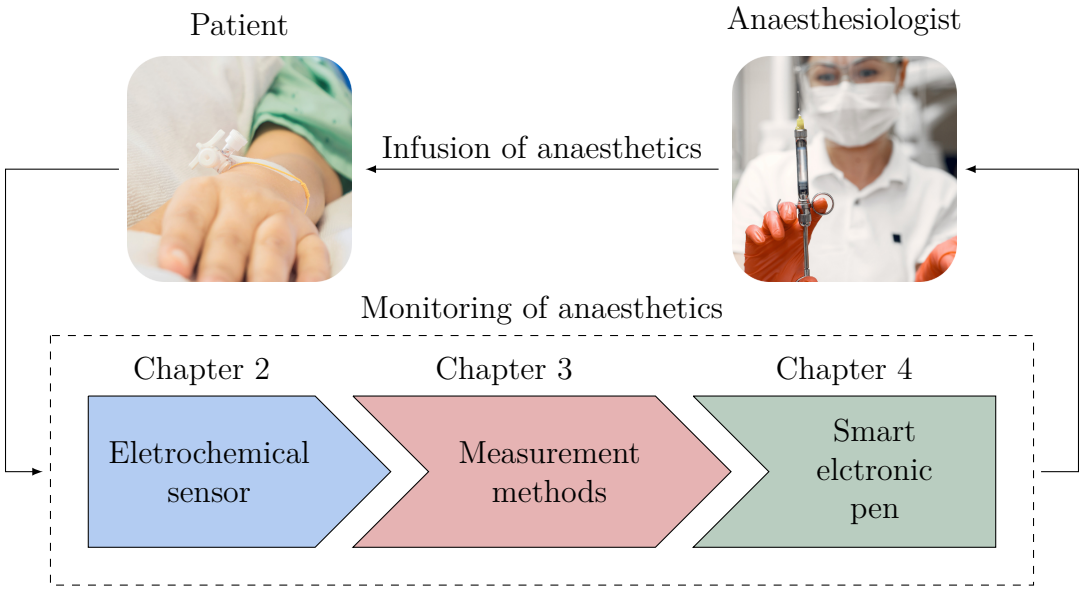

Figure 1.10: Thesis outline and research contribution. With a new electrochemical sensor (Chapter 2) and novel measurement methods (Chapter 3), an the smart electronic pen (Chapter 4) ready for monitoring of anaesthetics is developed. Designed by jcomp/Freepik and by prostooleh/Freepik. Reprinted with permission.

sensor and leverage on the novel methods. In all its part, the device is developed to enter a full system for continuous monitoring of anaesthetics.

In this thesis, several novelties are introduced and validated with respect to the state-of-the-art. Namely, the following goals are achieved in this thesis:

- **Portability**: the developed technology is low-power, wireless, and small size, in comparison with respect to the previously proposed electronics in the literature. Those improvements contribute to easy mobility into the surgery room, the proposed system's target environment.
- **Real-time monitoring**: in this thesis, the first needle-shaped sensor for detection of propofol in situ is presented for online monitoring of anaesthetics.
- **Continuous monitoring**: the sensors, the methods, and the electronics introduced, obtain together with the most important goal of this research: the capability of continuous monitoring. Readers will discover in this thesis the original device for continuous detection of anaesthetics, which provides stability in time the information requested to implement a TDM system for anaesthesiology practice.

Table 1.1: Table of correspondence between section of this thesis and published works.

Section	Reference
1.3 Biosensors and Electrochemical Sensors	[59, 76]
2.3 Needle-shaped Electrochemical Sensor	[98]
3.2 Sample Rate Optimisation	[99]
3.3 Total Charge Detection in Cyclic Voltammetry	[100]
3.4 Propofol Fouling Machine learning	[101]
4.2 Quasi Digital Potentiostat	[102, 103, 104]
4.3 Embedded Device	[105].

- **Smart and Automatic**: novel methods for intelligent and automatic detection of drugs are implemented in this thesis. For the first time, machine learning approaches resulted successfully in the compensation of non-linearities of the electrochemical sensor. Moreover, the intelligent classifier helps anaesthesiologist follow up with eyesight the infusion of anaesthetics.

All the claims of this thesis are proved and detailed by a series of academic publications. Table 1.1 presents the correspondence between published manuscripts and the content of the thesis. In detail, this thesis shows the following novelty that designed and implemented to achieve the goal of developing a complete system for direct and continuous detection of anaesthetics:

1. **Needle-shaped sensor**: to target the direct detection of anaesthetics direct in human serum.

2. **Sample Rate Optimization (SRO) method**: definition of a method for optimizing the sample rate in voltammetry towards reducing power consumption.

3. **Total Charge Detection in Cyclic Voltammetry (TCDC) method**: the invention of a technique to avoid oversampling in voltammetry detection of the analyte.

4. **Propofol Fouling Machine-learning (PFM) method**: development of the first ML-based algorithm for the compensation of non-linearities in an electrochemical sensor.

5. **Quasi Digital (QD) potentiostat**: design and implementation of an event-based, low power, and low noise novel electronic topology for amperometric integrated potentiostat.

6. **Embedded device**: fully integrated, battery-operated, Bluetooth®, an embedded device for continuous and autonomous measurement of anaesthetics.

Chapter 2

Electrochemical Sensors

The smart electronic pen for continuous monitoring of anaesthetics is based on an electrochemical sensor as the main sensor. As previously detailed, an electrochemical sensor is a physicochemical transducer capable of transforming the input information (concentration of analyte under measure) into an electrical signal. In general, the characterisation of a sensor is the collection and verification of all the sensor characteristics, which are mainly sensibility, linearity, working range, precision, accuracy, resolution, repeatability, reproducibility, hysteresis, and saturation [106]. The sensor characterisation is necessary to ensure a guaranteed level of readout accuracy over various operating conditions. Generally, this procedure may require considering a transducer and the whole sensing equipment and the detection methods. In some specific cases, it is possible to take for granted the ability and the performance of the sensing equipment. To use an analogy, in Resistance Temperature Detector (RTD), the characterisation of the performance of the sensor is made with a commercial impedance meter considering only the variation of resistance according to temperature. This will provide designers with sufficient information to develop their sensing equipment upon that given sensor. This is valid also for electrochemical sensors since numerous formal method already exists. In this section, the electrochemical sensor is characterised formally with a commercial instrument called potentiostat using voltammetry analytical methods [64]. Namely, no measurement methods and electronic circuits had been introduced or taken into consideration, but only the physicochemical transducer and its electrochemical behaviour.

Chapter 2 describes the state-of-the-art (Section 2.1) of such sensors and it figures out limitations and solutions. Commercial electrodes which are commonly adopted in literature are tested (Section 2.2). Later, the non-linearities introduced by passivation and secondary phenomena (called fouling) are considered and analysed. Finally, Section 2.3 presents the first-ever proposed needle-shaped sensor for detection of propofol in human serum, specifically developed for the smart electronic pen for continuous monitoring of anaesthetics.

2.1 State-of-the-Art

Several options have been presented in literature for the detection and quantification of pharmacological compounds in human samples. The most common practice is the modification of commercially available electrochemical cells. Nevertheless, the possibilities are endless. Focusing on the targeted cocktail of drugs, composed of paracetamol (analgesic), midazolam (muscle relaxant), and propofol (anaesthetic), the field may be narrowed.

As an example, Screen Printed Electrode (SPE), modified by casting a metal-organic nanostructure on its surface, has been developed to detect fentanyl, a dangerous analgesic narcotics [107]. The paracetamol, usually administered as a pain lever in the cocktail of anaesthetics, is studied in numerous cases reported in literature. Determination of paracetamol concentration may achieved by several different techniques, as an example, mass spectrometry [108], chromatographic methods [109, 110], near-infrared calibration models [111], and Raman spectroscopy [112]. Moreover, electrochemical study and flow injection analysis of paracetamol in pharmaceutical formulations based on SPE and carbon nanotubes [113], Carbon-coated nickel magnetic nanoparticles modified electrodes as a sensor for determination of acetaminophen [114]. Meanwhile, great results in the detection of paracetamol have been achieved using simple and bare SPE electrodes [115].

The muscle relaxant included in the cocktail of anaesthetics under analysis, the midazolam, may be determined by its voltammetric behaviour on glassy carbon electrode [116]. At the same time, both Pencil Graphite Electrode (PGE) and bare SPE may be used to detect it [3].

Propofol drug is a widely adopted anaesthetic, and it is considered the preferable solution with respect to inhalations drugs in general anaesthesia [28]. Due to its extensive usage, the direct monitoring of propofol will improve success in the anaesthesia procedure, and it is, in fact, the main focus of this thesis. There is a growing interest in using blood spot sampling for Therapeutic Drug Monitoring (TDM), usually obtained from finger pricks, which allows simple and cost-effective logistics [117]. However, it is not suitable for constant and continuous monitoring in the surgery room by definition. The detection and quantification of propofol are exploited using chromatographic methods, for example, liquid chromatography [118] and mass spectrometry [119]. As for most of the drug, those methods grants high precision on propofol quantification as well. Despite the advantages of these techniques, the instrumentation is costly, requiring large quantities of expensive organics, not portable, and requires experienced technicians [120, 121]. Today, the practice of detecting propofol through breath analysis is commonly present in literature as non-invasive methods. As example, the determination of propofol concentration in breath can be done using mass spectrometry [122], gas chromatography [123, 124], ion mobility spectrometry [125], and virtual surface acoustic wave techniques [126]. Unfortunately, there is still no evidence of a strict correlation

between propofol concentrations in blood and breath, a key point for real application. Therefore, detection of anaesthetics directly in serum samples is preferred for TDM [127]. For this reason, previous work in literature focused on detection in serum with either boron-doped diamond tips [3], polymeric membrane-coated carbon SPEs [128], or PGE [129].

2.2 Commercial Sensors

In this thesis, some examples of commercial electrochemical sensors are tested to detect anaesthetics to determine detection limits and possible solutions. Those sensors showed good results in previously presented works. In detail, SPE are suitable for measuring paracetamol [115] and PGE for propofol [129]. In particular, SPEs offers a low-cost, disposable device specially designed to work with microvolumes of samples. SPEs are ideal for quality control or research purposes and also for teaching electrochemistry. For those reasons, SPEs are widely proposed in literature to develop new detection methods upon electrochemical techniques. PGEs are also commonly implemented as electrochemical sensors due to their hybridised carbon, which shows high sensitivity, good adsorption, smaller background current, and conductivity. Moreover, PGEs are easy to be prepared, and the surface may be easily modified [130]. Compared to other electrodes such as glassy carbon electrode, the renewal of surface plays an important role for subsequent analysis because electrochemical reactions of the molecule may cause a change in surface properties of the electrode [131]. The propofol is an electroactive molecule so that it can be oxidised and, in principle, quantified through voltammetry techniques as shown in Section 2.2.2. Unfortunately, the problem of electrode fouling limits still today the development of a system for continuous monitoring of anaesthetics as pointed out by Section 2.2.3.

2.2.1 Detection with Screen Printed Electrodes

In this thesis, the characterisation of drug detection with SPE sensors is done using as a benchmark drug paracetamol (APAP). The compound is electroactive and can be easily detected employing Cyclic Voltammetry (CV) or Differential Pulse Voltammetry (DPV). APAP powder from Sigma Aldrich® (Acetaminophen BioXtra, $\geq 99\,\%$) is dissolved on the day of use in a background electrolyte, namely, Phosphate Buffer Saline (PBS) solution at pH 7.4. The buffer is purchased from Sigma Aldrich® as well, and it is composed of 10 mM phosphate buffer, 2.7 mM potassium chloride, and 137 mM sodium chloride. The sensing equipment is provided by a commercial potentiostat, namely the Metrohm Autolab PGSTAT 302N, driven by the software Nova 1.11. The instrument is interfaced to DropSens DRP-110 SPE composed of carbon Working Electrode (WE) with 4 mm diameter, carbon

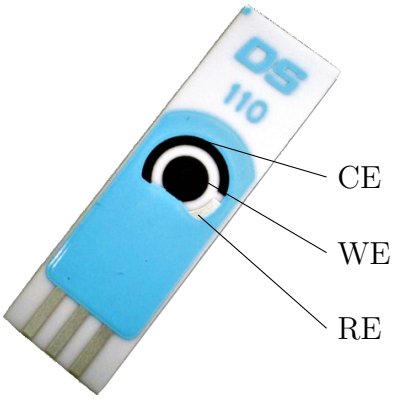

Figure 2.1: DropSens DRP-110, Screen-Printed Electrode (SPE) composed of carbon WE with 4 mm diameter, carbon CE, and silver (pseudo-)RE [132].

Counter Electrode (CE), and silver pseudo-Reference Electrode (RE) [132] for the drug-detection (see Figure 2.1). A full seven-point calibration procedure in the therapeutic range between 50 µM and 300 µM is performed. Subsequent increasing concentration steps of 50 µM of APAP are measured. To consider the inter-electrode variability and to avoid artefacts, the measurement is repeated three times with a new electrode for each condition. The collected data are processed in Matlab® (v. R2017b). After subtracting the background-current obtained by the blank measurement, the peaks are detected and analysed with the *findpeaks* built-in function to return the height of the oxidation-current peak and its position. The calibration curve, the sensitivity and the coefficient of determination (r^2) are derived by *regression* built-in function. All these parameters are detailed in Section 1.3.3.

The CV is performed with a Scan Rate (SR) of 0.1 V / s, in the range between −0.1 V and 1.1 V, starting from 0 V, with a voltage step of 6 mV, and a time step of 60 ms. The total number of sampled points is 406. The voltammogram resulting from a CV seven-point calibration procedure on APAP in its therapeutic range is presented in Figure 2.2a. The Faradaic oxidation peak appears around 500 mV, while the reduction peak is visible below 100 mV. The oxidation peak increases linearly with respect to the concentration of the analyte, as suggested by the Randles-Ševčík equation [133], as shown by the extracted calibration curve (Figure 2.2b). The variation of the current peak varying the SR is considered at fixed 300 µM of APAP, and keeping fixed all the other parameters. the current increases as shown in Figure 2.3a varying the SR from 10 mV / s up to 1 V / s. Figure 2.3b shows that the current peak increase quadratically with respect to the SR, which means the electrochemical reactions is completely reversible [133].

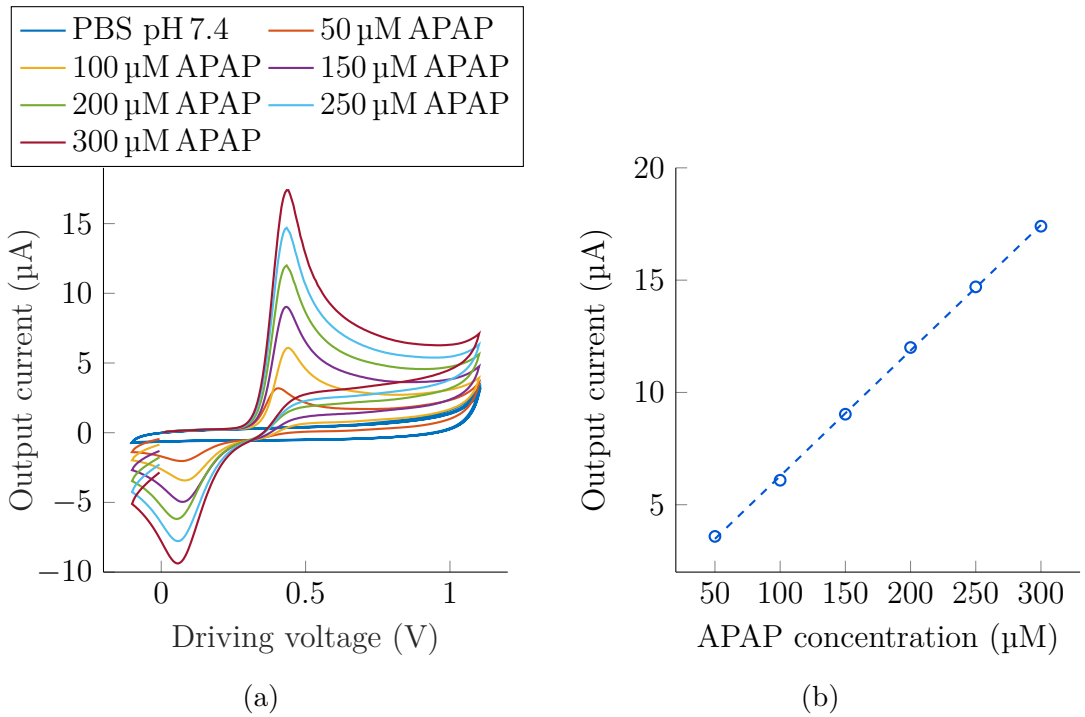

Figure 2.2: CV response of APAP with SPE in the therapeutic range 50 : 300 µM at a SR of 0.1 V s. Full CV (a), and extracted calibration curve from peak eight (b).

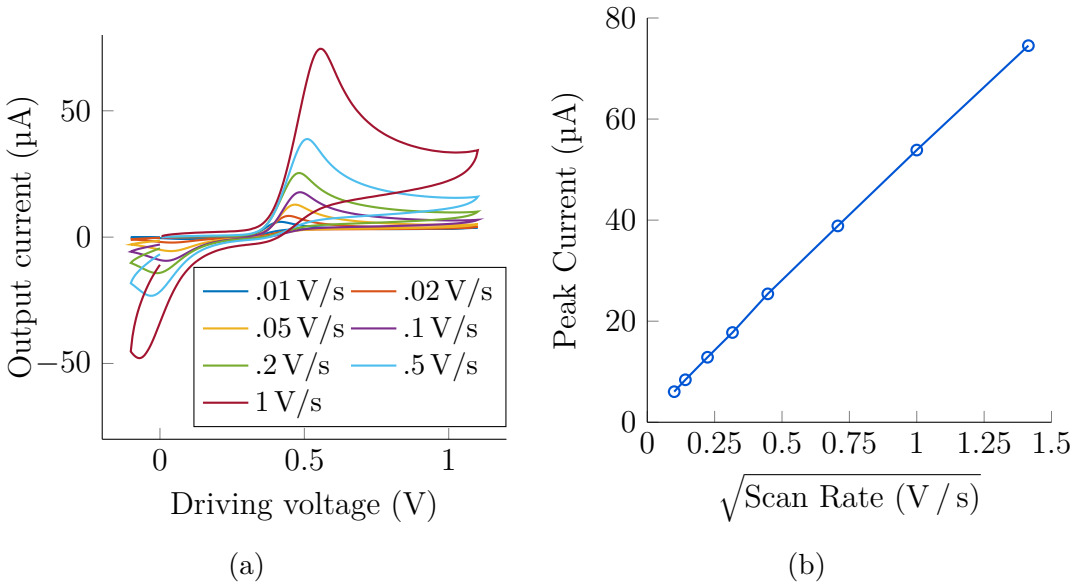

Figure 2.3: SR variation in detection of APAP with SPE in CV, full voltammogram varying SR at fixed 300 µM of APAP (a), and ratio between square root of SR and current peak (b).

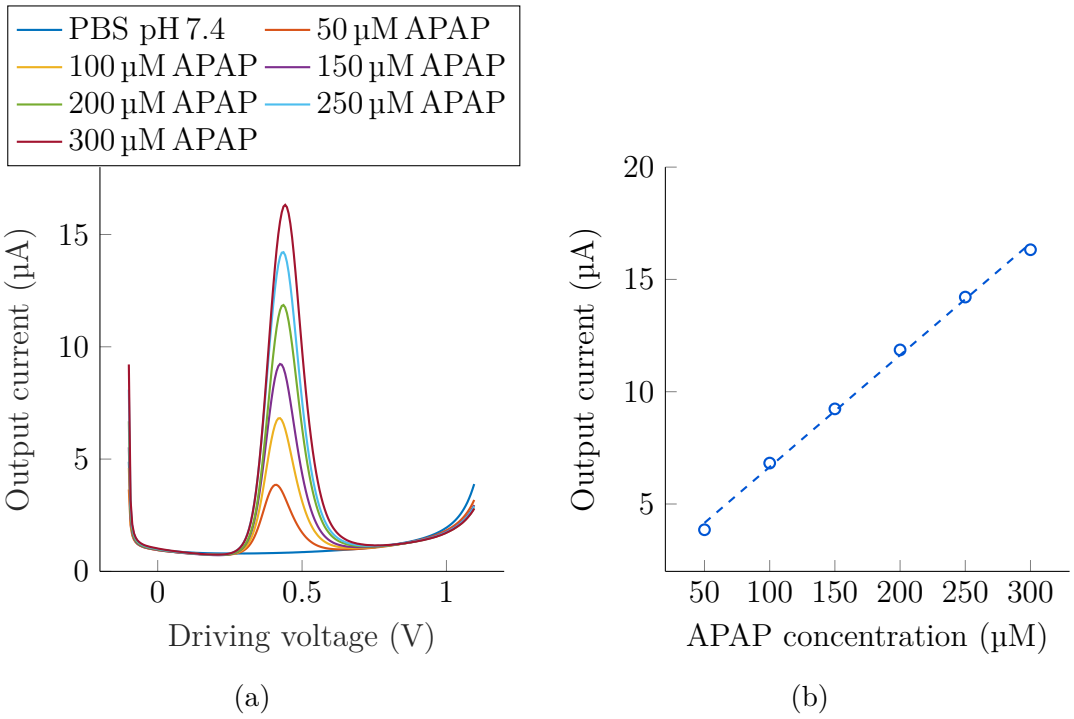

(a) (b)

Figure 2.4: DPV response of APAP with SPE in the therapeutic range 50 : 300 µM at a SR of 0.1 V s. Full CV (a), and extracted calibration curve from peak eight (b).

The DPV is performed with an SR of 0.1 V / s, in the range between −0.1 V and 1.1 V, starting from −0.1 V, with a voltage step of 6 mV, and a time step of 60 ms. The pulse amplitude is 60 mV and the pulse length is 20 ms, with a duty cycle of 33 %. The total number of sampled points is 210.

Figure 2.4a presents the voltammogram obtained by the seven-point calibration procedure. The oxidation peak is visible in the centre of the graph and increases linearly with the increase of APAP concentration, as shown by the extracted calibration curve (Figure 2.4b). DPV method presents a higher sensitivity than CV [133]. The variation of the current peak varying the pulse amplitude and the pulse width are considered at fixed 300 µM of APAP, and fixed all the other parameters. Figure 2.5 presents the variation of DPV response changing the pulse amplitude between 6 mV and 120 mV. The voltammogram presented in Figure 2.5a demonstrates that the increase of the pulse potential enhances the oxidation peak, while the background current increases too. Figure 2.5b shows that the peak current increases linearly with the square root of the pulse amplitude. The effect of varying the duty cycle of the DPV stimuli wave (i.e. the pulse width) between 20 % and 70 % is presented in Figure 2.6. Figure 2.6a highlights that the DPV shapes does not change varying the pulse width, and Figure 2.6b shows how the

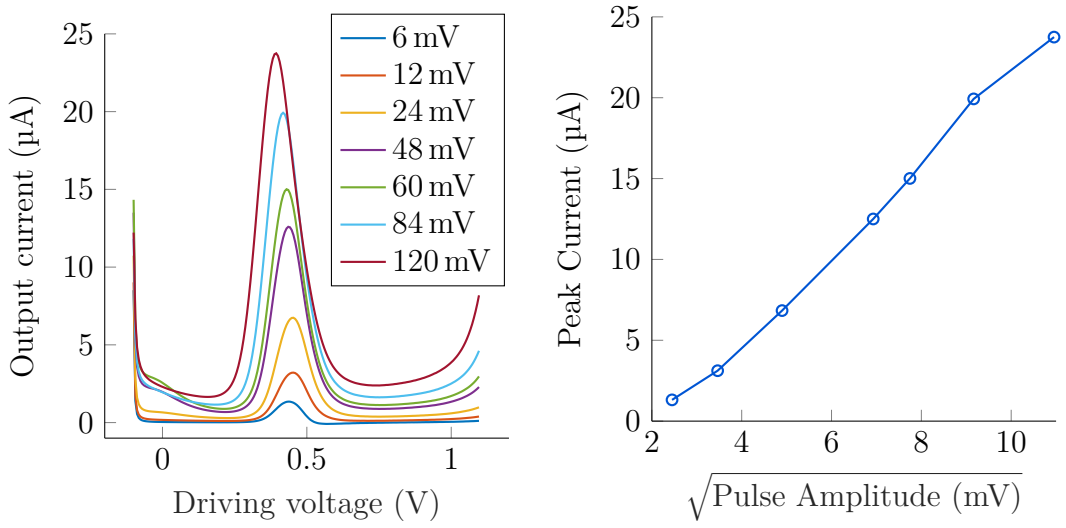

(a) (b)

Figure 2.5: Pulse amplitude variation in detection of APAP with SPE in DVP, full voltammogram varying pulse amplitude at fixed 300 µM of APAP (a), and ratio between the square root of pulse amplitude and current peak (b).

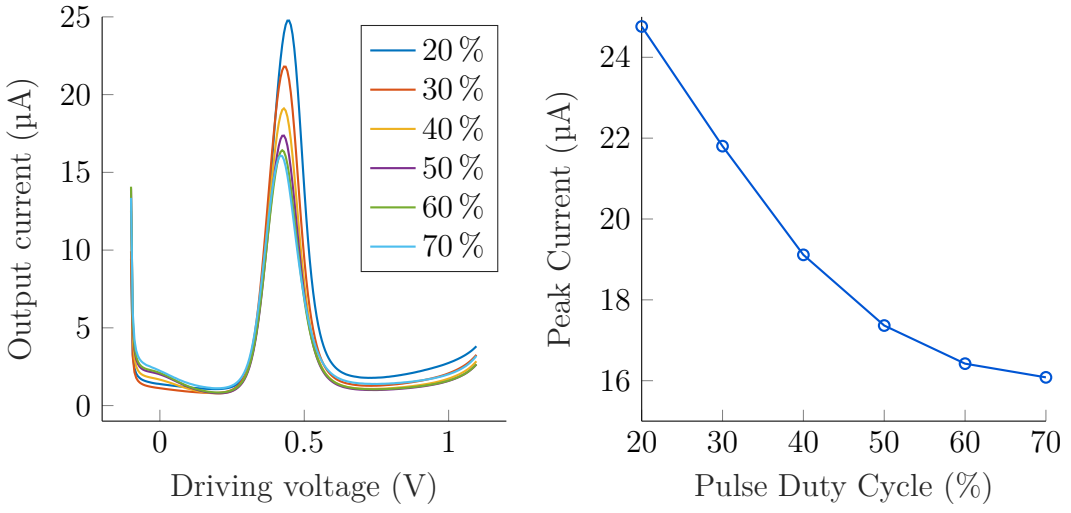

(a) (b)

Figure 2.6: Pulse width (duty cycle) variation in detection of APAP with SPE in DVP, full voltammogram varying pulse amplitude at fixed 300 µM of APAP (a), and ratio between pulse amplitude and current peak (b).

peak decrease decrementing the pulse duty cycle.

2.2.2 Detection with Pencil Graphite Electrodes

Taking advantage of the results of [129], in this thesis, PGE is used to detect the propofol anaesthetic. In particular, a stock solution of 5.4 mM propofol is prepared on the day of use with 2,6-Diisopropylphenol (propofol) purchased from Tokyo Chemical Industry Co., Ltd. and dissolved in 0.1 M NaOH. The samples are prepared with seven concentrations of propofol, equally spaced in its therapeutic range: 1, 12.8, 24.6, 36.4, 48.2, and 60 µM. The samples are prepared in PBS, 10 mM, pH 7.4 from Sigma Aldrich®. The electrochemical cell is composed by a PGE WE, while for CE a platinum wire of 0.3 mm diameter is used, and the RE is a K0265 Ag/AgCl electrode from Ametek Scientific Instruments as shown in Figure 2.7a. Two different PGE are selected, namely the tip of a 2H pencil (Figure 2.7b) and a 3H mechanical pencil lead (Figure 2.7c). The 2H pencil is a commercially-available Staedtler® Noris 120, 2 mm diameter, exposed by 1 mm to the sample, with an active area of around 9.4 mm^2. The 3H mechanical pencil lead is a Staedtler® lead for mechanical pencil Mars Micro 3H, 0.5 mm of diameter, exposed by 3 mm to the sample, with an active area around 4.9 mm^2.

Figure 2.8 shows the resulting voltammogram of propofol detection in the given sample, according to the seven-point calibration, considering as WE the 2H pencil (Figure 2.8a) and the 3H mechanical pencil lead (Figure 2.8b). Both present clear and clean oxidation peaks. Worth to be noted that 2H pencil also presents a secondary peak. Figure 2.9 shows the extracted calibration curves. 2H pencil and

(a) (b) (c)

Figure 2.7: Setup for detection of propofol with PGE, full setup (a) with PGE WE, platinum wire CE and Ag/AgCl RE. The two PGE under analysis are the commonly available 2H pencil (b) and a 3H mechanical pencil lead (c).

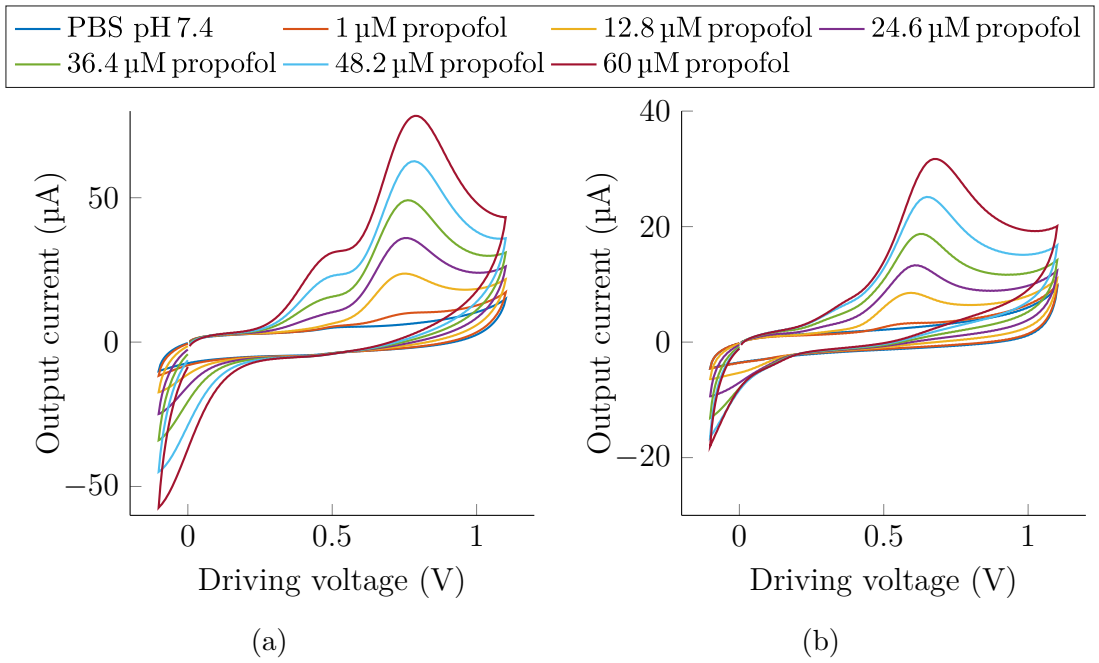

Figure 2.8: CV of detection of propofol with PGE. Considering a 2H pencil (a), and 3H mechanical pencil lead (b).

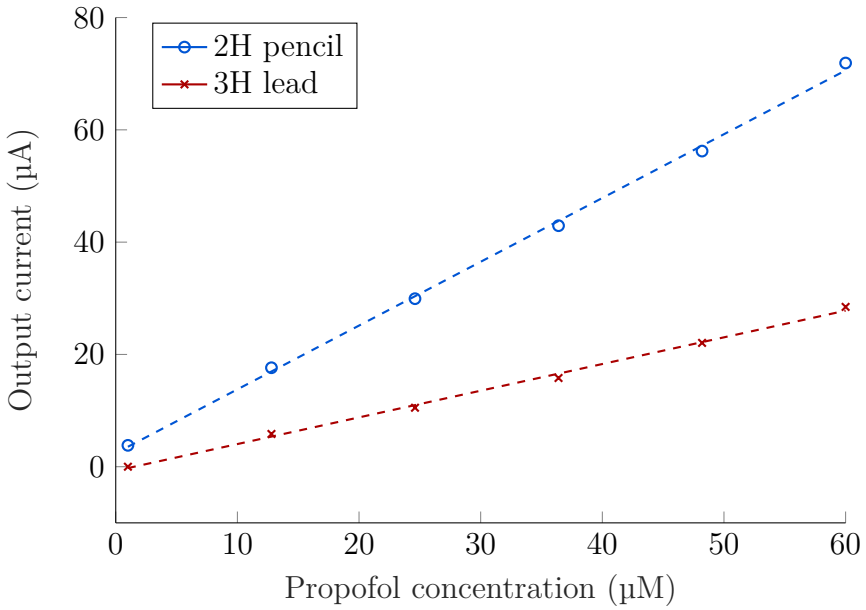

Figure 2.9: Calibration of detection of propofol with PGE. Considering a 2H pencil tip and 3H mechanical pencil lead.

3H mechanical pencil lead exhibit a sensitivity of 1.13 µA / µM and 0.4753 µA / µM, respectively, coherently with the expected different consequent areas of the WEs. The Limit of Detection (LOD, the minimum concentration detectable by the sensor) is 2.43 µM and 3.86 µM. The linearity (as the coefficient of determination r^2) is 99.94 % and 99.86 %. The PGE presents such a good capability to detect propofol with highly linear behaviour, high sensitivity, and low LOD.

2.2.3 The Propofol Fouling

When a voltage between RE and WE is applied to allow the direct oxidation of the propofol monomer, the reaction takes place, and a propofol free radical is generated [134]. The latter can react with O_2 or undergo free-radical polymerisation adding up to a propofol monomer or pre-existing polymer, thus leading to the formation of a polymeric film [135, 136]. This polymeric thin film covers the electrodes and therefore degrades the sensor signal. This behaviour is called fouling, and it is characterised in other phenolic compounds too [137]. Generally, the term electrode-fouling describes the passivation of the surface by a fouling agent, which forms a permanent layer on the interface between electrode and solution. In phenol, the film is tough, thermally stable, and chemically inert itself with low permeability. Being composed of high molecular weight species, it adheres tightly to the electrode. The resulting fouling layer is not uniform and consists of successive blocking films made by compounds with lower molecular weights in the upper region, furthest from the electrode. The subsequent hypothesis by Yang et al. was that charge transfer does not consist in tunnelling through the whole fouling film (10 : 100 nm thick) but only through the lower region, populated by high molar weight compounds [137]. This could be extended to propofol, and it suggests that propofol oxidation may become a charge-transfer limited phenomenon in the presence of a reasonably thick fouling layer.

Several methods had been proposed to minimise the effect of fouling in electrochemistry. First of all, the selection of electrode material is crucial in limiting the fouling. Modified electrodes, using for example metallic nanoparticles [138], graphene [139], nanodiamonds [140], or carbon nanotubes [141], shows better antifouling properties since generally standard carbon and metallic electrodes are affected by fouling. Coating the surface of the electrode could reduce the passivation of the interface, and polymers like Nafion are adopted to this application [142]. Special electrochemical analysis techniques such as DPV and Multiple Pulsed Amperometry (MPA) also mitigates the fouling [143]. The addition of surfactans [144] increases the solubility of reaction products lowering surface passivation.

Considering the continuous monitoring of propofol, which is the target application of the sensor, the literature presents a few attempts at solving the fouling problem. To the best of our knowledge, good results are achieved by coating the electrode [145], with cleaning procedures [136], and with optimised PGE [129]. [145]

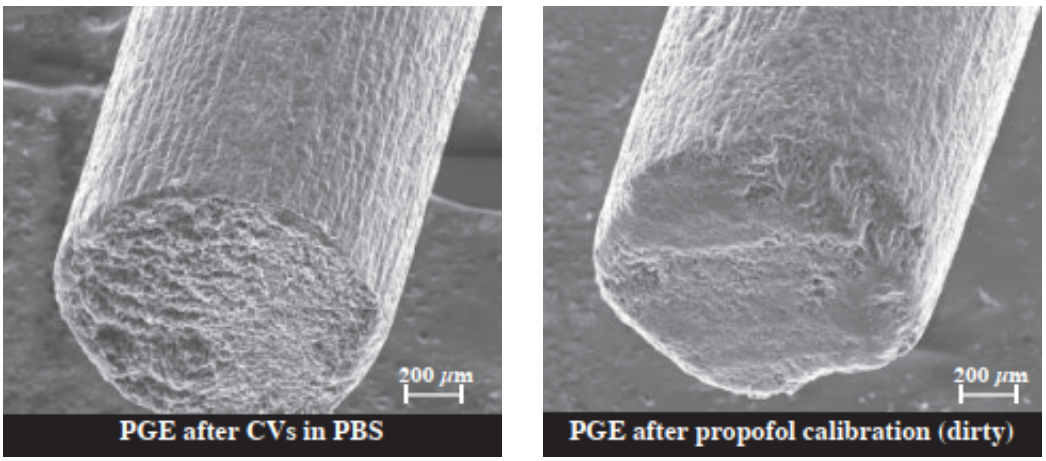

(a) (b)

Figure 2.10: SEM images of PGE, bare electrode after five cycles of CV in clean PBS sample (a), and after one propofol calibration (b). Reprinted with permission from [3].

covered the surface of the electrode with polyvinyl chloride (PVC) membrane. However, its low mechanical resistance brings Stradolini et al. to propose a cleaning solution to ensure the long-term performances [136]. The introduction of PBS or NaOH cleaning steps limits the final application since human intervention is still frequently required to extract the electrode from the sample and keep it in the cleaning solution. To achieve better fouling-resistance, [129] evaluated PGE electrodes. The results demonstrated that commercial pencils are suitable for propofol detection. Their composition can balance the fouling effect; namely, the graphite content of the pencil helps sensitivity and the clay content the fouling resistance. A trade-off can be done balancing the pencil composition, but this result is highly specific to the exact conformation of the sensor. Any small changes in geometry, size, and composition result in a drastic unbalance of performance. Figure 2.10 shows through a Scanning Electron Microscope (SEM) the effect of the propofol fouling on PGE electrodes. Namely, Figure 2.10b shows how the propofol reduction is smothering out, and it passivates the surface of the PGE tip, with respect to a clean one (Figure 2.10a).

The lead for mechanical pencil 3H is tested on fouling since [129] proposed the 3H PGE composition as the best candidate for the detection of propofol. Figure 2.11 presents the phenomena on fouling on the 3H mechanical pencil lead. The graphs present the blank signal, with a new electrode (1^{st} measure), with an electrode after a first run of calibration (2^{nd} measure) and after a second one (3^{rd} measure). Figure 2.11a shows the fouling in the absence of any cleaning process. The propofol sticks to the surface as expected by the theory. This can be seen because the

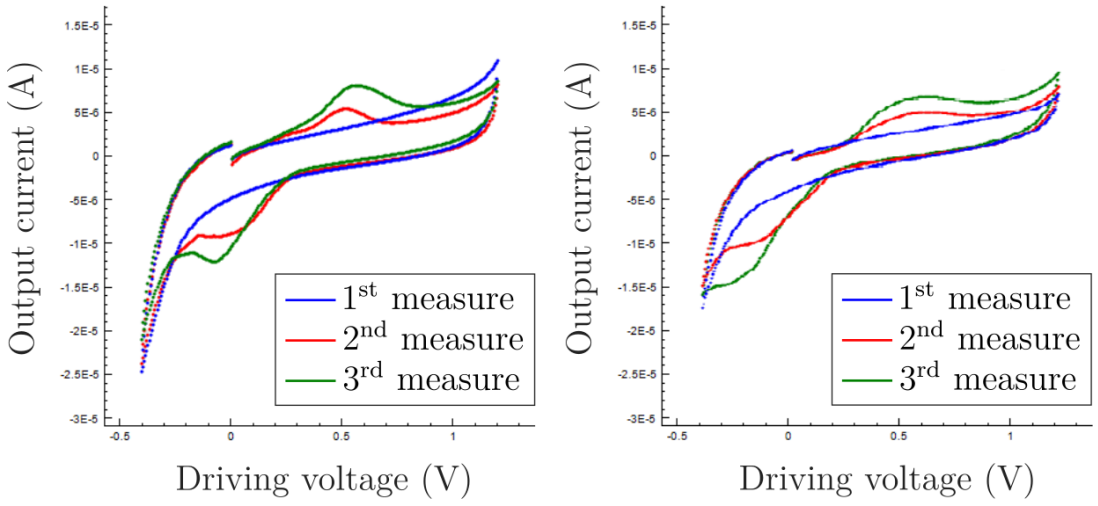

Figure 2.11: Propofol fouling effect on pencil lead 3H electrodes, blank signal after 3 measurement, withouth cleaning step (a) and with cleaning step (b). 1st measure. 2nd measure 3rd measure

propofol is still detected in the blank sample after each new measurement. The cleaning suggested by [136] does not help sufficiently in improving the situation when using the 3H mechanical pencil lead (Figure 2.11b). In this case, a completely new approach based on machine learning algorithms is the solution proposed in Section 3.4.

2.3 Needle-shaped Electrochemical Sensor

In literature, numerous sensors have been proposed for detecting and measuring propofol, achieving LOD of 0.5 µM (0.1 µg / ml) in only 25 s [146], Unfortunately, most sensors that achieve good detection performance are based on blood-spot sampling with disposable sensors. In particular, they employ single-use sensors [62], which cannot be implemented in an automatic TDM closed-loop system. Also, the commercially available sensors discussed and tested in Section 2.2 lack of capability to measure directly in-situ the concentration of anaesthetics. Devices built on top of commercial solutions must leverage on external fluidic chambers [147] or commercial SPE for Dried Blood Spot sampling (DBS) [102], which both hardly cope with the usage during surgery. This thesis proposes a needle-shaped electrochemical sensor for measuring propofol directly in the patient's vein to overcome these limitations. PGEs are suitable for drug monitoring [59] and propofol monitoring. PGEs are also the best candidate for compensating the fouling phenomena [129] with the help of machine learning techniques, as previously mentioned, and fully detailed

in Section 3.4. A novel low-cost and disposable electrode is developed with PGE mechanical pencil lead electrodes of sub-millimetre size in a needle shape. This section presents and details the full process of assembly of the proposed needle-shaped sensor. Finally, the proposed electrode is tested in undiluted human serum at 37 °C to show its performances in the human body. The performance assessment is done in the therapeutic range of propofol, between 30 µM and 240 µM, considering propofol therapeutic concentration can reach up to 40 mg / l (224 µM) [148]. This section is adapted with permission from [98] © 2020 IEEE.

2.3.1 Design and Assembling

The proposed sensor is a three-electrode electrochemical cell in a needle shape to target drug monitoring in-vein directly. Figure 2.12 shows the complete sensor, with the electrochemical cell on the bottom, the case in the middle, the audio jack connector for disposable use on top. As detailed in Figure 2.13, the sensor is composed of two PGE, which are 0.5 mm diameter HB mechanical pencil lead

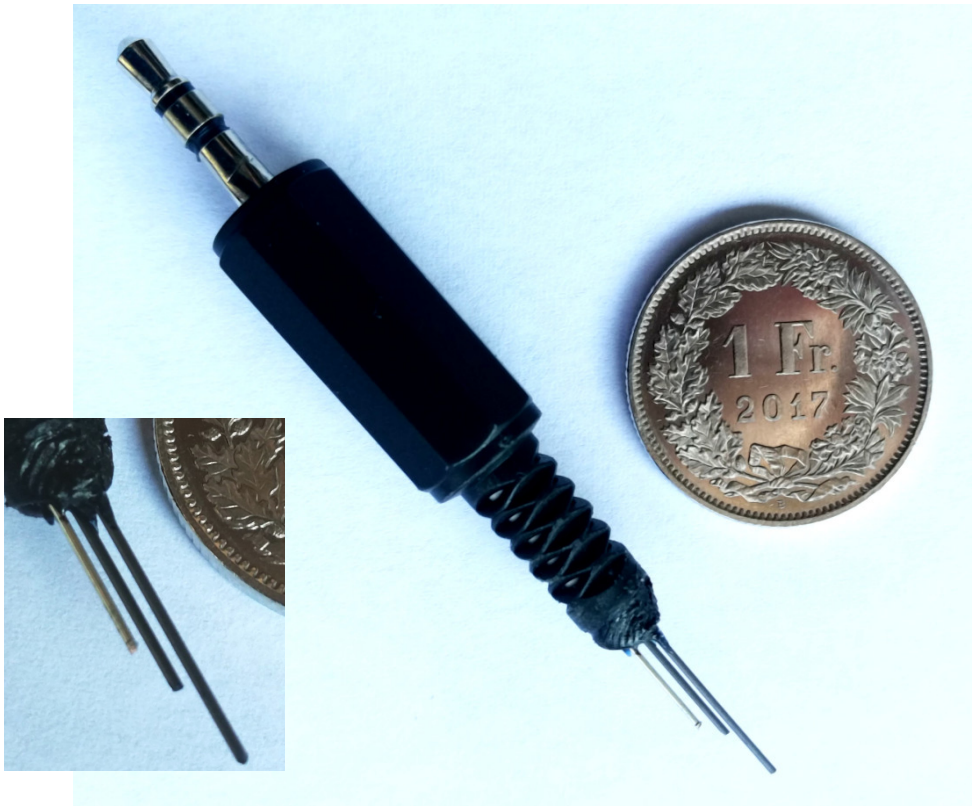

Figure 2.12: The novel disposable and low-cost needle-shaped electrochemical sensor. Reprinted with permission from [98]. © 2020 IEEE.

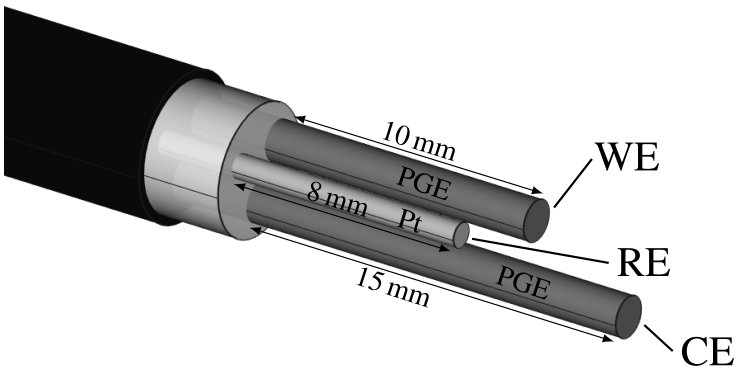

Figure 2.13: Needle-shaped sensor illustration, two PGE electrodes are WE (shorter) and CE (longer), while Pt wire is RE, joint together in a needle-shape. Reprinted with permission from [98]. © 2020 IEEE.

from Papeteria Migros, and one 0.3 mm diameter platinum wire. This composition (HB) has been chosen since it is the most commonly available. Similar to what presented in [136], the WE is the first lead, with a length of 10 mm and an active area of 15.9 mm^2. The second lead is the CE, with a length of 15 mm to maintain a ratio between the area of WE and CE smaller than one. The RE is the Pt wire, with a length of 8 mm. The different length of wires ensures the correct active area ratio among the different electrodes, which is required for best design practice in electrochemical sensors [87].

Figure 2.14 displays the whole assembly process of the proposed sensor. In step (a), the two mechanical pencil leads and the platinum wire are interfaced to a solid 22 AWG black soldering wire, and the connections are stabilised through polyolefin 2 mm diameter red heat-shrink tubes. In step (b), the three electrodes are joined together with a polyolefin 6 mm diameter white heat-shrink tube. In step (c), the three cable-ends are soldered to the three pins of a male audio jack 3.5 mm stereo connector. The sensor is completed in step (d) after closing the cover of the audio jack connector and cutting the three electrodes to length. The electrode tip is cleaned with ethanol first, distilled water second. The sensor is then immersed in PBS, pH 7.4, and ten CV cycles at SR of 0.5 V / s in the voltage window between − 0.6 V and 0.7 V are performed to ensure uniformity on the electrode surface and check connection faults. The sensor is then cleaned with distilled water, let dry, and stored in a dry cabinet.

The design of the presented sensor is the result of a study performed through potassium ferrocyanide to define the best geometry for a disposable and miniaturised sensor. It is worth noticing that the platinum pseudo reference electrode proposed in this thesis did not show any visible difference of stability when compared against silver pseudo reference electrodes present on commercial SPE. The audio jack connector provides a low-cost, disposable, and robust electrical interface

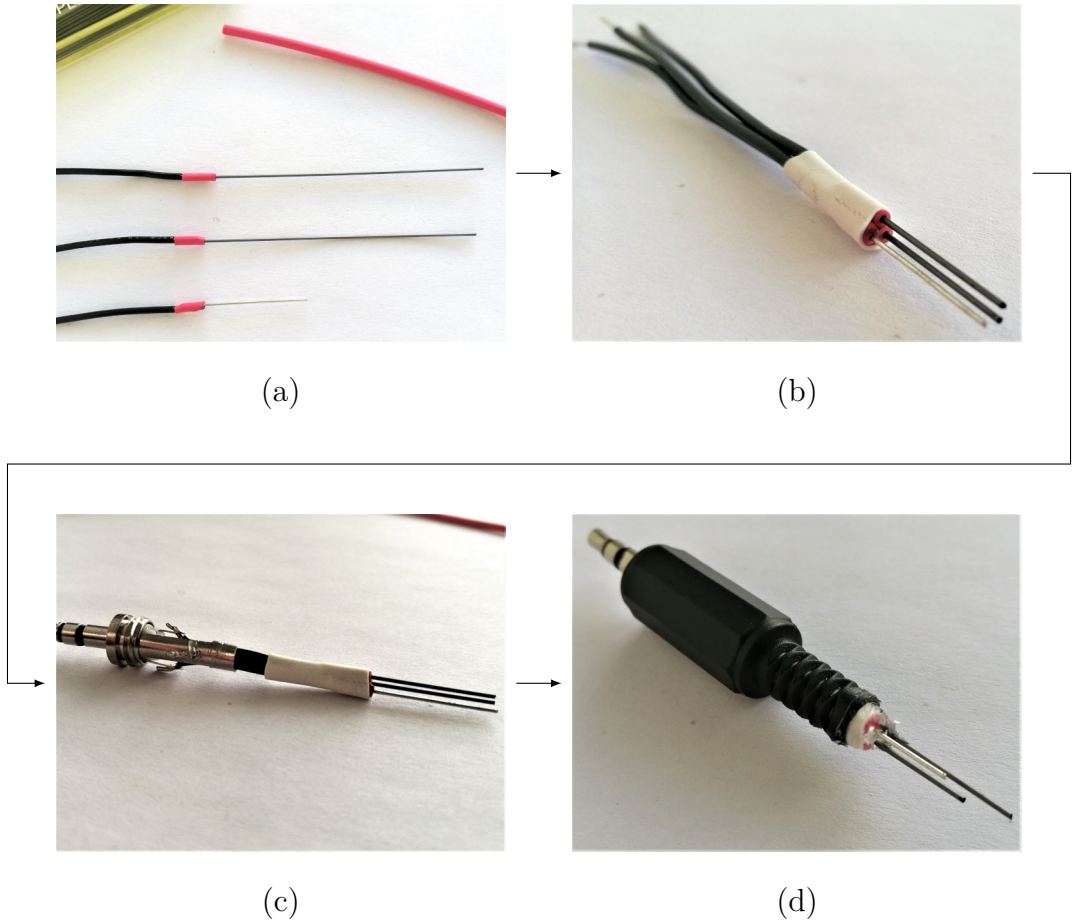

Figure 2.14: Needle-shaped sensor assembly process: mechanical pencil leads and Pt wire connected to soldering wire through heat-shrink tubes (a), joint together (b), soldered to audio jack connector (c), closed and cut to length to form the complete sensor with integrated audio jack connector for point-of-care applications (d). Reprinted with permission from [98]. © 2020 IEEE.

to systems and electronics, being audio jack a robust and widely adopted standard.

2.3.2 Validation and Performance

The solution of 5.4 mM propofol is dissolved in undiluted human serum, heat-inactivated from human male AB plasma, from Sigma-Aldrich as background. The samples are prepared with subsequent dilutions of propofol stock solution in human serum in a 10 ml beaker to obtain eight different concentrations, equally spaced in the range of interest: 30 µM, 60 µM, 90 µM, 120 µM, 150 µM, 180 µM, 210 µM, and 240 µM. The samples are continuously kept at 37 °C and continuously stirred by a hot plate stirrer from VWR®. The needle-shaped sensor is immersed in

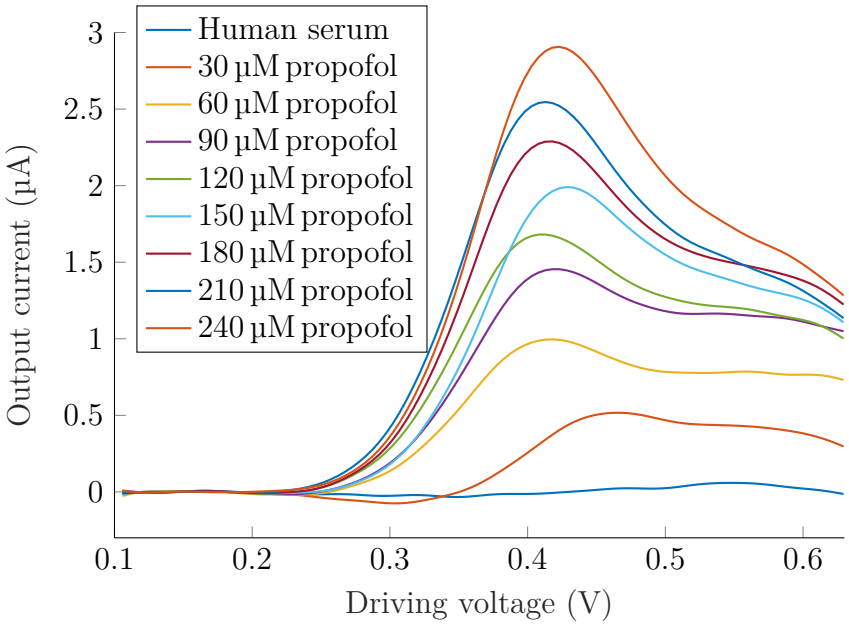

Figure 2.15: Voltammograms acquired by analysis of propofol sample in human serum showing oxidation peaks after signal filtering and baseline subtraction, considering one sensor. Reprinted with permission from [98]. © 2020 IEEE.

the sample solution, and it is connected to a commercial potentiostat (Metrohm Autolab PGSTAT 302N), driven by the software Nova 1.11. The CV is performed at SR of 0.1 V / s, in the voltage windows between – 0.6 V and 0.7 V, with a step voltage of 5 mV, and a step time of 30 ms. All the measurements are repeated three times with three different assembled sensors to validate repeatability and reproducibility. The data are elaborated by Matlab® (v. R2020a). The voltammogram curves are filtered with a low-pass filter at the cut-off frequency of 2 Hz to remove electrical noise. The background current obtained by the blank measurement is subtracted to remove chemical noise.

The proposed sensor had been tested for propofol monitoring in undiluted human serum at body temperature (37°C) in the therapeutic range. Figure 2.15 shows the results of the experimental setup. Namely, Figure 2.15 displays the voltammogram curves acquired by the lab instrument connected to the proposed sensor. The Faradaic peaks related to the propofol oxidation are visible between 0.4 V and 0.5 V. The peaks are highlighted, filtering the signal with a low-pass filter at 2 Hz and removing the baseline. Figure 2.16 shows the resulting calibration point with their confidence interval (derived as three times the standard deviation) and the calibration curve of the proposed sensor. The curve is obtained linearly interpolating the values of the oxidation current-peaks. The calibration displays the performance of the proposed sensor considering repeatability and reproducibility

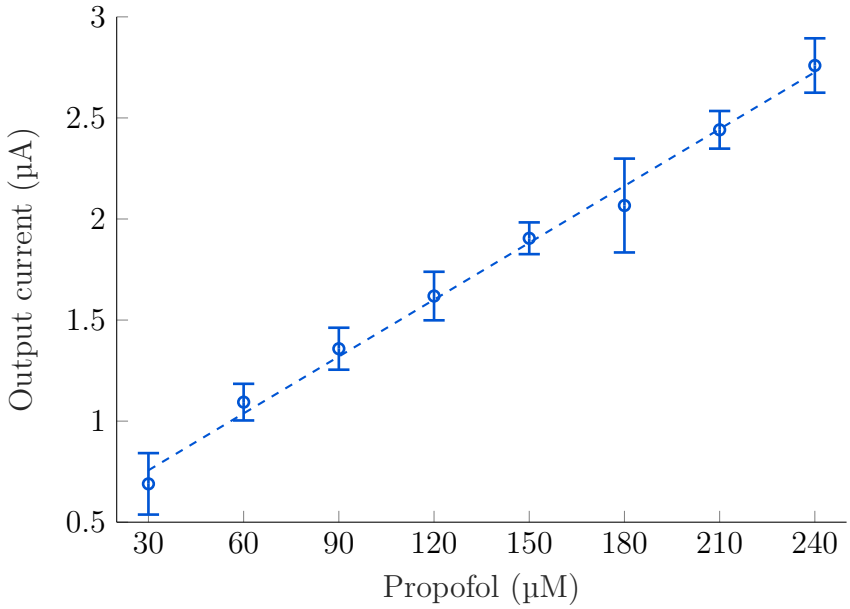

Figure 2.16: Inter-electrodes calibration curve of proposed needle-shaped sensor measuring propofol in human serum. The sensor shows good linearity and low uncertain. Reprinted with permission from [98]. © 2020 IEEE.

Table 2.1: Inter-electrodes performance results of needle-shaped sensor, in terms of sensitivity, LOD, and peak position. Reprinted with permission from [98]. © 2020 IEEE.

Sensitivity	$9.4 \pm 3.9\,\mathrm{nA/\mu M}$
Coefficient of Determination (r^2)	0.99
LOD	$7.2 \pm 3.0\,\mu\mathrm{M}$
Peak position	$462 \pm 37\,\mathrm{mV}$

since an inter-electrode analysis obtains it. As summarised by Table 2.1, the sensor Sensitivity (S, the calibration coefficient) is $9.4 \pm 3.9\,\mathrm{nA/\mu M}$. The coefficient of determination of linear regression (r^2) is higher than 99 %, indicating a good fit of the linear regressor to the calibration. The LOD, which is the minimum concentration of propofol detectable by the sensor, is $7.2 \pm 3.0\,\mu\mathrm{M}$, lower than the minimum concentration of interest for the application. The peak position is stable around $462 \pm 37\,\mathrm{mV}$, over-time and inter-electrodes, proving the performance and stability of the platinum wire pseudo-reference electrode. The repetition assures the reproducibility of the measurement on three different items of the proposed sensor. All these results confirm the effectiveness of the sensor for the target application.

2.4 Summary and Main Original Contributions

In this chapter, the design, development, and validation of a fully custom electrochemical sensor are exposed. Commercially available solutions are analysed, taking advantage of comparing to previous publications. Commercial SPEs are fully characterised in the detection of APAP using both CV and DVP electrochemical analysis techniques. Later, propofol electrochemical behaviour is exploited with PGE, using 2H pencils and 3H 0.5 mm diameter mechanical pencil leads. In Section 2.2.3, it is reported that electrochemical sensor suffers from propofol fouling phenomena, and that, there is not a reasonable solution at the level of electrochemical interfaces despite all the efforts presented in literature. Section 3.4 proposes a solution with a novel technique based on ML approaches. Finally, a new PGE needle-shaped electrochemical sensor for direct monitoring of anesthesiology practices can improve anesthesiology practices. The sensor is disposable and low-cost, composed of the most common mechanical pencil leads (HB composition) and platinum wire, with the help of an audio jack connector. The proposed sensor featured 99 % linearity and a limit of detection of 7.2 ± 3.0 µM in human serum between 30 µM and 240 µM of propofol at 37 °C, proving optimal performance for the target application.

Chapter 3

Measurement Methods

The proposed pen for continuous anaesthetics monitoring features three entirely novel detection methods: the Sampling Rate Optimization (SRO), the Total Charge Detection in Cyclic voltammetry (TCDC), and the Propofol Fouling Machine learning (PFM). In general, the measurement/detection methods are collections of procedures, equations, and routines, formalised to obtain a measure such as an unknown quantity. Despite being the electrochemical cell well established and formalised in literature, it can be used, modified, and optimised in infinite ways. In the specific case of electrochemical sensors, the aim is to translate the unknown concentration of target molecules in an electrical signal, and from this, with a specific method, estimate the concentration numerically. In this, a definition of sampling strategies of the electrical quantity, mathematical/physical relations, and estimation models must be included. Different methods may primarily influence the electronics for the electrochemical sensor in terms of resources.

This thesis also focuses on the relation between sensors and electronics employing detection methods, pointing out the effects on measurement performances. Targeting the final application of the continuous monitoring anaesthetics, which presents novel and significant challenges, three new measurement and detection methods are fully devolved, formalised, implemented, and validated. The methods are designed to target a specific application, but the formalization makes them suitable for a set of possible different applications. For the first time, the SRO method (Section 3.2) defines a simple yet effective way to quantify the optimal sample rate in voltammetry-based sensing techniques. In Section 3.3, the innovative TCDC method proposes a different way of directly determine the concentration of analyte in generic electrochemical voltammograms presenting completely reversible oxidation. Finally, the recent explosion of machine learning technologies inspired the PFM method (Section 3.4), which allows solving the well-known problem of the fouling that usually prevents a correct estimation of the concentration. This thesis demonstrates that Machine Learning (ML) based algorithm can be used in the direct estimation of drug concentration, especially to compensate non-linearities that

are commonly present in the outputs from a lot of different electrochemical sensors.

3.1 State-of-the-Art

Biosensors are playing a relevant role in numerous fields of application, including healthcare, environment, and food industries [149] and may be used for point-of-care diagnostics [150]. The real-time point-of-need biochemical sensing provides the possibility of direct non-invasive monitoring of patients, giving continuously valuable insights into their health and well-being. Electro-analytical measurements can be directly exploited in-situ and without sample purification. This brings the benefit of a point-of-care detection of several different analytes and drugs on wearable, portable, and IoT systems [151].

In doing that, Potentiometric and amperometric techniques, for example, Open-Circuit Potential (OCP) [152] and Chrono-Amperometry (CA) [153], are usually exploited in wearable devices for electrochemical sensing thanks to their capability of carrying out the bio-sensing information through a low-complexity electrical-converter. In those cases, the sampled information (concentration of analyte) is directly related to an electrical quantity, a voltage, or a current. The number of samples is equal to the number of information detected: one single sample of voltage/current directly gives one information on the concentration. In information theory, when the ratio between the number of samples and the number of information detected is one, it is possible to say that the information throughput is equal to one (i.e., one electronic sample to get one detected concentration). Nevertheless, OCP and CA are not suitable for the detection of all the possible analytes due to the higher variability and the poor stability over time of micro reference electrodes [154].

The voltammetry-based electro-analytical tools are primarily used in electrochemistry to obtain quantitative information on RedOx processes in a laboratory environment [155]. The voltammogram has a peculiar shape that depends, for example, on the drug present in the solution with current peaks corresponding to RedOx phenomena. Thanks to the recent advancement in electronics, voltammetry-based techniques appear on the scene as methods for direct sensing at the point-of-need [156, 157, 158]. Voltammetry techniques, like Cyclic Voltammetry (CV) and Differential Pulse Voltammetry (DPV), are amperometric sensing methods widely adopted to determine the concentration of several drugs [159, 160]. CV and DPV are required to compensate for poor stability and high variability over time of reference electrodes and reference potentials. The voltammogram is automatically analysed by software/firmware to evaluate the concentration of the drug [133]. The indirect method of measuring through peak-determination in voltammetry introduces complexity and increases the data bandwidth (w.r.t. OCP and CA). The information throughput, in this case, is no more one: to sense one concentration,

the current must be sampled much more than one time. However, the higher complexity of the method increases specificity and sensitivity [133] and provides simultaneous determination of different compounds [115].

Soft modelling techniques based on machine learning are commonly integrated into bio-sensor schemes as tools for solving complex mathematical models related to the biochemical processes implied at the level of the sensors [161, 162]. Applications such as peak deconvolution, pH, temperature, and fouling compensation are successfully applied to e-tongues and e-noses cyclic voltammograms with the aid of ML techniques such as support vector machines and Artificial Neural Networks (ANNs) [162, 163, 164, 165]. Different feature extraction schemes may be integrated into the ML methods such as principal component analysis and Fourier or Wavelet transforms [166, 167] to comply with the limited computational resources that are associated with the bio-sensor. The fouling phenomenon common for all phenolic compounds is characterised by a solid non-linear response in the cyclic voltammograms, being to date without any well-established mathematical model.

Chemometric techniques based on ML are successfully applied in the past to compensate for the lack of a theoretical model by dynamically compensating the fouling process along with other non-linear phenomena [168, 169, 170, 171, 172, 173, 174]. In general, the non-linearity of phenolic compounds can be approximated by two linear intervals, usually situated on the extremities of the curve, thus the usage of the already proven ML techniques being very suitable. Due to its phenolic group, propofol may benefit from the extensive studies that have already been conducted on serotonin and dopamine, which are two phenolic compounds related to neurological activity. P. Puthongkham et al. conducted an extensive analysis of methods based on ML techniques used to compensate the non-linearity associated with these neurological compounds measurements achieved by cyclic voltammetry [175]. They highlighted that the most widely used ML technique is based on ANNs. In addition to these neurotransmitters, there is an excellent selection of phenolic compounds recently investigated for their non-linear responses. Catechol was successfully detected in water samples with a limit of detection of 32 nM and almost undetectable interferences caused by other water phenolic compounds for up to fifteen independent experiments using a calibration method based on ANNs [172]. Polyphenolic compounds from olive oil samples are quantified in the micromolar range by using an e-tongue system combined with soft independent modelling of class Analogies algorithm that could replicate the results of spectrophotometer technique [170]. However, to the best of my knowledge, there has never been proposed an ML algorithm specifically designed to compensate the fouling of propofol.

3.2 Sample Rate Optimisation

Drugs can be detected either through CV or DPV with simple devices for continuous monitoring. Figure 3.1 details those methods relating to their most relevant parameters. The CV (Figure 3.1a) procedure requires the application of a driving voltage ramp between Working Electrode (WE) and Reference Electrode (RE), that usually is generated through a staircase of voltage step, defined by a voltage height (V_{step}) and a time length (t_{step}). The voltage scan ranges in an interval related to the RedOx process under analysis. The ratio between V_{step} and t_{step} is the SR (Scan Rate). Every sampling time interval t_{sample}, a current sample is acquired from the Counter Electrode (CE). According to the Randles-Ševčík equation [133], is possible to derive the analyte concentration by processing the voltammogram to detect the height of the current peak [155]. As already detailed in Section 2.2, the DPV (Figure 3.1b) adds to the staircase a pulse wave signal and introduces as main advantages the reduction of non-Faradic current related to double layer effect, the enhancement of the current peak, and the reduction of noise [176]. Typically, CV is applied to detect both oxidation and reduction peaks, while DPV only for one kind of reaction; for this reason, the voltage-scan ranges can be different in the two methods. From electrochemical determination, it is possible to derive the calibration curve (Figure 3.1c), which is the relation between the concentration of analyte and the current (in voltammetry, the height of the current-peak). The calibration curve forms a straight line in the region of interest, and the sensitivity represents the slope of this curve.

The voltammetry approach requires the sampling of a well-defined voltammogram to be effective. Despite the massive literature, an actual definition of the optimal sampling rate does not exist to the best of our knowledge. This value is usually set by empirical methods, for example, considering how many data points form the complete voltammogram graph. Considering this new scenario, portable devices strongly constraint the maximum power consumption of the system. The reduction of the sampling rate of the sensing node is one possible approach to enlarge the battery life-time [177], leading to a reduction of data density and signal bandwidth. In fact, the key components of the power consumption in the device are related to the power spent by signal elaboration and data transmission, which are both directly influenced by the sampling rate. Therefore, as already suggested by [178, 179, 180], there is the need for novel and effective methods for reducing and optimising the sampling rate in voltammetry. In doing this, [178, 179, 180] consider the Fast Scan Cyclic Voltammetry (FSCV) for neurotransmitters, a specific case where the sample rate is limited by communication bandwidth. Differently, to the best of our knowledge, CV and DPV methods for drug monitoring have never been investigated with dealing with sampling-rate issues. Hence, Sample Rate Optimisation (SRO) in the voltammetry method is developed in this thesis to define and derive the best sampling rate for CV detection of any drug. This method may

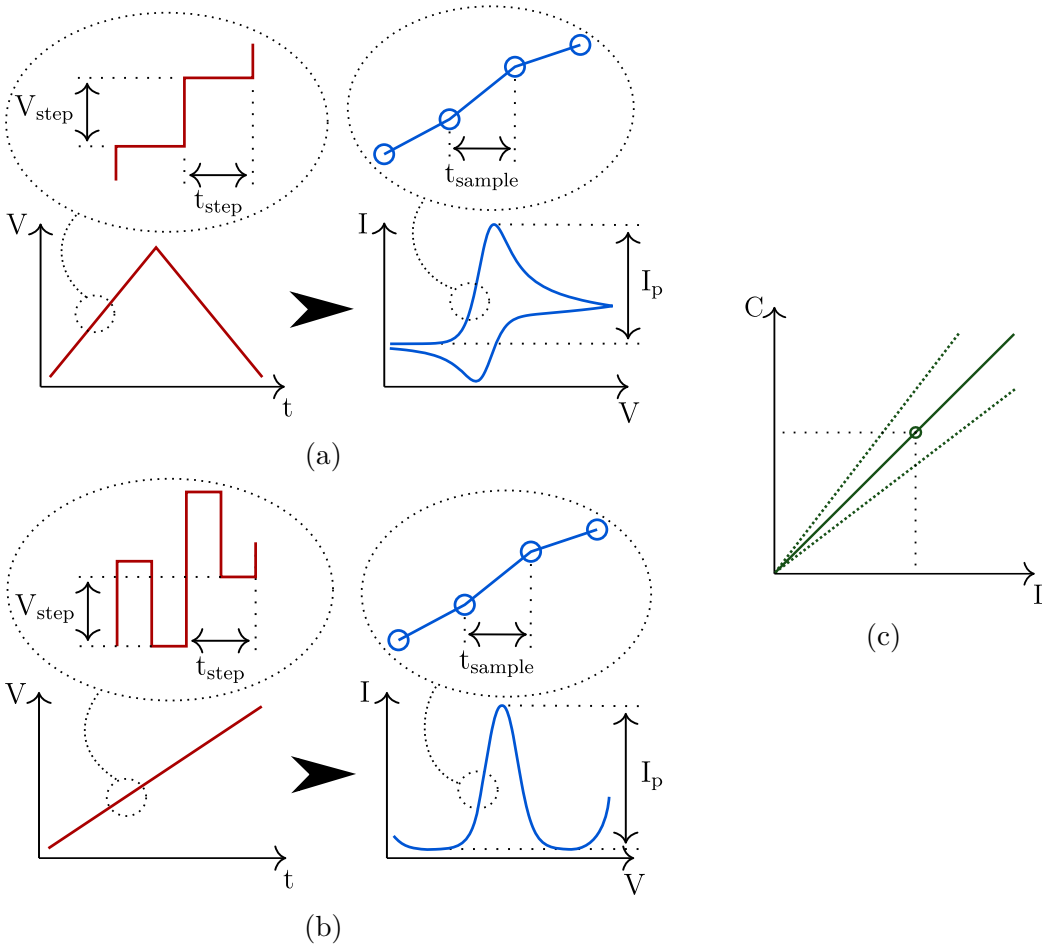

Figure 3.1: Example of voltammetry methods: In CV (a) the electrochemical cell is driven by the a staircase of potential while in DPV (b) by a differential pulse. Sampling the output voltammogram it is possible to extract in both cases a calibration curve, similar to (c). Reprinted with permission from [99]. © 2019 IEEE.

be introduced in every sensor's design path, aiming to use CV or DPV sensing techniques. This section is adapted with permission from [99] © 2019 IEEE.

3.2.1 SRO Method

Considering the main parameters of CV and DPV methods as the Scan Rate (SR), the total number of samples per scan (N_S), and the extension in voltage of scan window (V_{scan}), the sampling frequency (F_S) is defined as:

$$F_S = SR \cdot \frac{N_S}{V_{scan}} \tag{3.1}$$

Equation 3.1 provides three degrees of freedom which can be used to reduce the sampling rate F_S. However, the voltage scan interval is determined by the reaction under analysis, and also, the SR is a variable that should be primarily optimised considering the diffusion of the reaction [87]. For this reason, if the analyte and the electrochemical sensor are fixed, the SR and the voltage window (V_{scan}) are fixed by the specific detection method. Only the remaining free parameter, which is the number of samples N_S, may reduce F_S. Worth noticing that the Nyquist theorem is hardly applicable in the definition of the best sampling frequency. The cyclic voltammogram behaves as a triangular wave, where oxidation species meet reduction species. The triangular wave does not exist in reality since it presents an infinite, completely flat spectrum. Similarly, the voltammogram presents a spectrum that looks like a dinosaur tale, without poles and zeros. It is really hard to define any metrics and any band of interest to apply the Nyquist theorem in this situation. For this reason, the SRO is a procedure to derive the best sampling frequency given an electrochemical sensor experimentally.

The sensing of paracetamol drag (APAP) using Phosphate Buffer Saline (PBS) solution as background electrolyte is considered to define the SRO method. The sensing equipment is composed of a commercial potentiostat (Metrohm Autolab PGSTAT 302N) and interfaced to a standard DropSens DRP-110 Screen Printed Electrode (SPE). Chemicals and details are presented in Section 2.2.1. A parametric analysis is performed in CV considering a different number of samples per voltammogram, equivalently varying the sampling frequency (F_S) to reduce the sample rate in SRO. The SR is set to $0.2\,\mathrm{V/s}$, the driving voltage ranges between $-0.1\,\mathrm{V}$ and $1.1\,\mathrm{V}$, while the step voltage height ranges between $1\,\mathrm{mV}$ and $24\,\mathrm{mV}$, and the step time length ranges in between $5\,\mathrm{ms}$ and $120\,\mathrm{ms}$.

Figure 3.2 graphically presents the results. In Figure 3.2a, the y-axis shows the peak-current error, which is defined as the numerical difference between the best possible estimation of the peak (i.e., sampling the current with the maximum sampling frequency granted by the instrument [181]) and a given approximation of the estimated peak (i.e., sampling the current with a given frequency, x-axis). The error quasi-linearly depends on the sampling period. This effect is due to the lower resolution in the peak measurement, but it is also highly influenced by the increase of voltage step height [182]. Figure 3.2b analyses the Signal to Noise Ratio (SNR, y-axis) versus the sampling frequency. Two different values are taken into account: the SNR of the full voltammogram, and the SNR of the detected output, i.e., the CV peak value. The SNR is defined considering the signal (S) as the full voltammogram or the detected peak at the maximum possible sampling rate. At the same time, the noise (N) is the difference between the signal (S) and the output voltammogram or peak at the given sampling frequency. The noise introduced by the reduction of sampling frequency is visibly lower considering the CV-peak with respect to the noise present in the full voltammogram. This happens because the peak detection is not a linear function but a feature-extractor function, acting to

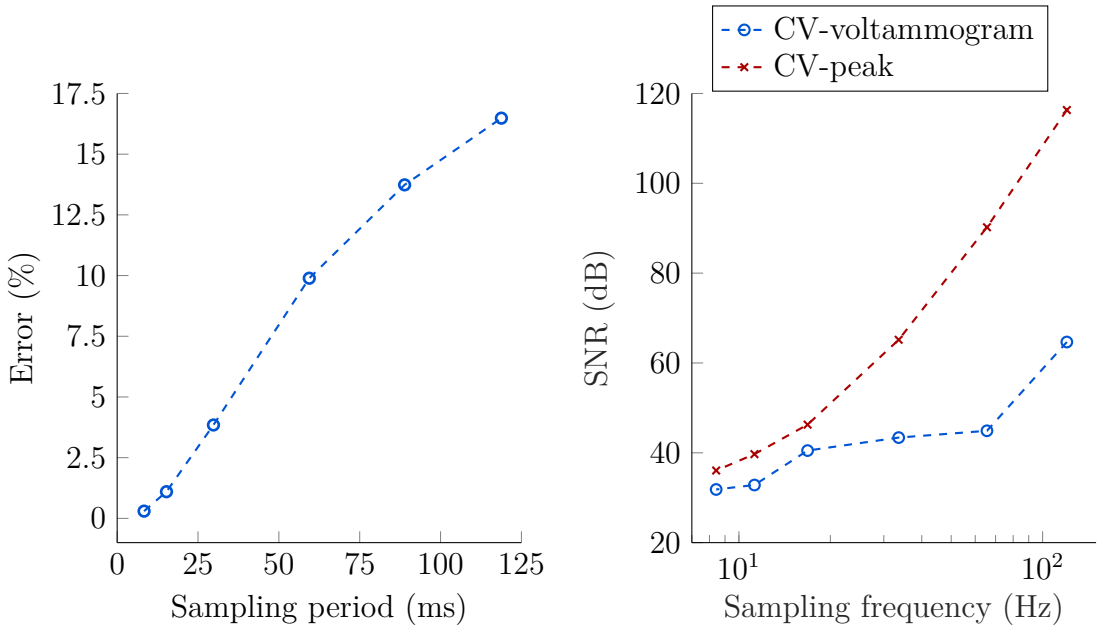

Figure 3.2: Analysis of CV output varying sampling rate: peak error percentage w.r.t the maximum (a), and SNR ratio (b) w.r.t. the maximum of full voltammogram (CV-voltammogram) and detected peaks (CV-peak). Reprinted with permission from [99]. © 2019 IEEE.

some extent as a filter. The output on which to develop the electrochemical sensor is primarily the peak height. The SRO method proves that it is feasible to reduce the sampling rate over what is usually considered the limit. The noise introduced in the voltammogram does not reflect linearly to the increase of noise in the output measure.

3.2.2 Validation and Performance

A complete seven-point calibration procedure on paracetamol, in its therapeutic range (i.e., between 50 µM and 300 µM of APAP) is performed for the validation of the SRO method. In detail, the CV is performed with an SR of 0.2 V / s, with a driving voltage ranging between −0.1 V and 1.1 V, with a step voltage height of 6 mV, and a step time length of 30 ms. The DPV is performed at 0.1 V / s, in the range between 0 V and 1 V, with a step height of 6 mV, an step length of 60 ms, the pulse amplitude is set to 60 mV, and the pulse time length to 30 ms.

The analysis is exploited on the data collected with the seven-points calibration halving the sampling frequency progressively from 33 Hz down to 0.1 Hz. The

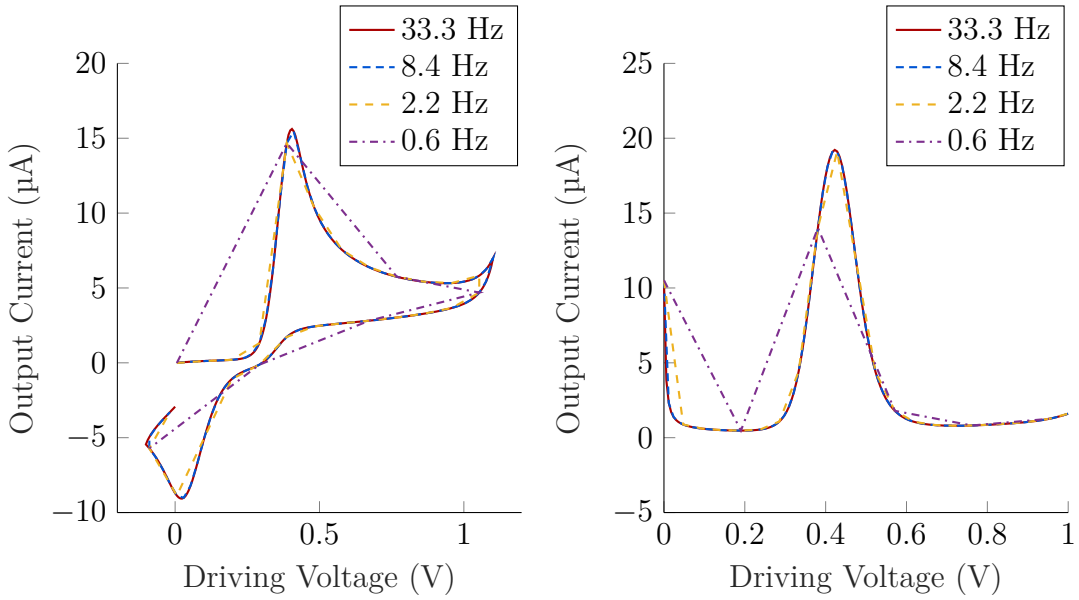

Figure 3.3: Resulting voltammograms in CV (a) and DPV (b), varying the sample-rate. Reprinted with permission from [99]. © 2019 IEEE.

frequency under test span in a range obtained by instrument (Autolab) indications [181]. The output current is re-sampled with an increasingly higher sampling interval (t_{sample} in Figure 3.1a). The shape of the input driving voltage is left unvaried to limit any effect related to the increase of the voltage step (V_{step} in Figure 3.1a). The down-sampling procedure visibly reduces the quantity of information in the voltammogram. Figure 3.3 presents some points of the analysis for demonstration purposes. Figure 3.4 graphically shows the results of this analysis from 33 Hz down to 0.6 Hz. Below this frequency, it is not possible to retrieve any useful information from the voltammogram. The results between 0.1 Hz and 0.6 Hz are not considered. The sensitivity (3.4a), the Limit of Detection (LOD) (3.4b), the current peak position (3.4c), and the linearity of the calibration curves (3.4d) are the parameters under investigation. The measurement errors are evaluated from the experimental data, considering the standard deviation on each computed parameter three times. The measurement error increases visibly with the reduction of the sampling rate in all the cases. The DPV method compensates for the sensing errors by applying a differential detection and consequently enhances the LOD. The peak position remains stable, varying its resolution, proving the selectivity. The linearity shows a drop in the DPV method below 2.2 Hz, defining a clear limit in the proposed experimental setup.

It is possible to obtain and evaluate the best trade-off just considering the data reported in Figure 3.4 to minimise the sampling rate without affecting the detection

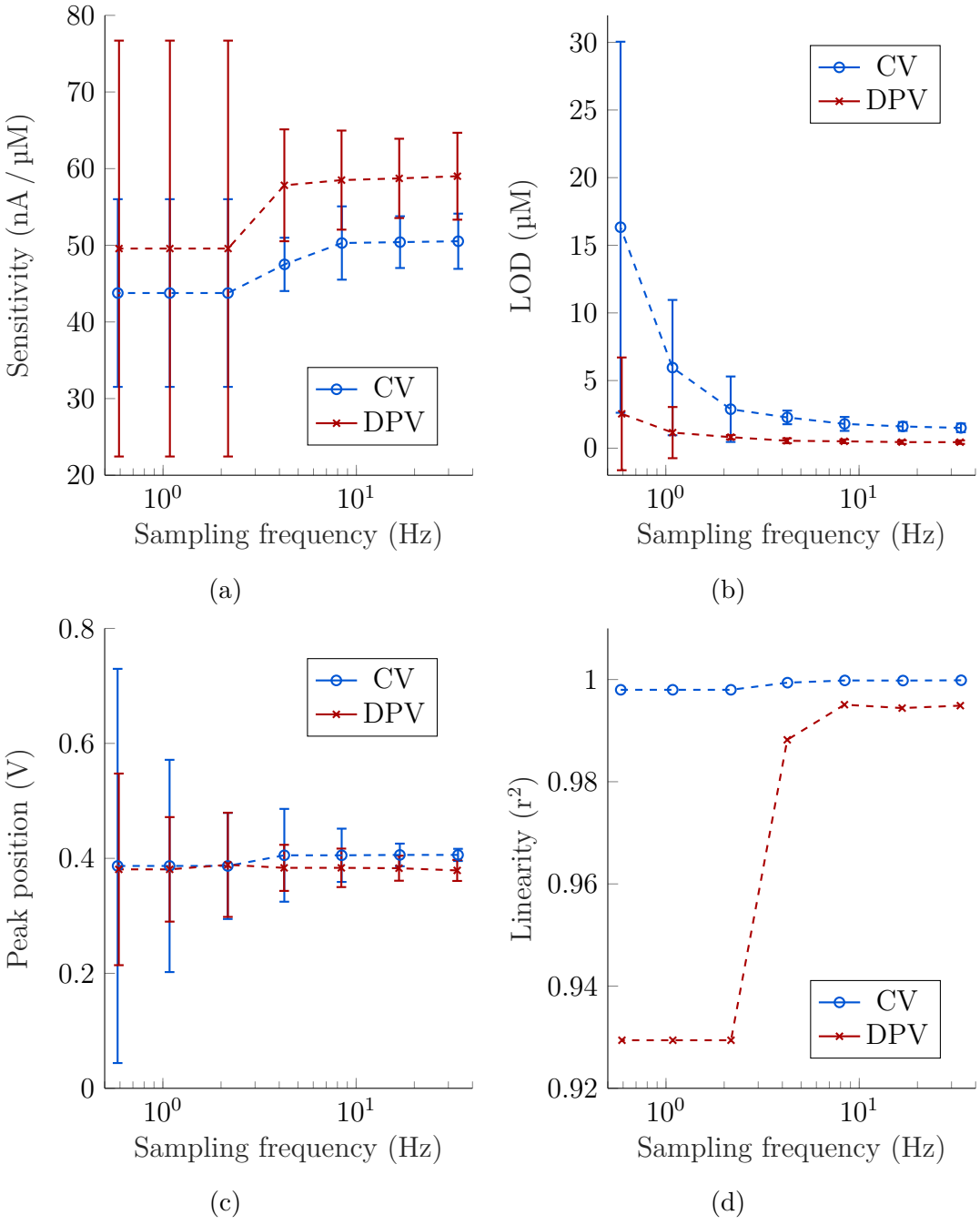

Figure 3.4: Effect of down-sampling w.r.t. sampling frequency in CV and DPV on the sensors metrics: sensitivity (a), LOD (b), voltage peak position (c), and calibration curve linearity (d) . Reprinted with permission from [99]. © 2019 IEEE.

performance. Considering that 50 µM is the minimum therapeutic concentration of paracetamol, it is possible to define that the LOD cannot exceed one-tenth of this

Table 3.1: Comparison between empirical-defined sampling rate approach and the proposed optimal sampling rate approach. Reprinted with permission from [99]. © 2019 IEEE.

	Empirical approach		Proposed approach	
	CV	DPV	CV	DPV
Number of sample	404	338	51	22
Sampling frequency (Hz)	33.3	33.3	4.2	2.2
Sensitivity (nA / µM)	50.5 ± 3.6	59.0 ± 5.7	47.5 ± 3.5	57.8 ± 7.3
LOD (µM)	1.50 ± 0.11	0.45 ± 0.04	2.27 ± 0.16	1.15 ± 0.60
Peak position (mV)	406 ± 11	379 ± 18	405 ± 80	383 ± 40
Linearity *	0.999	0.995	0.999	0.988

* Coefficient of determination, r^2

value (i.e., 5 µM is the minimum LOD requirement). Moreover, the drop in the linearity of DPV and the maximum sensibility uncertainty has to be forced to be lower than 10 %. Usually, in literature, the voltammetry experiments are conducted with an empirical a priori defined sampling rate of more than some hundred samples per voltammogram [181, 155, 156, 157, 158]. Table 3.1 shows a direct comparison between the empirical approach and the SRO method. Due to the here presented optimisation methodology, the LOD increases but remains in all cases under the imposed maximum. Amazingly the sensitivity scales down to 94 % of the standard with CV method, and 97 % with DPV. Meanwhile, the sampling frequency can be reduced by eight times in the CV and sixteen times in the DPV. Considering the DPV method and SRO approach, this reflects a remarkable reduction down to 6.6 % of the sampling frequency, with an increased LOD but still suitable for the application, losing just 2 % in sensitivity.

3.3 Total Charge Detection in Cyclic Voltammetry

While voltammetry methods exploit online monitoring of patients [156, 102], most of the point-of-care or wearable platforms present in literature usually calculate the drug concentration offline, instead of leveraging on voltammetry techniques for direct determination of concentration [183]. Indeed, the difficulty in point-of-care and wearable systems is to automatically retrieve the final information directly by the electronics limits the application of voltammetry. In fact, it

is usually required to implement a custom digital architecture [184] to quantify the drugs reliably, adopt an operating system-based processor [185], or process the information offline [152]. Unfortunately, all of these techniques require power and area demanding electronic architectures, with a suitable sampling rate [99]. The usage of power and area demanding systems conflicts with the edge-computing paradigm [186] needed for the connected point-of-care or wearable monitoring.

Total-Charge Detection in Cyclic-voltammetry (TCDC) is an innovative measurement method. It is possible to avoid full-voltammogram analysis in drug detection [100]. This approach scales down significantly the complexity at the edge-computing in drug detection systems. The TCDC applies a charge measurement on the top of a standard voltammetry-based procedure to detect, through coulometry, the concentration of the target biological compound. A complete circuit of the TCDC method is fully designed and tested to prove that it is feasible to implement it in consequent medical instrumentations. This section is adapted with permission from [100]

3.3.1 TCDC Method

Amperometric electrochemical detection methods usually rely on the determination of compounds by measuring the faradaic current. Differently, the TCDC measurement method presented here focuses on the total charge exchanged in the electrochemical cell due to the faradic process. The coulometry method (the measurement of the charge) has already been applied for the determination of biological compounds [187]. However, to the best of our knowledge, the measurement of charge has never been applied in the voltammetry method for continuous drug monitoring since standard current sampling in CV is usually exploited [188]. Several electro-active therapeutic drugs can be involved in an electrochemical reaction [159], in which the total net charge exchanged Q_{tot} is defined as the sum of the faradaic process Q_F and the non-faradaic one Q_{NF}, as described in Equation 3.2.

$$Q_{tot} = Q_F + Q_{NF} \tag{3.2}$$

Approximating the Faradaic charge with the Faraday's laws of electrolysis and the non-faradaic charge to the double-layer capacitance effect on the interface [64], then the total charge at the electrochemical interface is:

$$Q_{tot} = nFN + C_dV \tag{3.3}$$

Where n is the number of electrons transferred in the reaction, F the Faraday constant, N the number of moles involved in the reaction, C_d the equivalent capacitance of the double layer, and V the potential applied at the interface. From Equation 3.3 it is possible to derive the calibration equation:

$$Q_{tot} = Q_0 + S \cdot C \tag{3.4}$$

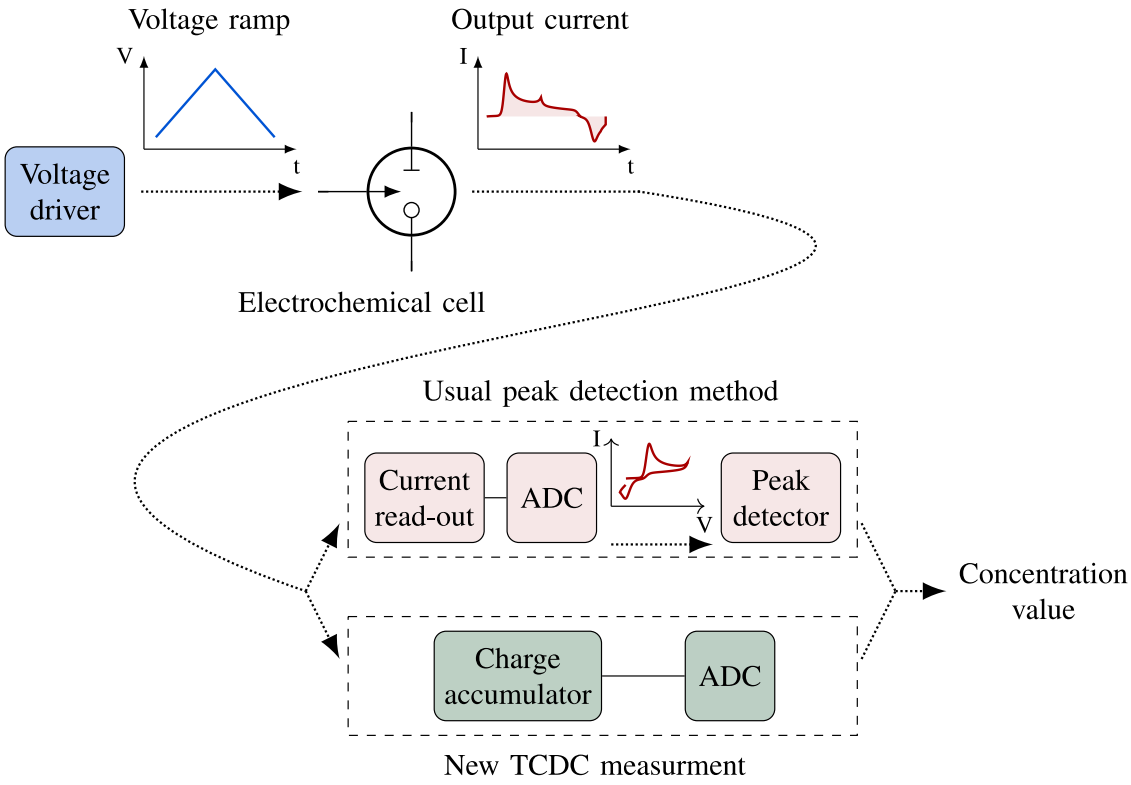

Figure 3.5: In the TCDC measurement method, the total charge is acquired to determine the drug concentration, avoiding computation and oversampling typically needed by the usual peak detection method. Reprinted with permission from [100]. © 2020 IEEE.

which relates Q_{tot} and the concentration of target analyte C. S is the sensitivity defined as Coulomb per Molar (C / M), and Q_0 is the total non-faradaic exchanged charge. To a first approximation, Q_0 does not depend on the analyte concentration, and it can be extracted as a calibration constant.

Figure 3.5 schematically explains the proposed TCDC measurement compared to the usual peak detection method. Both in the standard CV procedure and TCDC, a voltage ramp is applied to the electrochemical cell. In CV, the system samples the output current, although, in TCDC, the circuit accumulates the charge to measure the total net charge exchanged during the whole electrochemical process. Therefore, the TCDC does not require any more oversampling of the current to extract a feature from its shape. The proposed measurement system gives the concentration value directly in a voltage linearly proportional to the target drug concentration. The TCDC methods present a drastic reduction in complexity, eliminating both processing and oversampling in CV techniques, paving the road for several applications where standard microcontroller-based systems are not suitable.

3.3.2 Circuit Implementation

The implementation of the TCDC method requires the development of a single component, which is a charge-to-voltage converter, to accumulate the total charge produced in the electrochemical process. The output of the converter is implemented to input an Analog to Digital Converter (ADC) to get a digital value linearly proportional to the input concentration (as shown in Figure 3.5). The design of the circuit is constraint by the time involving the electrochemical reaction. For example, the time required to perform a CV-detection on paracetamol is around 10 s at an SR of 0.2 V / s [99, 102, 156]. Even though a simple integrator can perform the charge-to-voltage conversion, a standard inverting integrator is not suitable for the TCDC since the long-time constant requires an area-demanding component, usually avoided in any conventional CMOS implementation. Attenuation techniques help to eliminate part of the input charge to reduce the capacitor size [189]. In particular, the parasitic-insensitive Nagaraj integrator [190] exploits the attenuation.

The proposed circuit is fully based on Switch Capacitors (SC), without resistance components, planning a future CMOS implementation. Fig 3.6 shows the implemented TCDC circuit: in the first stage, A_1 operates as Nagaraj charge-attenuator, while in the second stage, A_2 operates as standard SC integrator. Due to a long time of charge accumulation required by the electrochemical drug detection, the Nagaraj topology does not operate as an ideal integrator since the long time constant suppresses its normal operating behaviour. Therefore, the proposed circuit relies on a two-stage circuit with the novelty of taking advantage by [190] to attenuate the input charge and achieve the specific purpose goal. The SCs are controlled by a two not-overlapped phase of the same clock (Φ_1 and Φ_2). During Φ_1, the charge is transferred from C_1 to C_2, and sampled by C_3. In Φ_2, C_1 withdraws the charge stored in C_2, while C_1 redistributes its charge with C_2.

The system is designed to fit a clock frequency of 32.768 kHz, the most widely adopted resonator in low-cost systems [191], and the supply voltage is set to 1.8 V matching the CMOS 180 nm technology for future developments. Considering the first stage, C_2 is equal to 20 fF, while C_1 and C_3 are 70 aF, value slightly above the current size limit of CMOS 180 nm technology [192], minimising therefore the size of the circuit until the technological limit. In the second stage, C_4 is 3 fF, and C_5 is 40 pF to have an equivalent resistance of 10 GΩ, which separates the two stages and avoids leakages. Folded-cascode Operational Transconductance Amplifiers (OTA) implement both operational amplifiers in the design. A process variation analysis selects all the values mentioned above. During the simulation, tolerance values obtained by literature [192] are considered to cover extreme cases and to guarantee the compensation of process variation by clock frequency tuning. Mainly, this analysis is performed on the value of C_1 and C_3 due to their small value. Both capacitor values are tested in the range 70 ± 30 aF, Supposing a typical process

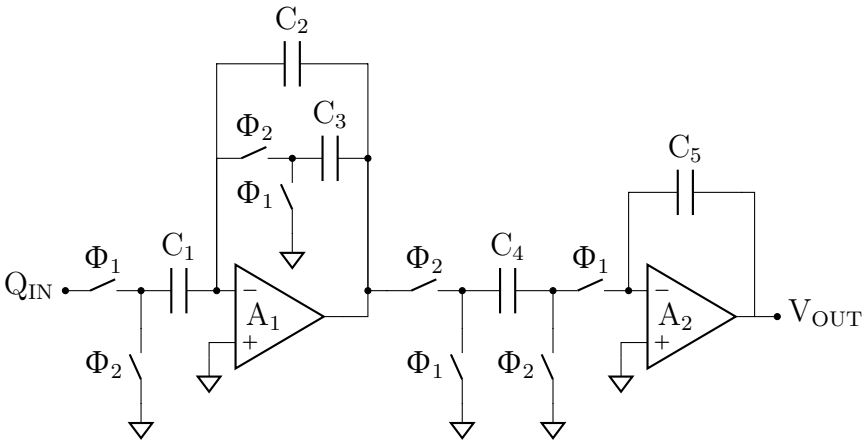

Figure 3.6: TCDC analog read-out circuit implementation. The Nagaraj integrator (A_1) and the SC integrator (A_2) accumulate and convert the total input charge into the output voltage, during the two non-overlapped clock phase (Φ_1, Φ_2). Reprinted with permission from [100]. © 2020 IEEE.

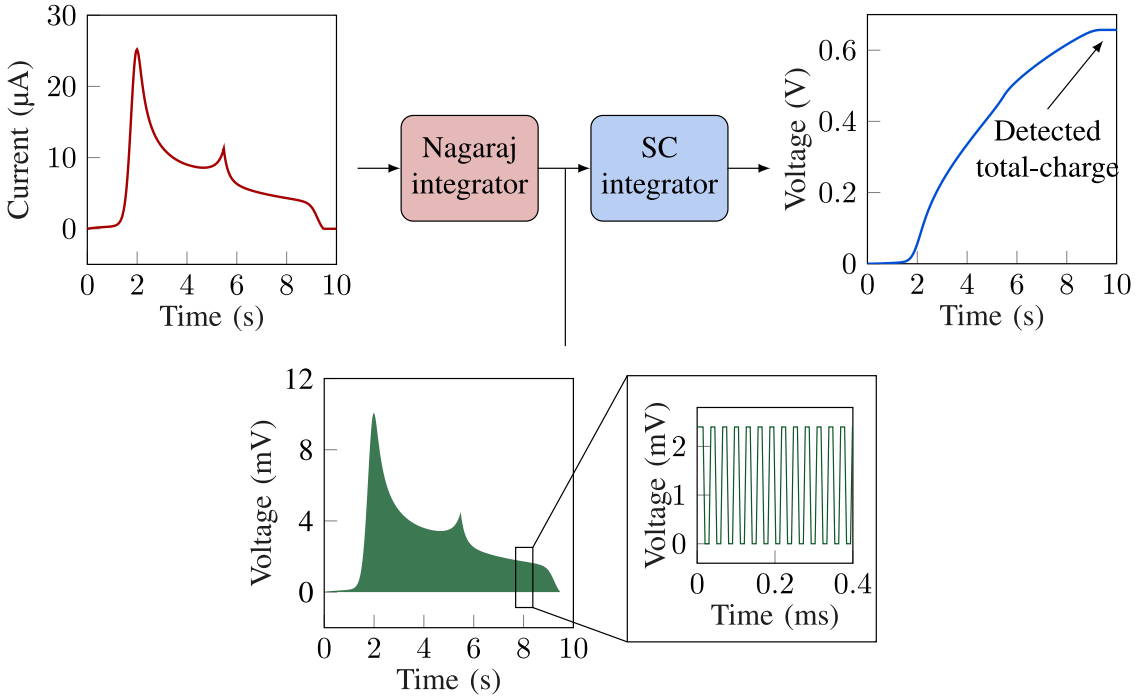

Figure 3.7: TCDC circuit behaviour from simulation. The Nagaraj integrator suppresses partially the input charge while the SC integrator output-voltage is proportional to the total charge. Reprinted with permission from [100]. © 2020 IEEE.

variation of 50 %.

Figure 3.7 presents the behaviour of the proposed TCDC circuit. For the sake

of simplicity, the current produced by the sensor (top left) represents the input charge. The Nagaraj integrator partially suppresses the input charge producing an attenuated switching voltage signal (bottom). The SC integrator accumulates the charge from the beginning of the CV procedure until its end. The maximum voltage reached by the output can be held, sampled, and fed to an ADC as the final detected value of the total charge. The voltage fits the ADC conversion range, avoiding saturation, and can be adapted to a wide range of measures tuning either statically by the component size or dynamically by the clock frequency.

3.3.3 Validation and Performance

Real data sets are collected experimentally in a lab environment to validate the TCDC method and its related circuit implementation. The data are used for both analytical comparisons as well as input for simulating the implemented measurement circuit. The validation is performed using APAP as the selected benchmark, using DropSens DRP-110 SPE and the Metrohm Autolab PGSTAT 302N as detailed in Section 2.2.1. The circuit performs each time a full CV voltammogram at an SR of 0.2 V / s in the voltage range between −0.1 V and 1.1 V. Each measure is repeated three times with a new electrode to consider the experimental variability. The lab instrument samples the current produced by the sensor at a rate of around 33.3 sample / s (400 samples per CV) and stored.

In the simulation of the implemented circuit, the waveforms obtained by the lab measurements are applied as input vectors. The same waveforms are also analytically processed to have a fair comparison with the usual offline methods of peak estimation. The analytical processing of the data is performed in Matlab®, the built-in function findpeaks returns the height of the oxidation peak shown by the voltammogram. Meanwhile, the built-in function trapz mathematically estimates the total charge considering the trapezoidal numerical integration. The electrical simulations are performed with OrCAD® PSpice®, and the output voltage is sampled after 12 s, namely, at the end of the CV excitation.

The data collected through the experiment are analysed to define better the capability and limitation of the proposed TCDC method. The analysis also helps to understand the performance of different possible ranges of charge accumulation in the CV. After simulations, the sensing performances of the proposed measurement circuit are compared with the analytical results obtained with the conventional peak detection method.

According to the definition of TCDC provided in Section 3.3.1, the total charge exchanged in the faradaic process expresses the concentration of the analyte. Figure 3.8 presents the current versus time acquired during the lab test at a concentration of 300 µM. Considering a standard CV, it is possible to define different intervals of integration in time, which are related to different ranges of charge accumulation.

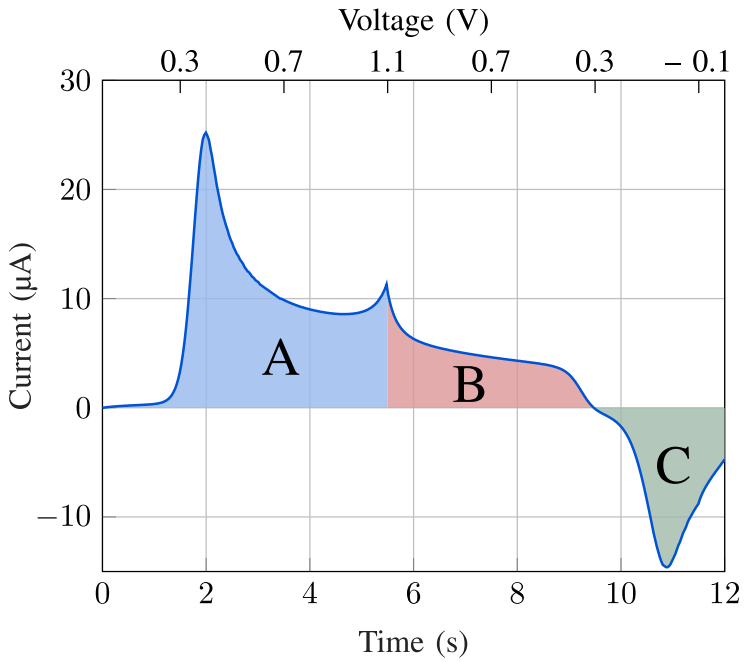

Figure 3.8: Possible range of charge accumulation in applying TCDC. Positive increasing only excitation waveform (A), positive only charge (A+B), natural total charge (A+B–C), or cumulative total charge (A+B+C). Reprinted with permission from [100]. © 2020 IEEE.

The range A is related to the first part of the voltammogram, where the positive-increasing voltage drives the electrochemical cell. The range A+B consider the total positive-only charge in all the voltammogram. Finally, the negative charges highlighted in C can be considered discharge, obtaining the total natural charge in CV (range A+B–C) or adding a rectifier as another additive charge, obtaining the cumulative total charge (interval A+B+C). Circuit with few components may implement all the interval, with an integrator and optionally the addition of current mirror.

Table 3.2 compares the possible interval of charge accumulation considering the sensitivity (as Coulumb per Molar, S, in the Equation 3.4), offset (Q_0 in Equation 3.4), linearity, and LOD. The sensitivity increases, enlarging the range of integration, presenting its maximum in the interval A+B+C. The regression coefficient of the obtained calibration curve evaluates the linearity, and the increase in the accumulation time does not affect this parameter. The LOD represents the minimum concentration of drug the system can detect. In this thesis, the LOD has been evaluated as three times the standard deviation of the measure, divided by the sensitivity. The results demonstrate that the application of the TCDC at the interval A+B–C, which is the total charge exchanged during the CV, presents a

Table 3.2: Comparison between possible range of charge accumulation in TCDC measurement method. Reprinted with permission from [100]. © 2020 IEEE.

	A	A+B	A+B–C	A+B+C
Description	Increasing positive only CV	Positive-only charge	Natural total charge	Cumulative total charge
Sensitivity (nC/µM)	144.7 ± 1.3	207.8 ± 2.8	155.3 ± 6.5	260.7 ± 6.8
Offset (µC)	5.27 ± 1.52	5.59 ± 2.57	3.92 ± 2.45	7.26 ± 2.70
Linearity (r^2)	.99997	.99997	.99997	.99997
LOD (µM)	5.55 ± 0.08	5.30 ± 0.09	8.96 ± 0.38	5.34 ± 0.15

Table 3.3: Comparison between peak detection method and TCDC, both analytical and simulation results. Reprinted with permission from [100]. © 2020 IEEE.

	Peak detection*	Total charge*	TCDC circuit
Sensitivity	51.7 ± 9.2 nA/µM	207.8 ± 2.8 nC/µM	1.97 ± 0.03 mV / µM
Offset	0.15 ± 0.15 µA	5.59 ± 2.57 µC	66.4 ± 9.0 mV
Linearity (r^2)	0.99970	0.99997	0.99994
LOD	1.93 ± 0.94 µM	5.30 ± 0.09 µM	6.09 ± 0.12 µM

* Matlab® analytical results.

considerable reduction of performance, showing a 69 % increase in the LOD. Meanwhile, the interval A+B, which is the accumulation of positive-only flowing charge, presents the best performance. For this reason, all simulations and the following considerations are then conducted considering the positive-only charge. Moreover, this choice is fully compatible with the circuit implemented and described in Section 3.3.2 since the A+B interval requires detecting a charge via a current flowing in one direction only. The addition of a diode will allow canceling area C directly. The circuit to implement accumulation of interval A requires the introduction of a controller or a threshold comparator to stop the accumulation at the end of A. Meanwhile, both interval A+B–C and A+B+C, requires a circuit for considering a current flowing in the opposite direction. Namely, the interval A+B–C requires subtracting the charge in area C; interval A+B+C requires the addition of a full rectifier bridge to invert the charge in area C and continue to accumulate it.

Figure 3.9 displays a comparison in the calibration curves obtained by both

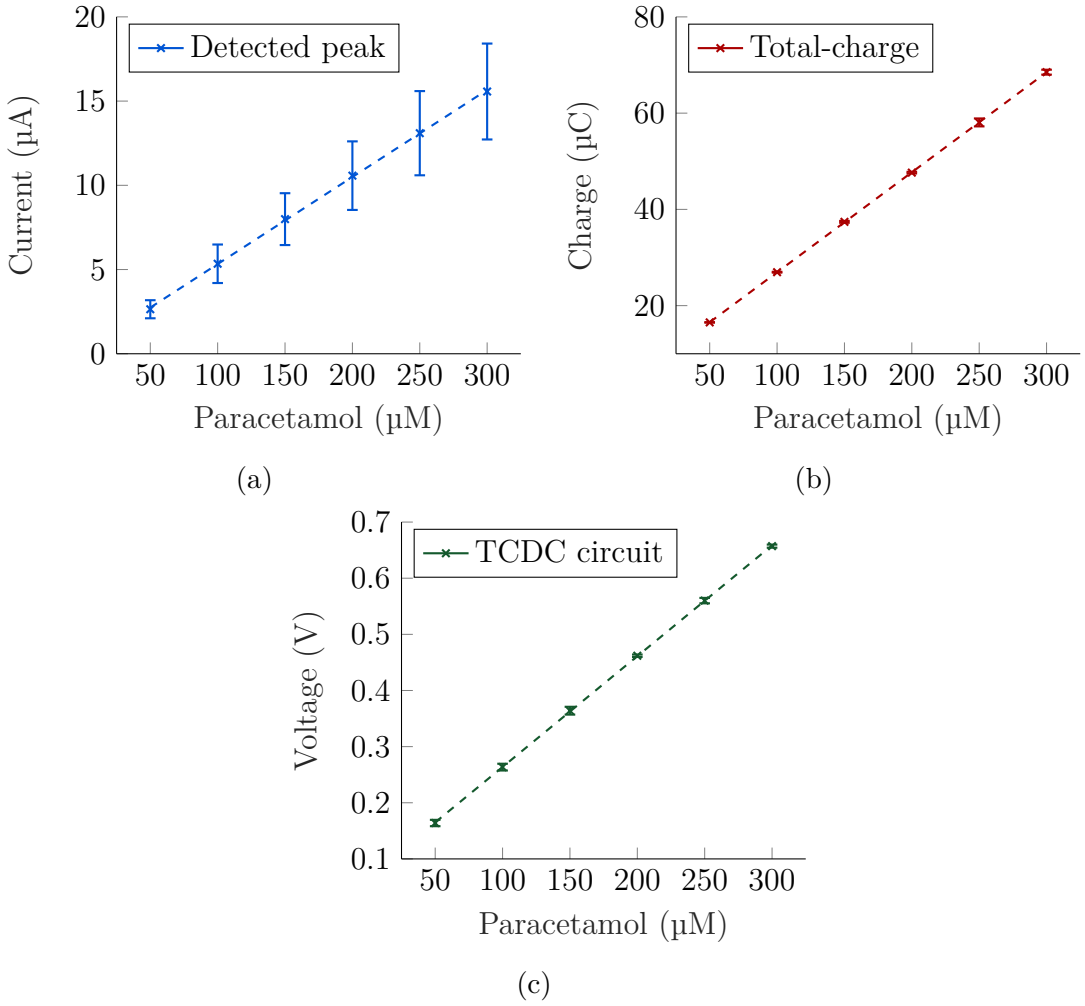

Figure 3.9: Calibration curves obtained by extractionon of current peak (a), analytical total charge (b), and TCDC circuit simulation (c). In (b) and (c), the uncertain is really small and it is hard to recognise in the graph. Reprinted with permission from [100]. © 2020 IEEE.

analytical processing and simulation. Namely, Figure 3.9a shows the resulting calibration obtained by measuring the paracetamol concentration with the extraction of the current peak. In contrast, Figure 3.9b displays the analytical computation of the total charge as integral of the current flowing in the electrochemical cell. Instead, Figure 3.9c presents the calibration curve obtained by performing the TCDC circuit simulation. As clearly evident in Figure 3.9, all the method is suitable to calibrate linearly with the sensor data.

Table 3.3 compares the detection performance in terms of sensitivity, offset, linearity, and LOD. The sensitivity can not be compared in absolute terms due to

different outputs obtained by the same transducer, and the same is valid for the offset. On the other hand, linearity is the first indicator of the performance of the TCDC method since it presents an increase from 0.99970 up to 0.99994, with respect to the peak detection method. Applying the TCDC method, the LOD increases due to the trade-off between the proposed dramatic reduction in complexity and the quality of the measure. The LOD increases because TCDC collects all the charge in the CV, therefore, acquiring a higher background noise related to the non Faradaic phenomena [64]. Although, the increase of LOD can be kept under control since it is limited approximately to 2.2 times with respect to peak detection by conventional methods. The LOD always remains one order of magnitude lower than the typical minimum pharmacological concentration. Therefore, the quality of the measurements is not compromised in the case of the proposed application. Moreover, the proposed method significantly reduces the error on the single drug measure (defined as a statistical error, that is three times the standard deviation), clearly visible directly in Figure 3.9. Namely, the presented approach scales the measurement error down from 17.8 % to just 1.7 % because of the higher obtained sensitivity, reflecting on a higher resolution.

3.4 Propofol Fouling Machine learning

For an ANN-based ML technique, some key components that may be extracted from a cyclic voltammogram are peak position, height, and area, peak width half-height, peak sum of derivatives together with the initial setup parameters. These elements are successfully quantified in an ANN that is trained to detect the concentration of Potassium Ferricyanide, which is marked by a solid non-linear response, on graphite pencil electrodes [169].

This thesis proposes a novel Machine Learning (ML)-based calibration method to compensate for the fouling effect described in Section 2.2.3, developing the new Propofol Fouling Machine learning (PFM) classifier. The PFM is implemented to identify the correct concentration of propofol in a given sample to contribute to developing a system for closed-loop controlled infusion of anaesthetic. The PFM classifier is designed, as well as its parameters are optimised using a large dataset of 480 samples acquired in PBS buffer. Later, the model is validated with a smaller, still representative, dataset of 120 samples for direct monitoring of propofol in undiluted human serum. The training of the classifier is performed with data sourced from the corresponding dataset. This section is adapted with permission from [101].

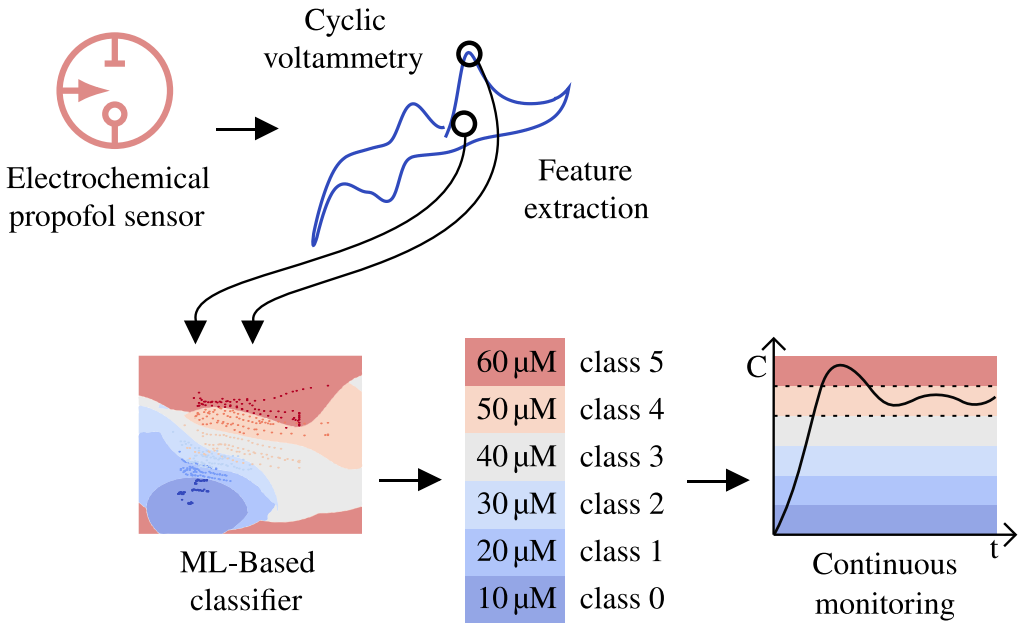

Figure 3.10: Proposed ML-based approach for continuous monitoring of propofol: from left to right, the sample is analysed through electrochemical sensors and CV to extract relevant features to be fed an ML-based classifier that determines the range of concentration of the propofol, compensating the fouling effect. Reprinted with permission from [101]. © 2020 Elsevier B.V. All rights reserved.

3.4.1 PFM Method

Recent works suggested that monitoring controlled-delivery of anaesthetics may be achieved with a 10 % accuracy around the target concentration, and with one measurement every 30 s, continuously in time, while the therapeutic concentration of propofol ranges between 0.25 mg / l and 10 mg / l (1 : 60 µM) [5]. The goal of the ML-based approach is to develop a technique suitable for the continuous measurement of propofol concentration every half a minute and able to discriminate the concentration level lower than 12 µM. Figure 3.10 presents the proposed PFM method. Through an electrochemical sensor and CV technique, the redox of propofol is analysed. From the voltammogram, several peculiar features are extracted and fed to the ML-based classifier. The classifier determines the concentration level of propofol in the sample in classes, compensating fouling of propofol. According to the requirements, the therapeutic range is subdivided into classes representing concentration levels of 10 µM. The PFM provides the anesthesiologist with a tool for the direct determination of propofol concentration in human serum. Compared to a regressor, the classifier directly provides the information required to maintain the constant dose in the range of interest.

The lab instrument Metrohm Autolab PGSTAT 302N is interfaced to the propofol PGE needle-shaped sensor described in Section 2.3 to develop the PFM and validate its performance. With the chemicals and materials described in Section 2.2.2, the samples are prepared with seven concentrations of propofol, equally spaced in its therapeutic range: 10 µM, 20 µM, 30 µM, 40 µM, 50 µM, and 60 µM. The samples for primary analysis, and the training and testing sets for the ML classifiers are prepared in PBS at pH 7.4. It worth noting that the procedure is not formally cyclic because the proposed method entails that the fouling is limited to its minimum. Cycling the voltage scan more than one time per measure would catastrophically reduce the lifespan of the sensor. The sensor can compensate fouling in real-time, at a fixed concentration of the analyte in its therapeutic range. For this reason, all the samples are measured twenty consecutive times, with an interval time of 30 s, to be consistent with the continuous monitoring target of this thesis.

3.4.2 PFM Implementation

Non-linear classifiers are considered to develop the PFM in order to model the non-linearities introduced by the fouling on the sensor. Kernelised-Support Vector Machine (SVM) ML methods are suitable for non-linear classification problems by constructing the optimal hyperplane in the features space induced by a kernel function [193]. The SVM predicts the class concentration of propofol analysing the unknown samples according to the mathematical distance of the samples to the training instances. All processing stages and algorithms are implemented within a Python 3.7.4 environment, using NumPy and scikit-learn libraries [194].

Let $X = \{x_i\}_{i=1,\cdots,m}$, with $x_i \in \mathbb{R}^n$, denote the input tensor of m samples and n features. Let $y \in \mathbb{R}^m$ denote the vector labelling the propofol concentration of each measurement, where each target concentration (10 µM, 20 µM, 30 µM, 40 µM, 50 µM, and 60 µM) is encoded into a categorical class with values from zero to five. The objective of the six-class classifier is to construct a predictor based on the training set (X_{train}, y_{train}) that can divide the input features space into a collection of regions belonging to each class. The decision boundaries are refined in the training process, for which the metric used is the classification accuracy:

$$accuracy = \frac{\#\ correctly\ predicted\ test\ samples}{\#\ test\ samples} \tag{3.5}$$

During inference, the predicted class indicates the range of concentration of propofol in the sample.

In kernelised-SVMs the optimisation objective is:

$$\begin{aligned} \min_{\alpha} \quad & \frac{1}{2}\alpha^{\mathrm{T}} \cdot M \cdot \alpha - e^{\mathrm{T}} \cdot \alpha \\ \text{subject to} \quad & y^{\mathrm{T}} \cdot \alpha = 0, \\ & 0 \leq \alpha_i \leq C,\ i = 1, \cdots, m, \end{aligned} \tag{3.6}$$

where M is an m by m positive semi-definite matrix:

$$M_{ij} = y_i \cdot y_j \cdot K(x_i, x_j) \tag{3.7}$$

and

$$K(x_i, x_j) \equiv \phi(x_i)^{\mathrm{T}} \cdot \phi(x_j) \tag{3.8}$$

is the equation defining the SVM kernel, e is a vector of ones of length m, C is a regularization hyperparameter tuning the tolerance of margin violations. Linear, polynomial, Gaussian Radial Basis Function (RBF), and sigmoid kernels are investigated. The training instances are shuffled, and ten-splits cross-validation is performed, where the metric used is the prediction accuracy based on decision boundaries. The ten splits are stratified to preserve the number of samples per class in each training and validation split (80 % / 20 %). An analysis is carried out to assess how the type of kernel and the features to be considered in the dataset influence SVM performance. Then, a cross-validation grid search on the kernelised-SVM hyperparameters is carried out to optimise the classifier. Finally, the classification performance of the optimal SVM is evaluated on the test set. The LIBSVM library is used [195], where a one-versus-one scheme is adopted for the multi-class classification.

The dataset consists of $m = 480$ samples acquired from four different sensors in PBS and $m = 120$ samples obtained in human serum. The dataset in PBS is extended with respect to the human serum analysis in order to improve the optimisation process of the ML-based algorithm and its parameters. The two datasets are kept separated from each other; the training and validation are performed on PBS on one side, on serum on the other side. Each recorded sample is a voltammogram relating the current measured in function of the potential applied to the electrochemical cell. The voltammograms acquired from propofol measurements at known concentrations are analysed in order to extract three relevant features: the peak current, the potential at peak current, and the total charge. The peak Faradaic current i_p is the current resulting from primary propofol oxidation, removing the baseline charging current. E_p is the cell potential at which the peak current is achieved. i_p and E_p are the most relevant features for characterizing the electrochemical measurements [133]. Moreover, the integral of the voltammogram in the window between 0 V and 0.7 V is computed. The latter is the total charge exchanged during primary propofol oxidation, denoted as Q, that is proved to be relevant in the determination of drugs [100]. Lastly, the ordinal number of measurements performed with the same sensor, n_{meas}, is added to the feature list. The input features matrix X is first standardised by removing column mean and scaled to unit variance. This is of paramount importance since the features have different unit scales. The dataset is then split into a training and test set of ratio 80 % / 20 %.

Several experiments and analyses are carried out to implement the best PFM classifier. Namely, the optimal kernel is selected, the best set of features is defined,

Table 3.4: Selection of the appropriate kernel for PFM: comparison among different kernelised-SVMs in i_p and E_p features space with their default hyperparameters. The best results are achieved with RBF-SVM. Reprinted with permission from [101].

Kernel type	Linear	Polynomial	RBF	Sigmoid
Kernel function $K(x_i, x_j)$	$x_i^{\mathrm{T}} \cdot x_j$	$(\gamma \cdot x_i^{\mathrm{T}} \cdot x_j + r)^d$	$\exp(-\gamma \lVert x_i - x_j \rVert^2)$	$tanh(\gamma \cdot x_i^{\mathrm{T}} \cdot x_j + r)$
Kernel hyper-parameters	-	$\gamma = 1/m$, $r = 0$, $d = 3$	$\gamma = 1/m$	$\gamma = 1/m$, $r = 0$
Soft-margin penalty parameter	$C = 10$	$C = 10$	$C = 10$	$C = 10$
Classification accuracy	43.8 %	86.5 %	90.6 %	33.3 %

and the classifier's parameters are optimised. The experiments for defining the best type of ML network are performed with the dataset obtained from the 480 samples in PBS buffer. Such a stable buffer may facilitate identifying the best ML model for the compensation of propofol fouling.

Kernel selection The selection of the most appropriate kernel for the PFM is exploited by implementing linear, polynomial, RBF, and sigmoid SVMs with their default hyperparameters. The classifier's decision boundaries are constructed from the training set in the space built by the combination of standardised peak current and standardised potential at peak current (i_p and E_p space). The latter are the main features to characterize propofol electrochemical measurements. The different classifiers are trained with ten-splits cross-validation on the training set and evaluated on the test set. The four different kernel functions, the kernel hyperparameters, and their classification performance are reported in Table 3.4. The decision boundaries of each kernelised-SVM are visualised in Fig 3.11. Linear and sigmoid kernels are not suitable for detection of propofol (see Table 3.4). Meanwhile, non-linear kernels enable computing the decision hyperplanes in the space of higher dimension. Polynomial and RBF are the most accurate kernels, and the decision boundaries are smoothly separating the classes. RBF kernel is chosen for the subsequent experiments since it yields a higher classification accuracy of 90.6 % on the test set.

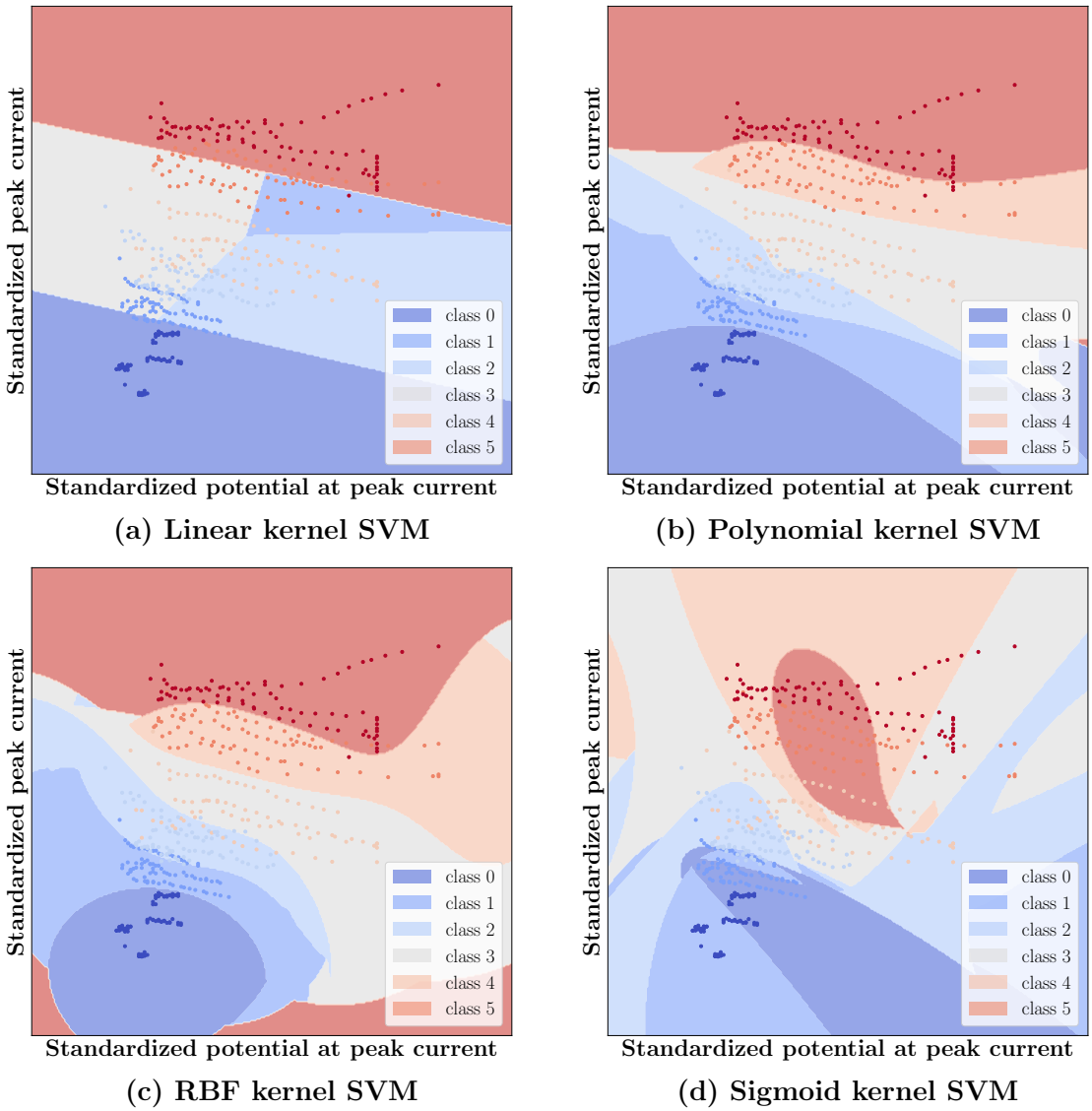

(a) Linear kernel SVM

(b) Polynomial kernel SVM

(c) RBF kernel SVM

(d) Sigmoid kernel SVM

Figure 3.11: Kernelised-SVM implemented with: linear (a), polynomial (b), RBF (c), and sigmoid kernel (d), represented by the features space peak current and potential at peak current. The spaces are colour-mapped according to the class predicted by the classifier, highlighting the decision boundaries and each sample is colour-mapped to its target class in order to assess classification accuracy. It can be seen that the samples cannot be linearly separated in the original features space. The polynomial curves present on the graphs the best boundaries considering SVM with different kernels. Reprinted with permission from [101].

Features selection Different combinations of input features are evaluated on the RBF-SVM. This optimisation helps to understand the effect of the different

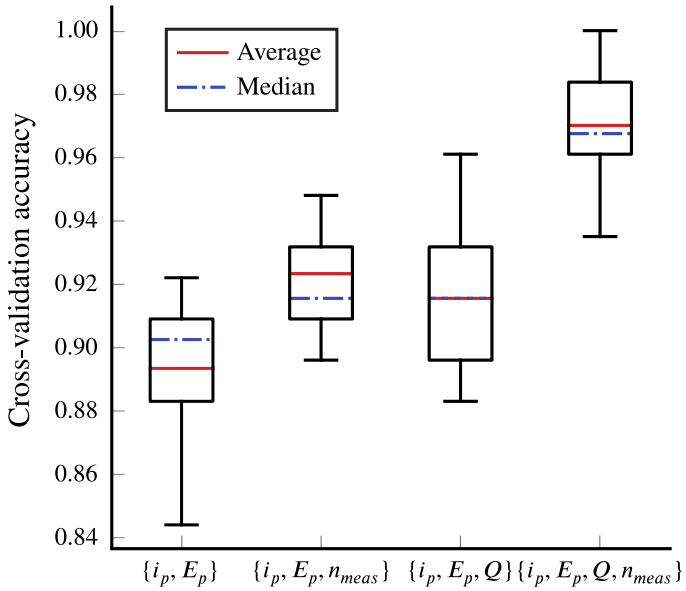

Figure 3.12: Cross-validation classification accuracy of RBF-SVM trained with four combinations of input features. The box plots extend from lower to upper quartile values of cross-validation accuracy, with median (dotted blue line) and average (red line), and whiskers show the range of classification accuracy. The complete set of feature $\{i_p, E_p, n_{meas}, Q\}$ shows visibly an higher accuracy, that cannot be reached with less features. Reprinted with permission from [101].

features extracted from the voltammograms on the classification accuracy of the ML model. The possible combinations of features considered are $\{i_p, E_p\}$, $\{i_p, E_p, n_{meas}\}$, $\{i_p, E_p, Q\}$, and $\{i_p, E_p, n_{meas}, Q\}$. All the different input sets are fed to the classifier, and a ten-splits cross-validation is performed on the training set. The cross-validation accuracies are presented in Figure 3.12 with a whisker plot. It highlights that classification accuracy scales with the amount of features included in the dataset. Indeed, it could be noticed from Figure 3.11 that samples belonging to classes two and three are mis-classified in features space of i_p and E_p, since the samples are intermingled. Besides, for the set of features $\{i_p, E_p, Q\}$, classification accuracy is more dispersed, and it is lower than using n_{meas} instead of Q. There is a high correlation between the charge exchanged during propofol oxidation and the peak oxidation current. Significant improvement in cross-validation accuracy is observed when the training set contains all four features, reaching 0.970 ± 0.020.

Hyperparameters optimisation RBF-SVM hyperparameters are tuned through cross-validation grid-search in order to optimise the hyperparameters of proposed ML model. The non-linear coefficient γ is swept from 10^{-9} to 10^{3}, while the soft

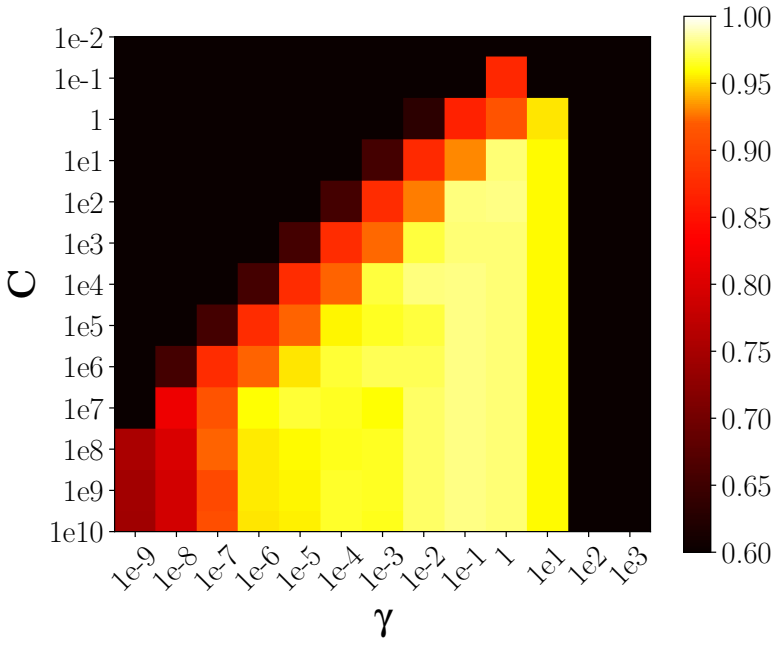

Figure 3.13: Heatmap of cross-validation accuracy as function of RBF-SVM hyperparameters C and γ, highlighting the parameters space yielding the most accurate classifiers (yellow regions), $C = 100$ and $\gamma = 1$. Reprinted with permission from [101].

margin penalty parameter C is swept from 10^{-2} to 10^{10}. Both sweeps are performed on a logarithmic scale, training 169 SVM models. The training set (X_{train}, y_{train}) comprising the four features is shuffled, and ten-splits cross-validations are implemented. The training and validation accuracies are computed for each split. Their average value is retained for classifier comparison. Figure 3.13 displays the heatmap of the cross-validation accuracy on hyperparameters, highlighting the hyperparameter space yielding the most accurate classifier. It is observed that the support vectors are not able to separate the samples for large values of γ. They influence very few training instances. Conversely, a low value of γ over-constrains the classifier model, that ends up behaving like a linear classifier. The classifier does not capture the complexity of the non-linear dataset. As for the soft-margin penalty parameter C, a lower value is preferred to reduce over-fitting trading-off accuracy. Larger values for C tend to generalize better, but maximum accuracy is reached for $C = 10^4$, and it does not improve beyond. RBF-SVM models with C lower than 10^4, and yielding cross-validation accuracy above 97.5 % are evaluated on the test set. RBF-SVM with parameters $C = 100$ and $\gamma = 1$ yields classification accuracy of 98.9 %.

3.4.3 Validation and Performance

The validation of PFM is implemented first, discussing the sensor's performance for propofol detection through standard metrics to show the limitation of a linear model in the given application. Later, the performance of the proposed PFM method is characterised on human serum, repeating the training on the serum dataset too, to validate the method in the target application. The final testing is done with accurate and undiluted human serum with propofol in the therapeutic range at body temperature, which artificially mimics the infusion of anaesthetics in the clinical environment. The samples for classification in human serum are prepared in undiluted human serum, heat-inactivated from human male AB plasma, from Sigma-Aldrich®, and they are continuously kept at 37 °C by a hot plate stirrer.

Figure 3.14 presents the resulting voltammogram obtained by repetitively acquiring the Faradaic current in a sample of 60 µM of propofol, considering PBS (Figure 3.14a), and human serum (Figure 3.14b) as background. Even though both the sensor and the propofol concentration are not varying, the curves are radically varying. Figure 3.14a illustrates fouling on the carbon surface of the electrode in PBS. Namely, with every new measurement, the fouling layer increases on the interface, reducing the primary oxidation peak (A) height and shifting the peak itself to the right. Peak B and C are substantially changing in time, similarly to A, presenting fouling as well. In this thesis, the analysis focuses on the primary peak A, which is the best candidate to determine propofol concentration due to higher magnitude, which improves sensitivity, and higher distance from other peaks, enhancing selectivity.

Figure 3.14b shows a detail of peak A in the undiluted human serum, obtained by baseline subtraction and filtering. The human serum contains proteins completely absent in PBS, which embed and adsorb the propofol. For this reason, the free propofol detectable in serum is lower than in PBS, resulting in reduced Faradaic current, signal strength, and reduced sensitivity [147]. As expected, the current peak is lower (one fifth), and the passivation due to fouling is again visible.

The full dataset acquired is elaborated to extract the sensor calibration according to the linear model commonly used in electrochemical sensors [99] to evaluate the limitation introduced by the fouling phenomenon. The calibration relates linearly the primary oxidation current peak and the propofol concentration recalling the Randles-Ševčík equation [133]. The calibration is performed using 80 % of the samples to be consistent with the ML-based method. The linear calibration procedures resulted in a sensor with a sensitivity of 162.9 ± 10.3 nA / µM and a LOD of 2.4 ± 0.1 µM with PBS as samples medium. In human serum, the sensor presented a sensitivity of 28.8 ± 7.7 nA / µM and LOD of 4.9 ± 1.3 µM. The sensitivity is calculated as the coefficient of regression through linear regression fit. At the same time, LOD is computed as three times the standard deviation of the blank signal around the peak, over the sensitivity [129]. Both sensitivity and LOD variations are

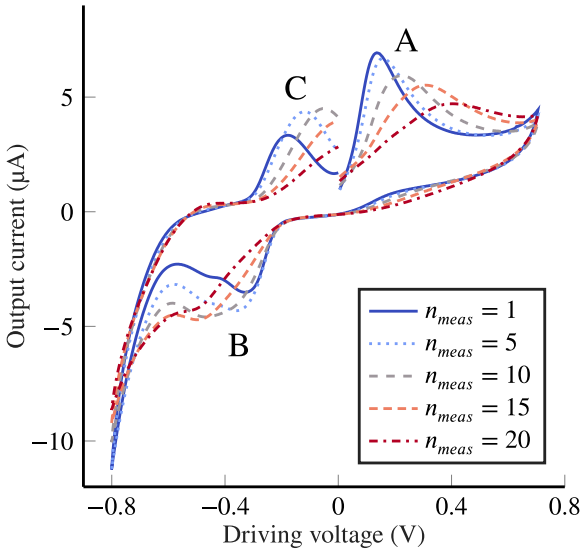

(a)

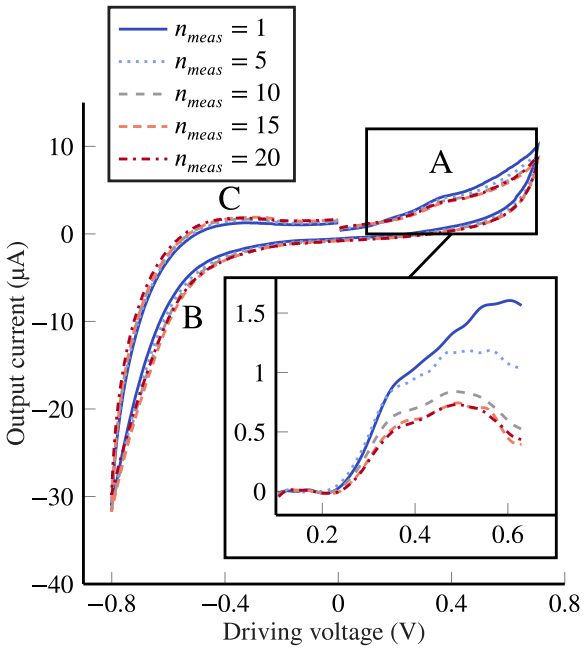

(b)

Figure 3.14: Voltammogram from continuous propofol detection at fixed 60 µM in PBS (a), and in human serum (b). In human serum, the peak is graphically highlighted by baseline subtraction, and filtering since the lower free concentration of propofol reduces its visibility. The peak A lowers in current after each new measurement due to the fouling phenomenon in both cases. Reprinted with permission from [101].

computed with the residual sum of squares of three times the standard deviation of each observation.

Despite being promising, the two extracted linear calibrations present their limits only when considering the measurements in time. Reporting the linear model to a six-classes classifier, similarly to what the PFM does, the classification accuracy tested on the remaining 20 % of the samples are 69.8 %, and 33.3 % in PBS and human serum, respectively. This analysis proves that it is impossible to develop a system for continuous monitoring of propofol concentration without compensating the non-linear fouling effect with a non-linear model.

After selecting the best ML-based model for propofol fouling compensation in PBS buffer, the proposed PFM is validated in undiluted human serum at the body temperature (37 °C). The CV dataset from propofol measurement in human serum is pre-processed as the dataset from PBS. The column mean-centring and standardization to unit-variance are applied, and the dataset is split into training/test sets of ratio (80 % / 20 %). All four features $\{i_p, E_p, n_{meas}, Q\}$ are sent to the classifier and a cross-validation grid-search is carried out for the optimisation of the hyper-parameters C and γ. The RBF-SVM models yielding cross-validation accuracy superior to 94.0 % are selected and evaluated on the test set. The same RBF-SVM which obtained the higher performance in PBS (with $\{C = 100, \gamma = 1\}$), yields the best results also in human serum. The maximum classification accuracy achieved by the PFM in human serum is 100 %, with a null generalization error. The lower error and higher gain achieved by the PFM in serum with respect to the PBS is justified by the smaller dataset, 120 samples for human serum and 480 samples for PBS.

Figure 3.15 displays the results of the validation carried directly in undiluted human serum, in the form of confusion matrices, which presents the prediction accuracy graphically. As visible in Figure 3.15a, the standard linear model features a classification accuracy of 33.3 %, leading to a wrong estimation of the concentration in 66 % of the cases. Meanwhile, the proposed ML-based model with the RBF-SVM classifier (Figure 3.15b) compensates the fouling resulting in an accuracy of 100 %. This result proves that the sensor is suitable for continuous monitoring of propofol for up to ten minutes, with one sample every 30 s, discriminating concentration levels of 10 µM.

Previous works had proven that it is possible to detect propofol with small LOD with inexpensive and disposable sensors [146]. At the same time, [5] opened the need for sensors for continuous monitoring of anaesthetics for improved Therapeutic Drug Monitoring (TDM)-assisted anaesthesiology practice. [145], and [129] faced the problems of fouling and electrode-passivation in continuous measurement of propofol using new materials and new mechanical procedures. In this thesis, it is instead demonstrated that the difficulties of using standard linear models in continuous measuring of propofol while, on the other hand, a novel soft-modeling-based solution to compensate via ML-based method the problem of fouling is proposed.

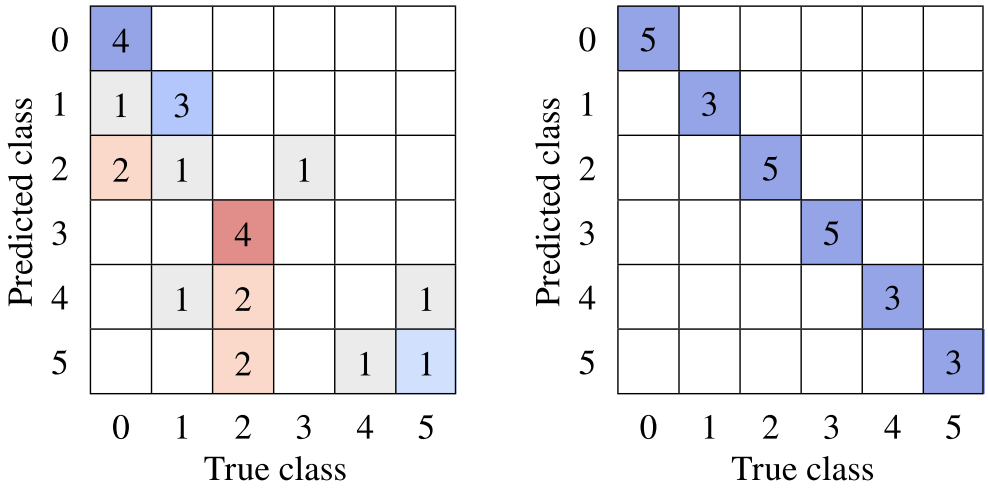

Figure 3.15: Results of validation in undiluted human serum: the confusion matrices show the difference between real concentration (true class) and the concentration estimated (predicted class). While the standard linear model (a) leads to wrong estimation 33 % of the time, the proposed ML-based model (b) always outputs a correct result. Reprinted with permission from [101]. © 2020 Elsevier B.V. All rights reserved.

Table 3.5: Comparison of detection limit with respect to the state-of-the-art. The proposed method trades off a slight increase in LOD with continuous measurement capability. Reprinted with permission from [101]. © 2020 Elsevier B.V. All rights reserved.

Reference	LOD	Continous measurement*
[134]	$3.2 \pm 0.1\,\mu M$	no
[146]	$0.1\,\mu g\,/\,ml$ ($\approx 0.5\,\mu M$)	no
[136]	$2.4 \pm 0.5\,\mu M$	no
This thesis	$4.9 \pm 1.3\,\mu M$	yes

*Without human intervention.

The proposed sensor itself features LOD of $4.9 \pm 1.3\,\mu M$ in real, undiluted human serum, which is ten times more than the LOD reached by [146] but still below the minimum concentration of interest ($10\,\mu M$). More comparisons on the LOD with respect to the state-of-the-art are shown in Table 3.5. The kernelised-SVM is proven to be optimal for compensating the problem of fouling since it reaches 100 % of accuracy in real, undiluted human serum at steady 37 °C in discriminating

10 µM of propofol. Moreover, extensive experiment and optimisation demonstrated that the best kernel for SVM in this application is RBF, with the best parameter set to $C = 100$ and $gamma = 1$, considering as input feature the Faradaic primary current peak (i_p), the potential at the current peak (E_p), the total charge exchanged during Faradaic process (Q), and the ordinal number of measurements performed with a given sensor since it was new (n_{meas}).

3.5 Summary and Main Original Contributions

The results demonstrated how SRO (Sample Rate Optimization) methods could balance the performance to appropriate sampling rate and power consumption in voltammetry-based electrochemical sensing. Lowering the sampling rate, the device's power consumption diminishes, helping the realization of optimised electronic platforms able to provide non-invasive real-time point-of-care bio-sensing, targeting IoT and wearable applications. In particular, this work established that it is possible to develop a method to reduce the sampling frequency maintaining all the sensing performance in the range of the system requirements. A novel measurement method for drug detection is introduced, called TCDC (Total Charge Detection in Cyclic voltammetry). The novel TCDC method provides better calibration (higher linearity and tenfold measurement error reduction) due to an edge-computing lower-complexity method that removes both processing and oversampling, trading off a slightly more than doubled LOD. Hence, the proposed method fits the requirement for point-of-care and wearable real-time monitoring. Finally, the PFM (Propofol Machine Learning) is developed: a novel ML-assisted method to compensate the fouling effect of propofol on electrochemical sensors to improve the anaesthesiology practices. Through extensive analysis, this thesis demonstrated that the proposed model based on Gaussian RBF-SVM helps to obtain high classification accuracy (higher than 98.9 %) both in PBS and in human serum. The new PFM method discriminates 10 µM concentration with 100 % classification accuracy, directly in undiluted human serum at body temperature, and continuously up to ten minutes to meet the requirement for the development of a system for closed-loop controlled-infusion of anaesthetics. Future work will include implementing the proposed model in a portable electronic device for continuous monitoring of anaesthetics and its test with clinical samples.

Chapter 4

Smart Electronic Pen

In this thesis, the first complete electronic pen device for continuous real-time detection of propofol concentration in human serum is developed to address the request of a device for monitoring anaesthetics toward safer anaesthesiology practices. The system is fully characterized and tested for the classification of propofol concentration in the therapeutic range between 10 µM and 60 µM in human serum at 37 °C.

In this section, the full electronic pen for the detection of anaesthetics is presented. The electronic is tailored to interface the needle-shaped sensor (Chapter 2) and implement the measurement methods of Chapter 3. The pen must contain a sensor, a voltage driver, a current reader, a sampling strategy, and a processing tool [59] to detect and display the concentration of anaesthetics correctly. The potentiostat (which implements the voltage driver and the current reader) is developed by designing the first-ever proposed Quasi Digital (QD) potentiostat (Section 4.2), which helps reducing power consumption of the system, with a novel and smart event-based design. Section 4.3 displays the embedded device and its case, which is the main piece of electronics of the pen. It features a Bluetooth® battery-operated Printed Circuit Board (PCB), running a custom firmware, enclosed in a 3D printed case. In Section 4.4, the complete system is presented, grouping and detailing all the novel components developed in this thesis. Finally, a direct comparison between the smart electronic pen with respect to the state-of-the-art is provided.

4.1 State of the Art

A recent publication suggested that better control over propofol delivery is achieved with one measurement every half a minute, in the therapeutic range, i.e., between 10 µM and 60 µM of propofol, and with 10 % accuracy around the target concentration [5]. Although numerous sensors have been proposed in literature for detecting and measuring propofol, achieving high sensing performance [146], they are disposable sensors for single-use blood-spot sampling [62], and they are inefficient in an automatic Therapeutic Drug Monitoring (TDM) closed-loop system. Electrochemical determination of propofol suffers from the so-called fouling phenomena, limiting stability over time of the sensor. The electrochemical oxidation of propofol produces free radicals forming a polymeric film [135] that covers the electrode and degrades the signal [137]. In the works described in [196, 129], solutions to cope with the propofol fouling of electrodes with specific materials are presented, without any sensor for in-situ detection. In addition to the sensor, a system allowing the monitoring of anaesthetics must include a potentiostat, i.e., the set of electronic components required to drive and read the electrochemical sensor [59]. Several circuits have been proposed for this purpose, but without considering long-time detection of propofol [115, 156]. The systems proposed in the literature to monitor anaesthetics are usually bulky and power hungry [3], limiting their application in the surgery room. Moreover, smart data processing and display are generally missing.

Stradolini et al. proposed a complete system consisting of a fluidic chamber-based device to detect anaesthetics on the sensing site. This is connected to a custom electronic system driven by a Raspberry-Pi single-board computer. Finally, a novel Android-based IoT connected this system to the cloud to help the anaesthesiologist to be constantly aware of the patient sedation [3]. This system contains all the components for being a good candidate for a system for TDM of anaesthetics. However, unfortunately, it is still bulky, power-consuming, and not portable, all limitations that this thesis can solve. The main limitation is that it contains a fluidic chamber [3] which is bulky and requires a consistent quantity of blood (around 10 µl / s). In this work, the needle-shaped sensor avoids the necessity of a fluidic device which presents limitations also related to cloths. The electronics in [3] is power-hungry and contains a wired connection to a single-board computer (Raspberry-Pi). Meanwhile, the presented system contains an entire and easy portable PCB without any wire while featuring low-power electronics.

4.2 Quasi Digital Potentiostat

The focus of this section is the design, development, and validation of a Commercial-Off-the-Shelf (COTS) component-based potentiostat, whose size may fit in

a pen-shaped portable device. This potentiostat needs to be low-cost, low-power, and with good resolution. The primary design novelty of the proposed architecture is the amperometric sensing through bio-inspired event-based techniques [104], which is innovative with respect to the standard approach involving power-hungry Digital to Analog Converter (DAC) and Analog to Digital Converter (ADC) in the architecture [197, 198]. Indeed, the whole proposed potentiostat is a QD electronic interface, which takes advantage of an event-based technology [104].

In the QD domain, the information is encoded in the temporal distance between consecutive pulses of a digital signal, including both the properties of a digital and an analog signal [199], to maximize the quality-energy trade-off [200]. This event-based design avoids power-hungry DAC and ADC [197], with a compact and low-power read-out circuit (even when a numerical output is needed [201]). Meanwhile, the event-based approach yields accuracy increase and noise reduction [202], and it provides advantages in terms of signal processing in the time domain [203]; furthermore, the same approach can be seamlessly applied to the (wireless) information transmission as well [204, 205]. The literature presents numerous examples of applications based on bio-inspired and QD approaches [206, 207, 199]. However, to the best of our knowledge, they have never been integrated for the scope of providing on-line monitoring of anaesthesia. The proposed architecture is validated by comparing the measurement results with the ones achieved by a commercial laboratory potentiostat. Acetaminophen (APAP) is the benchmark drug since it is usually administered in anaesthesiology [208]. This section is adapted with permission from [102].

4.2.1 Design and Circuit Implementation

The proposed custom QD potentiostat relies on QD to analog conversion and vice-versa. Figure 4.1 shows the proposed design, which contains a voltage driver (PWMtoV) and a current read-out (ItoQDE). The Voltage Follower (VF) avoids current flow on the Reference Electrode (RE). The grounded Working Electrode (WE) is the selected topology for the potentiostat architecture since it minimises the number of components required [133]. The WE is connected to half-supply ($½\,V_{DD}$) to achieve both dual-voltage driving and dual-current sensing (i.e., driving and measuring both positive and negative voltages/currents) without the introduction in the system of a dual-voltage supply.

The driving of the electrochemical cell can be exploited, creating a voltage ramp. In the actual design, the technique involved is the Variable Duty-Cycle Method (VDCM) [133]. The method permits controlling the electrochemical cell driving voltage using the Pulse Width Modulation (PWM), a type of QD signal. Namely, the digital logic contained in the core can drive a constant or a slowly-changing voltage, varying the Duty Cycle (DC) of a square wave. The implementation of the PWMtoV converter is then based simply on the use of a low-pass filter, which

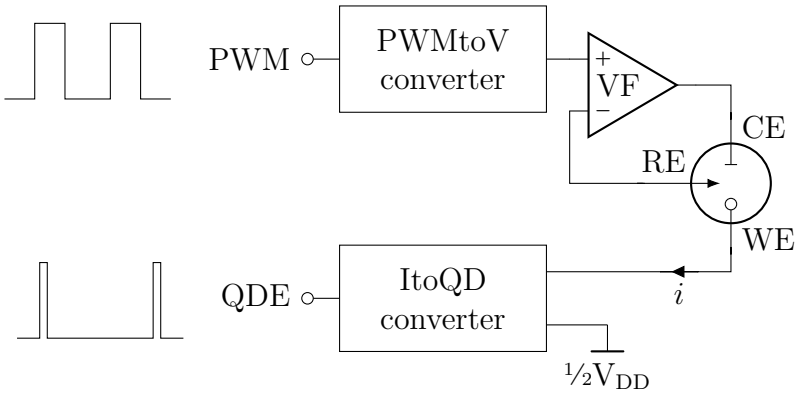

Figure 4.1: Complete topology of the proposed QD potentiosta: the PWMtoV converts the input PWM signal in the driving voltage, while the current read-out (ItoQDE) translates the value of the target redox current into QDE. Both element are event-based. Reprinted with permission from [102]. © 2019 IEEE.

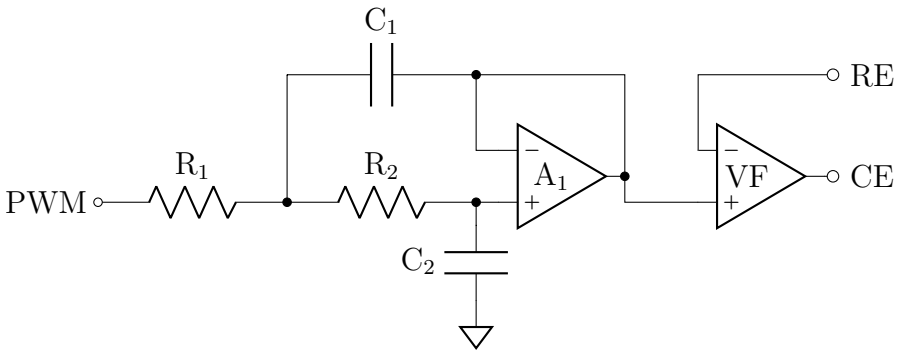

Figure 4.2: PWM to voltage converter schematic: the first operational amplifier (A_1) is an active second-order Sallen-Key low-pass filter, generating a voltage (V, on right) linearly dependent to the duty cycle of the input PWM signal (on left).

filters the square wave signal to create a constant analog voltage. This block is a second-order active low-pass filter in the Sallen-Key configuration at the cut-off frequency of 33 Hz and quality factor around 0.8 (Figure 4.2). The driving potential applied between the Counter Electrode (CE) and the WE is directly proportional to the DC of the PWM input signal. At convenience, the circuit can provide an electrochemical cell with an increasing or decreasing voltage ramp, just modulating the DC of the input. The pole is inserted at a frequency much lower than the PWM signal modulating frequency in order to provide good quality in the conversion. The voltage at the output of the low-pass filter is in the range from zero and V_{DD}, proportional to the value of the duty cycle of the PWM square wave. The output voltage can be expressed as in Equation 4.1, where DC is the duty cycle and V the driving voltage.

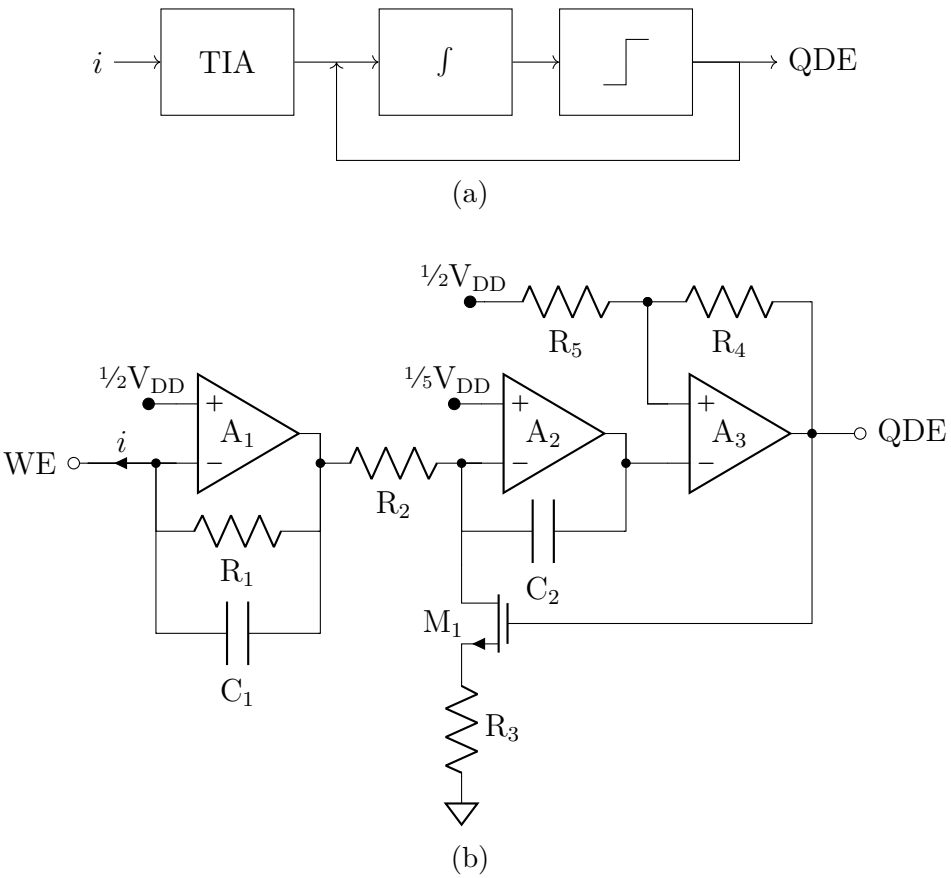

Figure 4.3: Current to QD stream of event converter (ItoQDE): block diagram (a) and full schematic (b). The redox current (i, right) is converted to QDE signal (left). Adapted with permission from [102]. © 2019 IEEE.

$$V = DC \cdot \mathrm{V_{DD}} \tag{4.1}$$

The oxidation or reduction current (i) is read, converting it to a QD stream of Event (QDE) by the ItoQDE block. Differently from what the literature proposed in [206, 209, 210], a low-complexity one-input one-output read-out circuit able to convert the dual-range current in an event stream, with a single-voltage supply is shown here. The implemented conversion relies on the concept of QD signal: the information is carried in the temporal distance between two edges of a digital, event-stream signal. The signal is a Pulse Position Modulation (PPM). Figure. 4.3a shows the block diagram of the current to QD converter, while Figure 4.3b presents the proposed schematic. The ItoQDE module contains three amplifier blocks: a Trans-Impedance Amplifier (TIA) (A_1 and R_1), an integrator (A_2, R_2, and C_1) and a comparator (A_3, R_4, and R_5). The TIA converts the input current into voltage

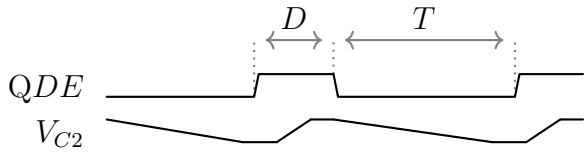

Figure 4.4: ItoQD converter timing diagram. The timing (T) between consecutive edges of the QDE signal is proportional to the monitored current. Adapted with permission from [102]. © 2019 IEEE.

as follow:

$$V_{A1out} = -\mathrm{R}_1 \cdot i + {}^1\!/\!_2\mathrm{V}_{\mathrm{DD}} \tag{4.2}$$

A_2 integrates the voltage coming from the trans-impedance amplifier. A square wave signal is generated through the comparator. The distance between two rising edges of the QDE signal is proportional to the voltage on the output of the trans-impedance amplifier and proportional to the input current.

Figure 4.4 presents the timing diagram of the current to frequency conversion. The capacitor C_1 is discharged according to the input current (adapted to the dynamic by the trans-impedance amplifier), the comparator notifies when V_{C1} overcomes the lower threshold; this sets QDE. After that, a reference current rapidly charges the capacitor again through the feedback MOSFET (M_1 and R_3), the signal QDE is reset, and the conversion can start again. According to Equation 4.4, the sampled current i is proportional to the timing between two consecutive edges, where i_0 is the offset current and V_{th} is the comparator threshold. Equation 4.3 presents the conversion between the voltage V_{A1out} and the period of the QD signal.

$$T = \frac{\mathrm{R}_2 \cdot \mathrm{C}_1 \cdot {}^1\!/\!_2\mathrm{V}_{\mathrm{DD}}}{V_{A1out} - {}^1\!/\!_5\mathrm{V}_{\mathrm{DD}}} \quad \text{when} \quad V_{A1out} \in [{}^1\!/\!_5\mathrm{V}_{\mathrm{DD}}, \mathrm{V}_{\mathrm{DD}}] \tag{4.3}$$

where T is the distance between two edges of the signal QDE, and it can be evaluated in a digital logic architecture thanks to the use of a free-running counter. The relation between current and the period of the QD signal can be described with Equation 4.4.

$$i = -\frac{\mathrm{R}_2 \cdot \mathrm{C}_1 \cdot \mathrm{V}_{\mathrm{th}}}{\mathrm{R}_1 \cdot T} + i_0 \tag{4.4}$$

where i_0 is the steady offset current and can be measured directly from the system in open-circuit to compensate variations. The minimum time spent in the high state by the signal QDE D_{min} must be in order to be lower than T while guarantying glitch-free electronics (Equation 4.5).

$$D_{min} = 2 \cdot \mathrm{R}_3 \cdot \mathrm{C}_1 \tag{4.5}$$

Figure 4.5: PCB implementation of QD potentiostat with COTS components; the electrochemical cell connected on pin on the left, and power supply, PWM, and QDE on the right. Adapted with permission from [102]. © 2019 IEEE

The current is linearly proportional to the frequency of the output signal, which is one over the period of the signal QD (T). The frequency spans in the range related to the minimum and the maximum measurable current as described by Equation 4.6.

$$\Delta f = \left[0\,;\ \frac{1.5}{\mathrm{R_2}\cdot\mathrm{C_2}}\right] \tag{4.6}$$

The central output frequency (f_0), namely the value acquired when the input current is zero, is:

$$f_0 = \frac{1}{2\cdot\mathrm{R_2}\cdot\mathrm{C_2}} \tag{4.7}$$

The proposed potentiostat is implemented on a single PCB using COTS components as showed in Figure 4.5. The Figure 4.6 presents the input-output characteristic of the QD potentiostat reader. The output event frequency (event rate) is linearly proportional to the input current. In the implemented potentiostat, the PCB size is 78 mm×10 mm. Tuning the component according to Equation 4.4, the driving voltage range is set to be between −1.2 V and 1.2 V, while the input current range between −60 µA and 60 µA. The system is designed to fit an input PWM signal at the frequency of 20 kHz. In the current range, the event rate (i.e., frequency of the events) of the output QDE signal spans across 0.38 kevent/s and 34 kevent/s, with a resting event rate of 17 kevent/s. The PCB includes all the components required to stabilize the power supply and furnish all the reference voltages. This is achieved by a low drop-out power manager and one different voltage follower and resistor network for each voltage reference ($^1/_2\mathrm{V_{DD}}$ and $^1/_5\mathrm{V_{DD}}$). Capacitors are also added to avoid any floating of the reference voltages due to current drops. A closed feedback loop experiment is performed to verify the system by inserting a resistor between shortened CE-RE and WE nodes. The experiments highlighted that both PWM to voltage and current to QDE conversions are linear with a maximum linearity error of 0.14 %. The WE input is left unconnected, and the current is sampled at the operating frequency of the Cyclic Voltammetry (CV), namely 60 Hz to quantify the noise level. The level of noise is 39 nA considering the standard deviation of the sample. In the full scale (±60 µA), the equivalent number of bits is 11.6 bit, closer to the resolution of DAC, usually implemented

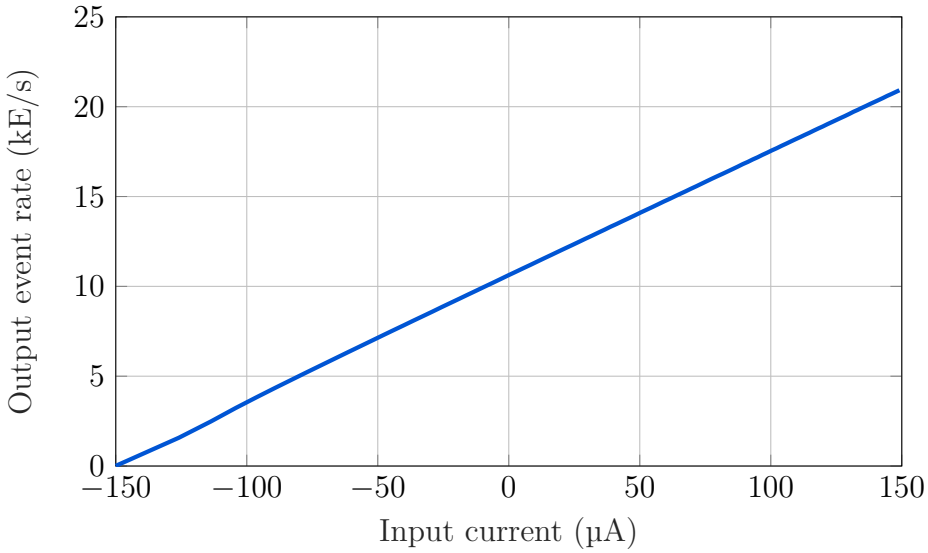

Figure 4.6: QD potentiostat characteristic: simulation results (LTSpice®), on proposed solution, considering an input raging in –150 µA and 150 µA. The output event rate (y axis), varies almost linearly according the value of the input current (x axis).

in a custom-built potentiostat for bio-sensing application (12 bit [115]). The mean total power consumption of the board is 19.5 mW as measured during lab testing.

4.2.2 Validation and Performance

As visible in Figure 4.7, a full demo setup is carried on to validate the QD potentiostat. The potentiostat described in Section 4.2.1 is interfaced to the electrochemical sensor for the detection of APAP. Namely, the commercial Screen Printed Electrode (SPE) acting as a biosensor is immersed in 10 ml becher containing Phosphate Buffer Saline (PBS) and a known concentration of APAP. The PBC implementing the QD potentiostat is inserted into a custom-built 3D case. A custom digital interface deployed on a Field Programmable Gate Array (FPGA) board transmits the data to a laptop via UART communication. The laptop displays the results in real-time of the APAP detection through a Matlab® Graphical User Interface (GUI), highlighting the oxidation current peak and providing to the visitor step by step the concentration monitored by the proposed system. The video of this validation test is available at [211].

The measures are performed on subsequent increasing concentrations of APAP in the therapeutic range (between 50 µM and 300 µM) accordingly to what detailed in Section 2.2.1 to perform the tests. Two different electrochemical sensing methods are taken into account: CV and Differential Pulse Voltammetry (DPV). The CV

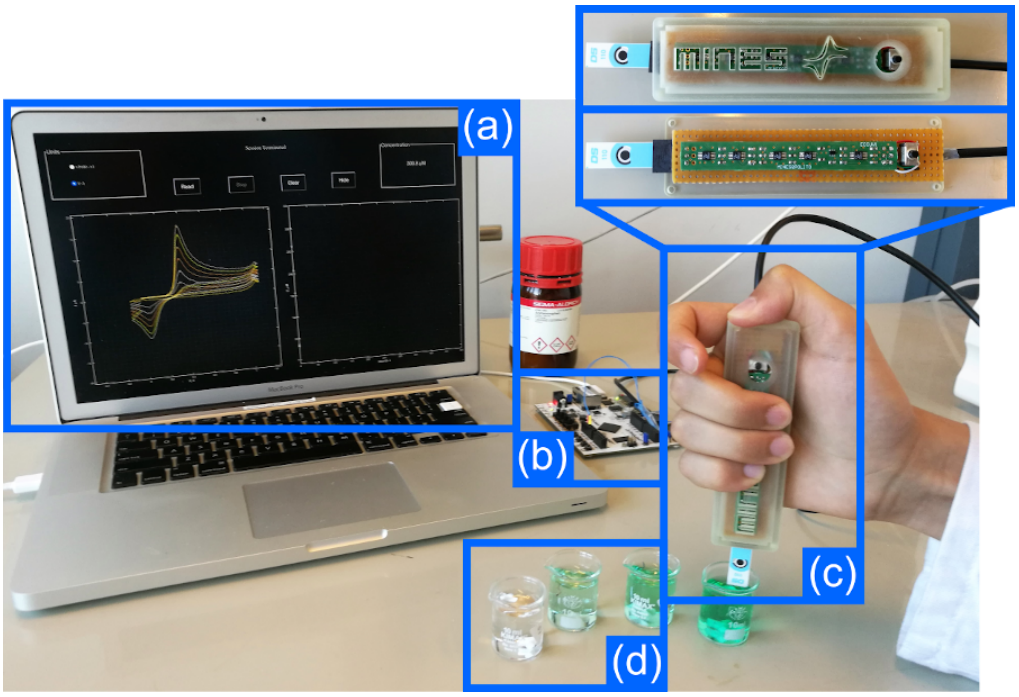

Figure 4.7: Validation setup for the QD potentiostat: GUI display interface (a), FPGA control logic (b), proposed portable pen (c), APAP samples (d). Reprinted with permission from [103]. © 2019 IEEE.

is performed with a Scan Rate (SR) of 0.2 V / s, in the range between −0.1 V and 1.1 V, with a voltage step of 6 mV, and a time step of 30 ms. The DPV is performed at 0.1 V / s, in the range between 0 V and 1 V, with a voltage step of 6 mV, a time step of 60 ms, the modulation amplitude is set to 60 mV, and the modulation time to 30 ms. A difference in SR between the two methods is introduced in order to compensate for the higher sensitivity of the DPV method [133].

The custom digital interface is deployed on the FPGA board Xilinx® Artix-7™, which generates the PWM signal to drive the cell with the waveform required by the voltammetry technique. The timing of the event received on the QDE line is measured with a simple free-running counter; the current is constantly sampled every voltage step. The data collected are sent out through a UART-USB port and then stored. The sensing of APAP is also repeated using a lab instrument, i.e., the Metrohm Autolab PGSTAT 302N driven by the software Nova 1.11 to validate the novel QD potentiostat. The data received from the lab instrument and the developed system are processed in Matlab® (v. R2017b), without any further post-processing or filter. The peaks are detected with the findpeaks built-in function after a blank-baseline rigid translation. The function returns prominence of the current peak; this value is considered for the final estimation of the drug concentration.

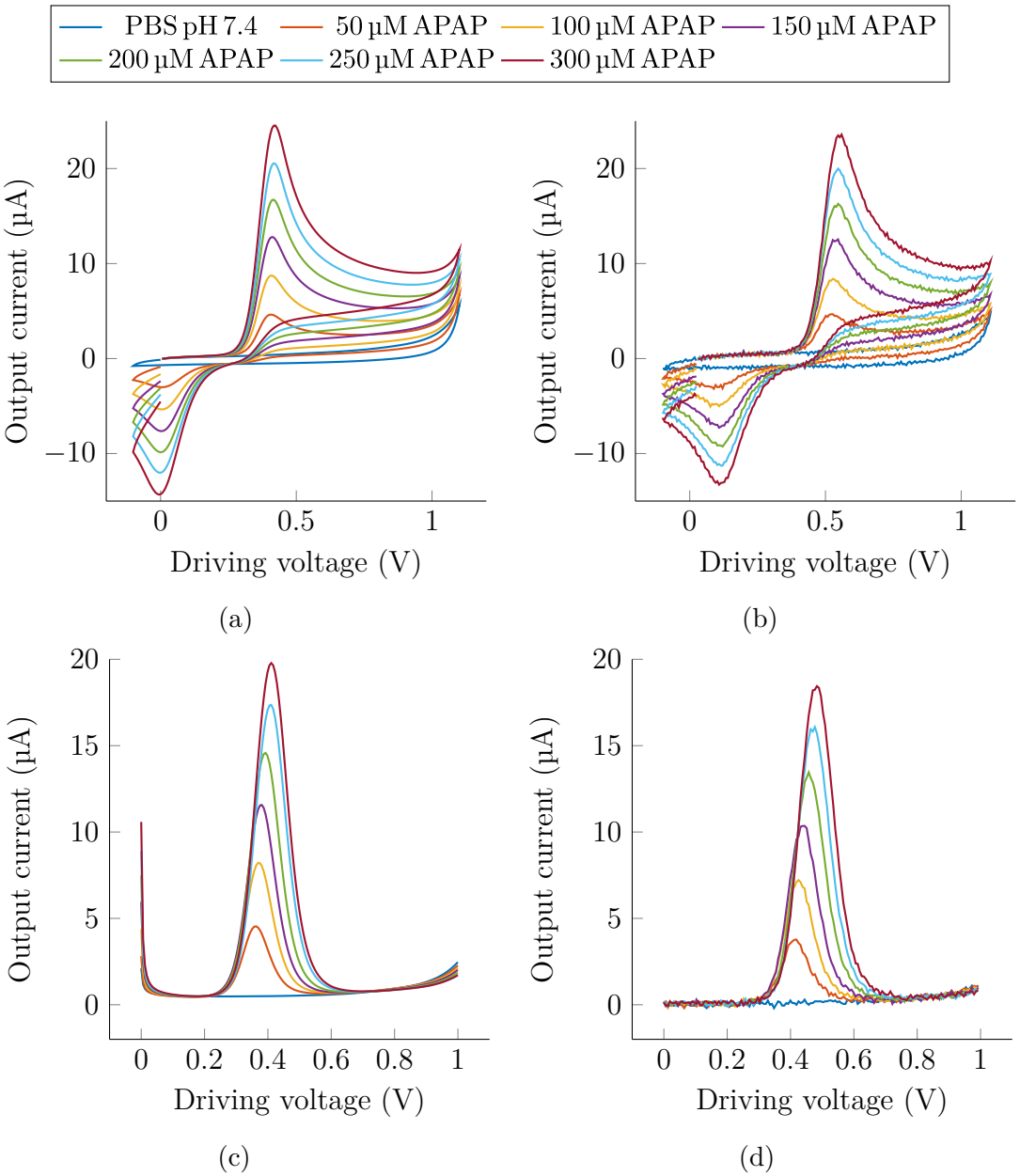

Figure 4.8: Output voltammograms obtained by lab instrument (left) and by QD potentiostat (right), considering CV (top) and DPV (bottom). Namely, lab instrument CV (a), QD potentiostat CV (b), lab instrument DPV (c), QD potentiostat DPV (d). Reprinted with permission from [102]. © 2019 IEEE.

Figure 4.8 displays a comparison in the output acquired by the two devices (QD potentiostat and lab instrument) considering CV (4.8a, 4.8b) and DPV (4.8c, 4.8d).

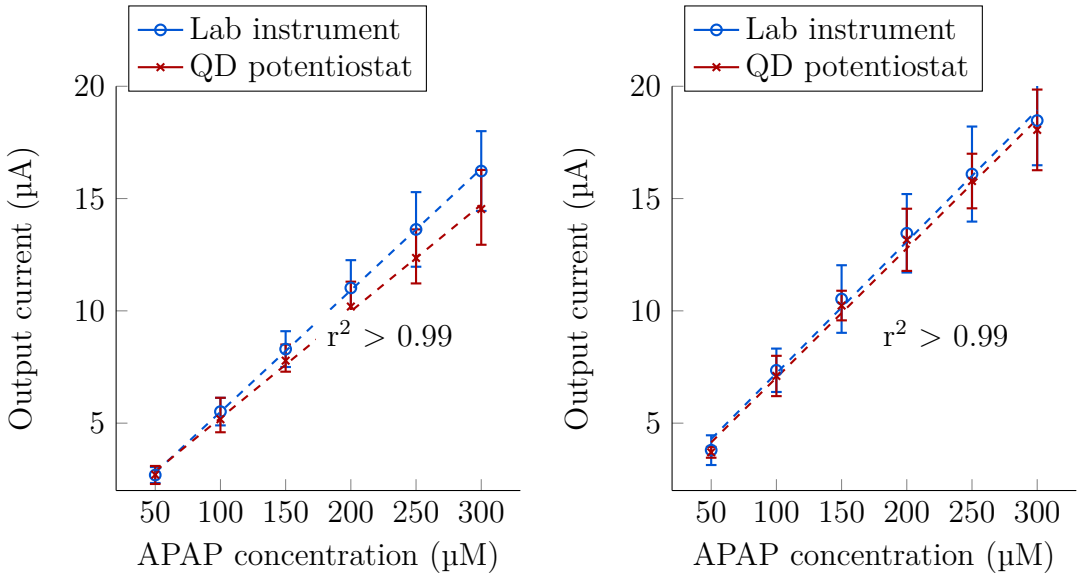

Figure 4.9: Calibration curves comparison between lab instrument and QD potentiostat, for CV (a) and DPV (b), in both cases the graphs almost overlaps. Reprinted with permission from [102]. © 2019 IEEE.

Table 4.1: Results comparison between lab instrument and QD potentiostat, considering CV and DPV in terms of sensitivity and LOD. The sensitivity shows small differences among methods and systems. Otherwise, the LOD increases with QD potentiostat but always remaining one-tenth of the therapeutic range. Reprinted with permission from [102]. © 2019 IEEE.

	CV		DPV	
	Lab instrument	QD potentiostat	Lab instrument	QD potentiostat
Sensitivity (nA / µM)	54.1 ± 7.1	47.5 ± 5.0	58.6 ± 5.9	57.6 ± 5.6
LOD (µM)	1.43 ± 0.18	5.43 ± 0.57	0.57 ± 0.06	5.08 ± 0.49

DPV is discussed for the sake of completeness, although the smart pen will employ CV only. The proposed solution introduces a certain level of white noise (4.8b, 4.8d), despite this, in both methods the results are comparable. Figure 4.9 reports the calibration curves obtained by the analysis of the data. The implemented system does not introduce a visible reduction in sensitivity; the two fitting curves almost overlap with the DPV method while they are very close in CV. The evaluated regression coefficient (r^2, higher than 0.99) does not change; hence, the

system does not introduce non-linearities. Table 4.1 presents a comparison between the two architectures. The sensitivity is similar (–12% with respect to the lab instrument in CV), with a standard deviation reduced of 20% in the presented solution with respect to the lab instrument in DPV. Even if the Limit of Detection (LOD) has a higher value in QD potentiostat, due to lower noise rejection, the value remains one order of magnitude lower than the minimum therapeutic concentration of the APAP, hence, confirming its excellent performance. These findings are highly promising, considering the reduction of three orders of magnitude of hardware cost, the minimal size (two orders of magnitude smaller), allowing much-improved portability between QD potentiostat with respect to the commercial instrumentation. The results prove that the presented approach does not require the introduction of post-processing, analog/digital filter, and differential measurement in QD potentiostat, methods all adopted by the lab instrument, to get comparable performance.

4.3 Embedded Device

The core of the portable smart pen is a custom-built embedded device enclosed in a 3D printed pen-shaped case. The embedded device consists of a single, double-layer PCB of size 92 mm×17 mm. The case is a box-shaped container with rounded corners of size 130 mm×30 mm×30 mm. The PCB is the mechanical support that electrically connects electronic components using conductive paths. For the final medical application, the main required features well match the PCB implementation. The device has to respect some indications. Namely, it has to be small with a proper shape suitable for measuring the blood substance of the patient. For this purpose, the realization of a board long and narrow, suitable sizes as for a medical syringe, is suggested in order to facilitate the application; it has to be portable and, for this purpose, the circuit, the components and, the firmware is selected in order to reduce the power consumption.

4.3.1 PCB Implementation

The PCB (Figure 4.10) includes a Bluetooth® antenna for wireless communication, a MicroController Unit (MCU) for smart detection, the previously mentioned QD potentiostat (driver and reader), and a power manager. The PCB is connected to the disposable sensor with a jack connector. The design is carried on with Altium Designer® 18.0, developed by Australian software company Altium Limited. Figure 4.11 shows the 3D view of the implemented PCB, considering the top and bottom view.

The MCU is the Nordic® Semiconductor nRF52840 built around the 32 bit ARM® Cortex™-M4 processor, with a floating-point unit at 64 MHz. It features a

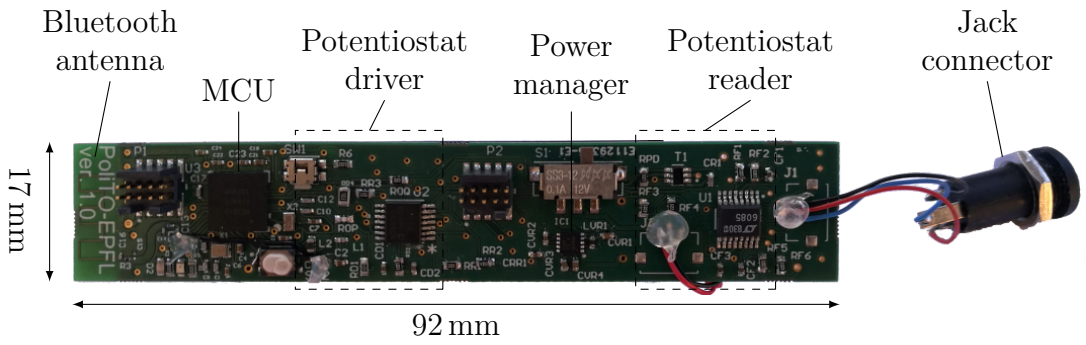

Figure 4.10: The embedded board includes on a single PCB a Bluetooth® antenna for communication, a MCU for processing, the QD potentiostat (driver and reader), a power manager, and the jack connector to host the sensor. Reprinted with permission from [105]. © 2021 IEEE.

Bluetooth Low Energy transceiver, four PWM channels, three Real-Time Counter (RTC), and up to 32 General Purpose I/O (GPIO) pins with configurable output drive strength [212]. This component provides sufficient processing power to guarantee future developments in a fully embedded framework, and it already showed excellent capability in biomedical applications [213].

The QD potentiostat is implemented on top of the PCB with COTS components to reduce cost and increase flexibility. The potentiostat is interfaced on one side to the WE, CE, and RE of the electrochemical needle-shaped sensor (see Section 2.3) through the female stereo audio jack connector. On the other side, PWM and QD signals are connected to two MCU GPIO ports. For space reasons, the eight op-amps needed to implement the driver and reader circuit are integrated into just two components. Driver and reader of QD potentiostat are implemented with Surface Mount Technology (SMD) resistor and capacitor. With three integrated circuits, the LTC® 6085 and the Analog Devices AD863, both including four op-amps, and the Nexperia 2N7002BKS, including two n-MOSFET transistors. The difference between the two op-amp lies in performance and power consumption. The AD863 is chosen for its speed performance; indeed, that part of the circuit is addressed to the PWM conversion in linear-sweep voltage for the sensor and the comparison task to obtain the QD signal as output. On the other hand, all the stages that do not need high performance are realized with LTC6085 to preserve power. Both amplifiers are rail-to-rail devices to offer a wide dynamic and good linearity.

The system features Bluetooth® 5, IEEE 802.15.4-2006, 2.4 GHz transceiver to allow Bluetooth® Low Energy (BLE) communication. The Bluetooth® antenna is integrated on the PCB top layer as a copper trace antenna (Figure 4.12). The geometrical design is a replica of the one proposes by the Nordic and developed on the dongle device nRF52840 [212]. Together with the antenna copper trace, it is fundamental to a matching circuit. In the project, the π network matching is

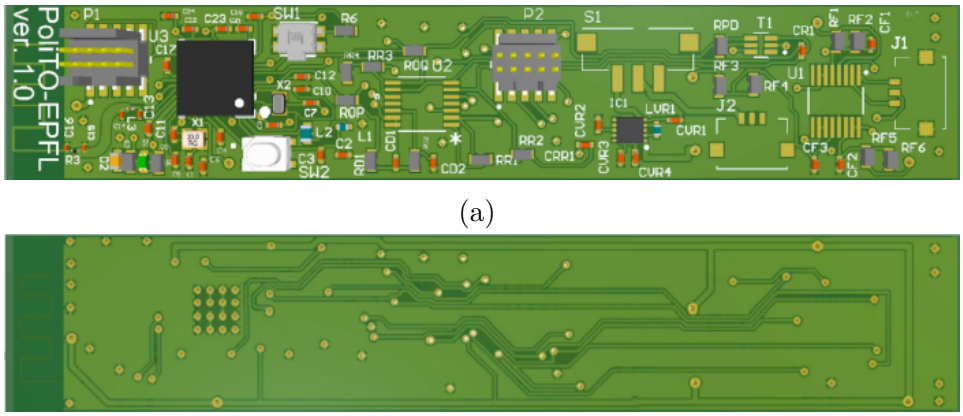

(a)

(b)

Figure 4.11: 3D view of the implemented PCB: top (a) and bottom (b) view. Reprinted with permission from [214]. CC BY 3.0 IT.

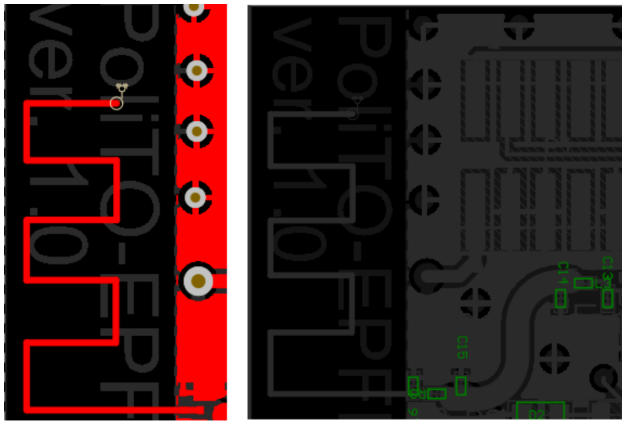

Figure 4.12: Bluetooth® Antenna layout on PCB. Left: antenna geometry trace; Right: Antenna with matching network. Reprinted with permission from [214]. CC BY 3.0 IT.

realized by an inductor connected on two capacitors.

A lithium-thionyl chloride AA 3.6 V battery with a capacity of 2700 mAh, placed conveniently on the backside of the PCB, powers the device. A buck-boost DC-DC voltage regulator, Texas Instrument™ TPS63031, fixes the output voltage at 3.3 V [214].

4.3.2 Firmware Implementation

The MCU hosts a firmware for the automatic measurement of propofol. The firmware is developed in SEGGER Embedded Studio for ARM®, a streamlined, integrated development environment, compilation tools, and libraries for building,

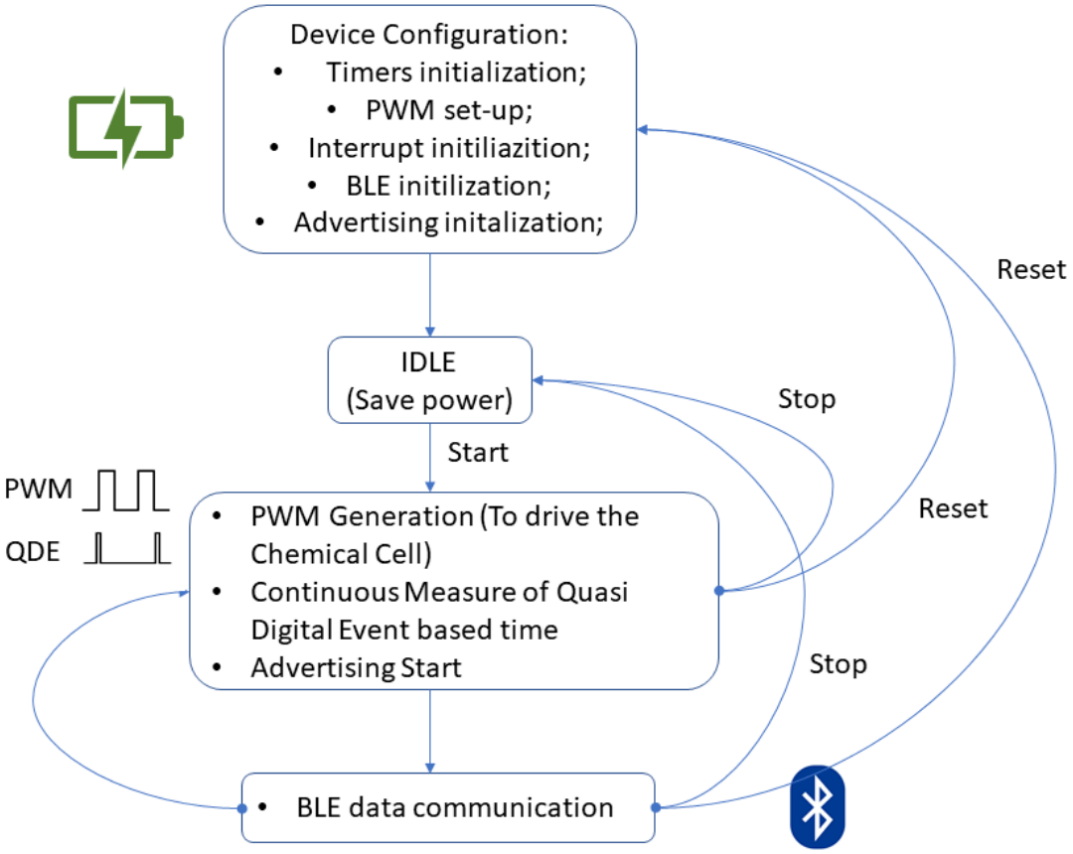

Figure 4.13: Flow chart of the firmware routine: after the configuration, the device resides in idle-state; pressing the start button the device moves to the on-state, perform the measurements, and send out via Bluetooth® the data. Reprinted with permission from [214]. CC BY 3.0 IT.

testing, and deploying applications on ARM® and Cortex microcontrollers [215].

Figure 4.13 represents the flow chart of the state covered by the processor during the operation. A mechanical switch controls the power-on of the board. At the power-on, some configurations and setup operations are executed to make the system ready to use. The configurations include the initialization of PWM and timer drivers, the definitions of interrupts, and the BLE setup. After all the preliminary steps have terminated, the micro-controller waits for the start command in the idle state. Only the interrupt connected to the GPIO linked to the mechanical button can wake up the system. The battery charge is preserved in this condition.

The idle-state is called every time the user decides, always employing the pressure of the button to pause the operation and lie in stand-by. When the start is asserted, the firmware proceeds with the main loop. The operation is repeated in an infinite loop: the electrode cell is driven cyclically by the PWM signal. The current response in terms of event quasi-digital signal is continuous monitoring and

measurement. During the main state, the device is discoverable and connectable by the central BLE receiver. Once the set of measures is ready, they are transmitted through the BLE technology and protocol; this step concludes the loop cycle. The only way to pause or stop the operations is to push again the same button (in this case, it stands for stop command) or reset the device.

Once all the preliminary steps have been executed, the MCU also starts BLE advertisement, and then the connection is established. The device acts as a Generic Attribute Profile (GATT) BLE server, containing a set of GATT characteristics. The custom service is accessible by an external GATT client, calling and reading the measurement GATT characteristic. The MCU drives the electrochemical cell with the CV pre-defined stimuli, modulating the PWM signal, and samples back the Faradaic current through the QD signal. The sampling of QD is done by a simple counter which measures the timing distance between consecutive pulses of QD. The measurement is read directly by the client on the attribute "current" of the GATT characteristic.

4.3.3 Case Design

A custom 3D printed case host the PCB and all the component of the smart electronic pen for continuous monitoring of anaesthetics. The case is a box-shaped container with rounded corners of size 130 mm×30 mm×30 mm and a thickness of 2.5 mm, composed of two shells. The case is designed with FreeCAD 0.18. The case is printed with a Formlab Form 3 printer using clear wax.

Figure 4.14 shows the entire case inside the assembled embedded device and the open compartment for battery replacement. The top shell (Figure 4.15a) contains the custom PCB and the female audio jack connector for the needle-shaped sensor. Meanwhile, the bottom shell (Figure 4.15b) closes the case. The case presents numerous loopholes to ensure enough ventilation and avoid any possible heating when the user holds it in his hand. On the top shell, the loophole takes the form of the word MINES to acknowledge the Micro and Nano Electronic Systems (MiNES) research group author of this thesis [216].

4.4 Complete System

The proposed complete system for anaesthetics monitoring is shown in Figure 4.16. The needle-shaped electrochemical sensor, designed specifically for direct detection of propofol, is interfaced to the patient's body under anaesthesia (on the right). The sensor connects to the smart portable pen (in the middle). The pen consists of a battery-operated embedded device packaged in a handy pen-shaped case. The device includes a QD potentiostat as sensor front-end and communicates via Bluetooth®. On a computer (on the left), Machine Learning (ML)-based

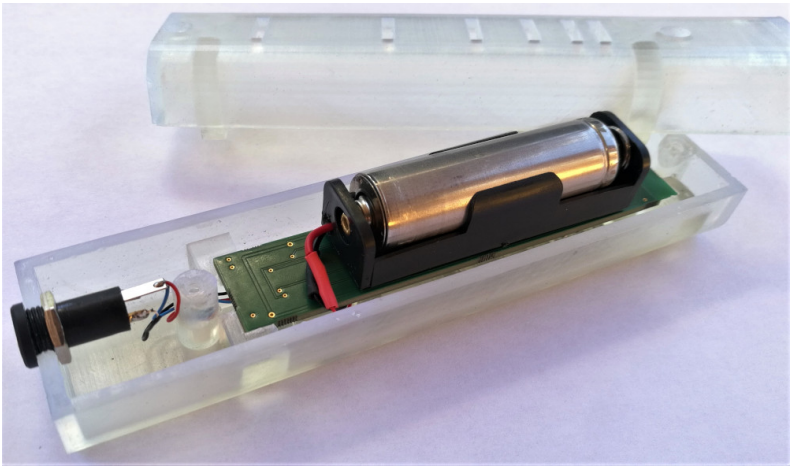

Figure 4.14: Case of the smart electronic pen and open compartment for battery replacement. The PCB is upside down.

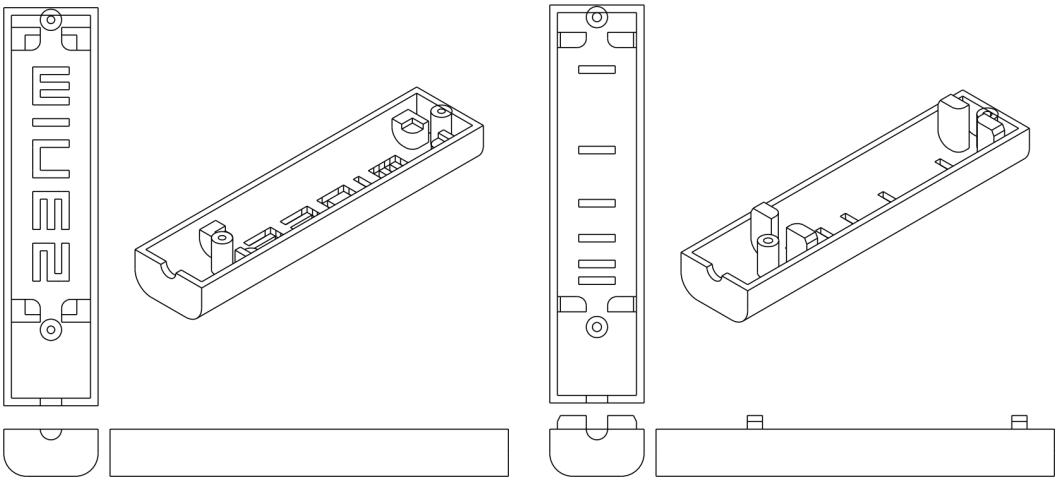

(a) (b)

Figure 4.15: Isometric projection of the designed case for hosting the smart electronic pen: top shell (a) and bottom shell (b).

model classifies the concentration of anaesthetics. It informs the anaesthesiologist continuously on the concentration of propofol present in the body of the patient.

4.4.1 The Implementation

The proposed sensor is the low-cost three-electrode electrochemical cell in a needle shape to target detection of propofol in human serum [98]. The sensor is detailed in Section 2.3 is composed of Pencil Graphite Electrode (PGE), which reduces the propofol fouling of the surface [129]. The sensor features a male audio

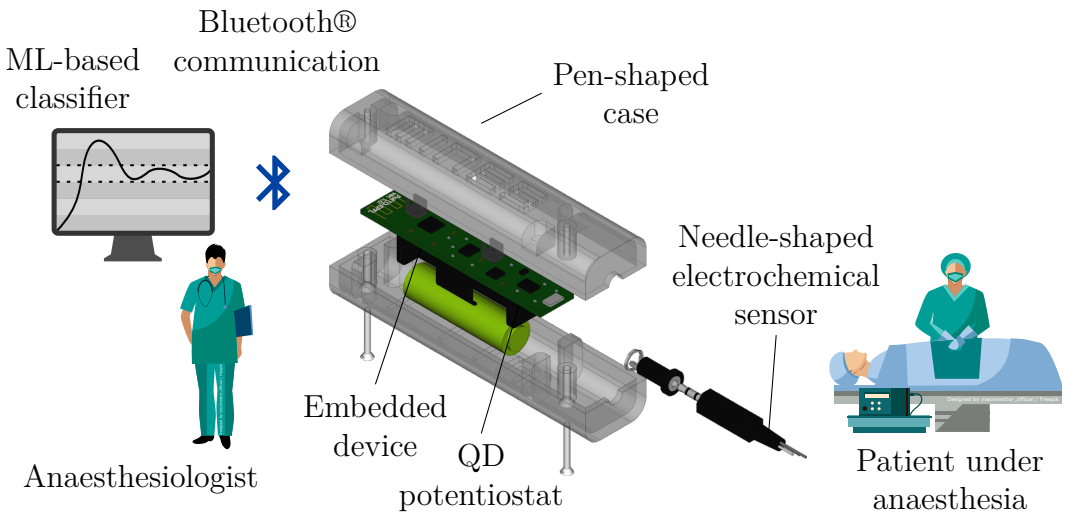

Figure 4.16: The anesthesiologist follows up the infusion of anaesthetics in the patient body through the portable pen. The system includes a needle-shaped electrochemical sensor for propofol detection, a QD potentiostat on an embedded device, closed in a custom pen-shaped case, with Bluetooth® communication towards an external PC running an ML-based classifier. Reprinted with permission from [105]. © 2021 IEEE.

jack 3.5 mm stereo connector, which provides a low-cost, disposable, and robust electrical standard. The proposed potentiostat is based on the design presented in [102]. The circuit relies on analog to QD conversion and vice-versa, as detailed in Section 4.2. The core of the portable smart pen is a custom-built embedded device enclosed in a 3D printed pen-shaped case as detailed in Section 4.3. The embedded device consists of a single, double-layer PCB featuring an MCU hosting the firmware for the automatic measurement of propofol. The custom service is accessible by an external GATT client,

An external computer, running custom software and connected to a monitor, processes the measurement to provide smart and easy-to-read information to the anesthesiologist. This software contains a GUI and an SVM classifier, taking advantage of [103, 101]. The ML-assisted method is required for compensating nonlinearities introduced by the fouling effect of propofol on the electrochemical sensor as detailed in Section 3.4. Moreover, the classifier is the most efficient tool to directly provide the final user (the anaesthesiologist) with the preliminary information necessary to keep the constant dose in the range of interest. The computer resides the external GATT client, which reads via BLE the full vector of measurement samples. This data is stored and processed by the software to obtain a four-features list sent to the ML-based model. Three relevant features are extracted from the received CV: the peak current, the peak position, and the total

charge. At the same time, the fourth feature is the ordinal number of measurements performed with the same sensor. A digital low-pass filter at the cut-off frequency of 2 Hz removes external electrical noise. The Faradaic current peak is detected after baseline subtraction. The peak is determined by two features: the potential (position of the peak) and the current (height of the peak). These two features are the most relevant for characterizing the electrochemical reaction [133]. Moreover, the total charge exchanged in the Faradaic process is extracted from the CV using the recently proposed TCDC method (Section 3.3). The SVM predicts the class of propofol concentration according to the similarity or distance of the unknown samples to the training instances. Later, a display outputs the results of this classification to the anaesthesiologist.

4.4.2 Final Validation and Performance

All the proposed system components are tested and validated to assess the performance of the complete system. The results cover the most challenging goals achieved by the proposed smart pen to monitor anaesthetics; i.e., reproducibility, portability, and smartness. The needle-shaped sensor is tested and characterized for propofol monitoring in human serum; finally, the QD potentiostat is validated in comparison with respect to a commercial lab instrument, then the performance of the embedded device is evaluated in terms of power consumption and portability.

The needle-shaped sensor is tested to detect propofol in undiluted human serum at body temperature (37 °C), between 10 µM and 60 µM, a range that corresponds to the therapeutic range too. The analysis of the samples is performed in CV, at a SR of 0.1 V / s (see Section 2.2.2 for further detail). The sensor's performance is evaluated through a seven-point calibration on three different items of the needle-shaped sensor. Figure 4.17 displays the output voltammogram (current upon voltage) obtained by a CV procedure on the sensor after data filtering and baseline subtraction. The Faradaic redox peak increases linearly with respect to the concentration of propofol present in the sample. The calibration curve (Figure 4.18) displays the performance of the proposed sensor considering repeatability and reproducibility since it is obtained by an inter-electrode analysis. The sensitivity is 12.29 ± 4.43 nA / µM. The linearity (r^2) is higher than 94.9 %. The LOD is 3.80 ± 1.37 µM, below the minimum therapeutic concentration (10 µM). The position of the redox peak is 452 ± 110 mV.

The QD potentiostat is tested to detect propofol with PGE electrodes in PBS 10 mM at pH 7.4. In this case, the CV is performed with an SR of 0.2 V / s, in the range between -0.1 V and 1.1 V, with a potential step of 6 mV, 30 ms long (see Section 2.2.2 for further detail). The QD potentiostat is validated against the lab instrument (Metrohm Autolab PGSTAT 302N). Figure 4.19 displays the results of the comparison. The output voltammogram from the lab instrument (Figure 4.19a)

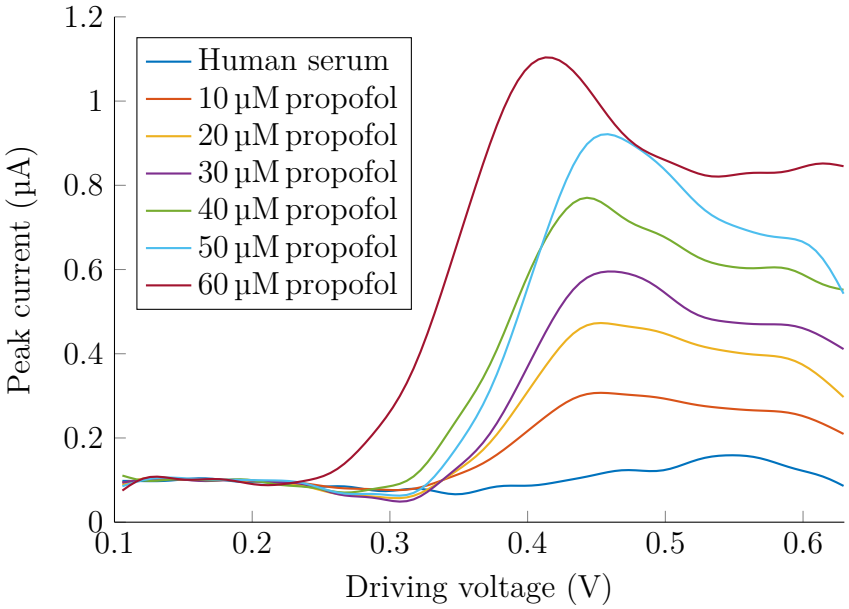

Figure 4.17: Voltammograms acquired by analysis of propofol sample in human serum showing oxidation peaks after signal filtering and baseline subtraction, considering one sensor. Reprinted with permission from [105]. © 2021 IEEE.

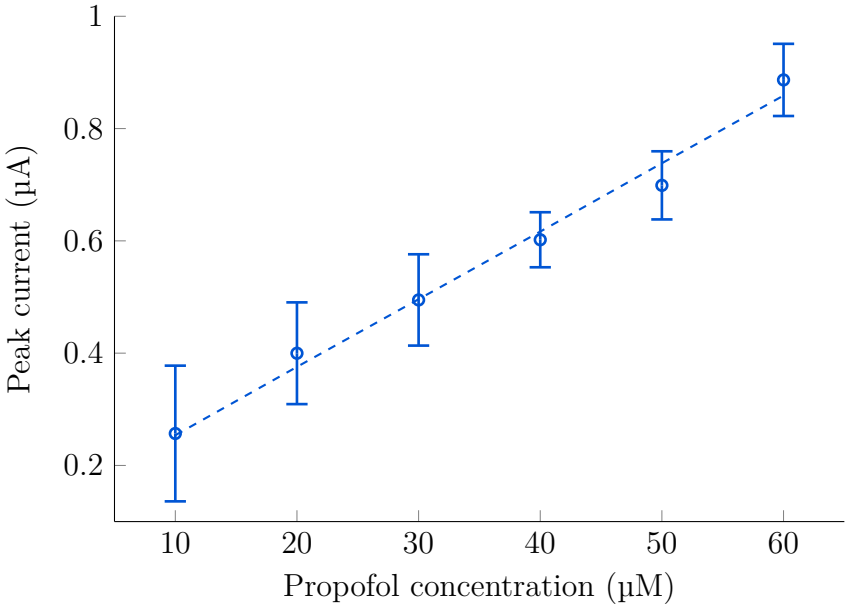

Figure 4.18: Inter-electrodes calibration curve of proposed needle-shaped sensor measuring propofol in human serum. The sensor shows good linearity and low uncertain. Reprinted with permission from [105]. © 2021 IEEE.

Table 4.2: Total power consumption of the embedded device, minimum (Min), average (Avg), and maximum (Max) values, considering both idle-state and on-state. Reprinted with permission from [105]. © 2021 IEEE.

	Min	Avg	Max
Total idle-state current (mA)	8.2	10.1	11.9
Total on-state current (mA)	17.4	20.0	22.0
Total idle-state power (mW)	29.7	36.3	42.9
Total on-state power (mW)	62.7	72.0	79.2

is compared directly to the output voltammogram from the proposed QD potentiostat (Figure 4.19b). No distortions are visible comparing the two curves. At the same time, linear variation and stretch are present on both the x-axis and y-axis: those linear differences are due to the usage of a different electronic system which may introduce offset on both voltages and current. This trade-off was introduced to get less bulky and power-consuming electronics, with few components to allow portability. The real validator is the calibration curves shown in Figure 4.19c to compare the two systems. The linearity (r^2) is higher than 99.9 % in both cases, which demonstrates that the QD potentiostat does not introduce non-linearities or distortion in the measurement. The sensitivity is 565 nA / µM with the lab instrument and 467 nA / µM with the proposed QD potentiostat.

The board's power consumption is measured during lab testing, adding a digital multimeter in series on the power supply of the device. Table 4.2 reports the power consumption of the full embedded device both in idle-state and in on-state. The on-state considers a series of ten full voltammograms, acquired with a pause time of 30 s, without connecting the sensor. The average absorbed current during the on-state is 20 mA, corresponding to the average power consumption of 72 mW. The QD potentiostat consumes 19.5 mW [102]. The digital control and the Bluetooth communication total average power is 52.5 mW.

The system features a 2.7 Ah battery, supporting a battery lifetime of 135 hours always-on, limiting the necessity of charges and allowing continuous usage in more than one surgery per charge. The BLE Received Signal Strength Indication (RSSI) is estimated by the LightBlue® Android™ application to be −95 dBm at 18 m and −51 dBm at 0 m, compliant with the BLE standard specifications.

Considering the comparison with respect to the state-of-the-art and the extent of our knowledge, the literature presents just a few examples of anaesthetics monitoring systems including electronics and full devices with processing and display, such as using Raspberry Pi [156] or an IoT Cloud [3]. Table 4.2 present a full comparison with respect to the state-of-the-art ([146, 196, 115, 156, 129, 3]). The sensor features a LOD higher with respect to the state-of-the-art. However,

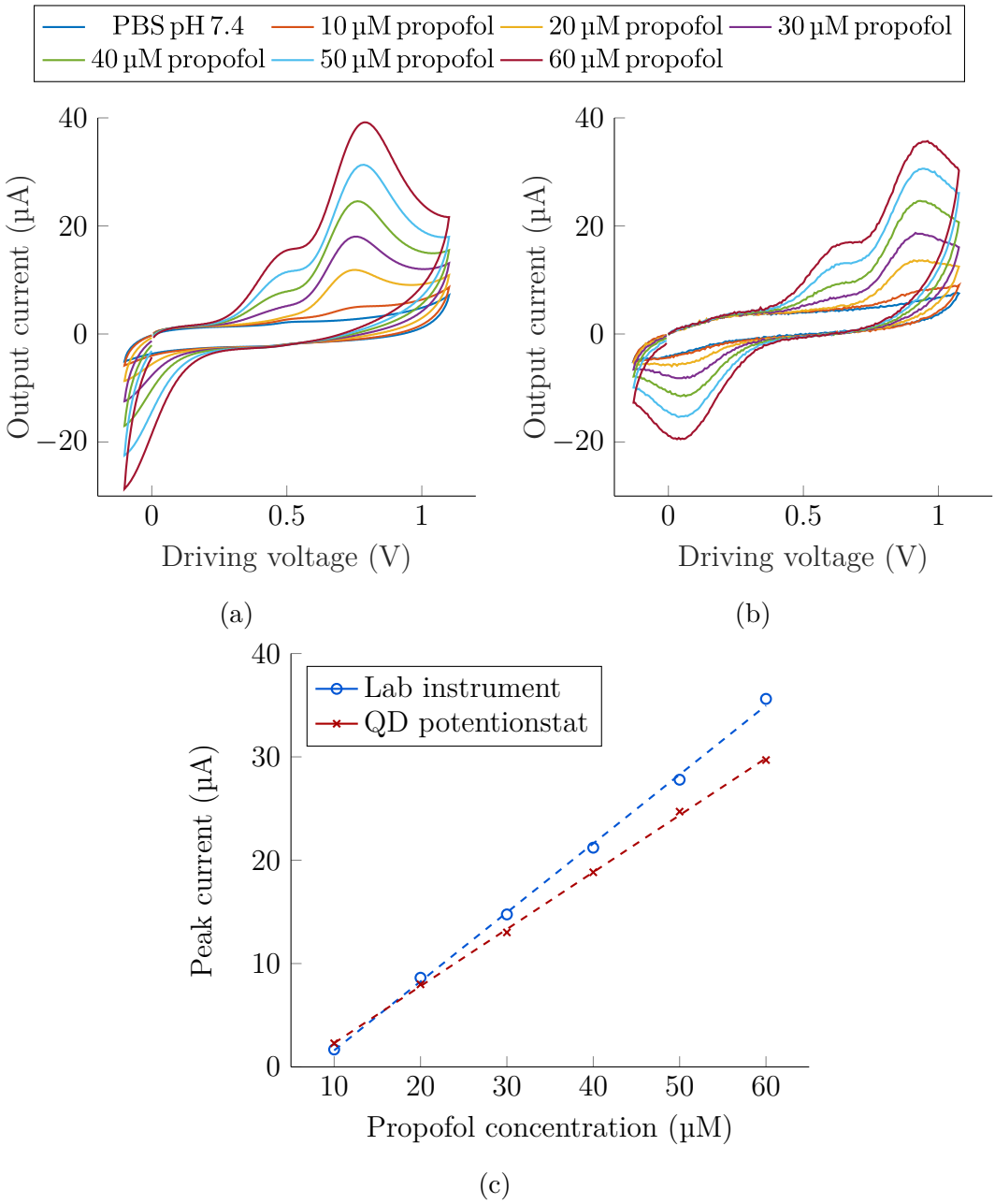

Figure 4.19: Comparison between commercial lab instrument (a) and proposed QD potentiostat (b) in detection of propofol in its therapeutic range. The calibration curves (c) present few differences. Reprinted with permission from [105]. © 2021 IEEE.

it remains below the minimum concentration target of the reference application (10 µM), therefore sufficient for the application. As published in [101], this thesis is

Table 4.3: Comparison with respect to the state-of-the-art. Reprinted with permission from [105]. © 2021 IEEE.

	[146]	[196]	[129]	[115]	[156]	[3]	This thesis
Propofol LOD (µM)	0.5	0.1	0.7	n.a.	n.a.	n.a.	3.8
Number of continuous measure tested	1	12	25	1	n.a.	n.a.	20
Size (cm^2)	n.a	n.a	n.a	96	567	n.a	39
Power consumption (mW)	n.a	n.a	n.a	n.a	n.a	390	72

tested for continuous monitoring up to twenty consecutive measurements with the same sensor, similar to what was achieved by the literature [196, 129]. The proposed QD potentiostat is 59 % smaller (w.r.t. [115]) and consumes way less than one fifth of the total power (w.r.t. [3]). Moreover, to the best of our knowledge, the proposed system is the only one presenting a fully wireless device and including ML-based smart processing. The latter one compensates non-linearities and displays with 100 % classification accuracy the results [101].

4.5 Summary and Main Original Contributions

In this chapter, a novel smart pen for continuous monitoring of propofol anaesthetic drug is presented. The electronic device is the missing piece of technology to close the loop between anaesthesiologist and patient with TDM towards safer anaesthesiology practices.

A newly-designed potentiostat architecture based on the event-based approach, namely QD potentiostat, is used as the main analog front end for the electrochemical sensor. The results prove that the QD potentiostat provides a portable, small, and low power circuit (respectively 92 % and 95 % reduction with respect to previous implementations), always maintaining comparable sensitivity with respect to reference commercial lab instrumentations, and LOD one order of magnitude below the requested minimum therapeutic concentration. The complete system is developed upon a single wireless battery-operated embedded device in a pen-shaped case, 59 % smaller and 81 % less power consuming w.r.t. the state-of-the-art, allowing complete portability and enhancing mobility thanks to the QD approach. The sensor LOD (3.80 ± 1.37 µM) fits the medical application requirements, directly in undiluted human serum at 37 °C, with 100 % accurate ML-based classifier.

Chapter 5

Conclusion and Future Works

General anaesthesia is a medical procedure that requires the infusion of a perfectly balanced cocktail of drugs. The procedure of anaesthesia presents numerous risks and side effects. Today, the anaesthesiology practices leverage on PharmacoKinetics and PharmacoDynamics (PK/PD) models with Target Controlled Infusion (TCI) pumps. The patient is later monitored via BiSpectral (BiS)-index, a weighted sum of ElectroEncephaloGraphic (EEG) features. This approach comes with some limitations since all TCI pumps implement PK/PD models experimentally derived from observation of drug effects on a population of individuals, being so only statistically accurate, meanwhile presenting a significant standard deviation. Several closed-loop devices enter the clinical practice of general anaesthesia, but they are based on ECG or blood pressure sensors, with poor performances due to artefacts. In the meantime, the loop between anaesthesiologist and patient may be closed with the Therapeutic Drug Monitoring (TDM). TDM allows a dynamic adjustment based on the response of the individual. Propofol is the hypnotic agent usually administered to induce and maintain sedation in anaesthesia since it ensures a fast and predictable time of effect. Although numerous sensors have been proposed for detecting and measuring propofol with high sensing performance, they are inefficient in an automatic TDM closed-loop systems since usually based on Dried Blood Spot sampling (DBS). Moreover, long time electrochemical determination of propofol suffers from the so-called fouling phenomenon, limiting stability over time of the sensor. In addition to the sensor, a system allowing the monitoring of anaesthetics must include a potentiostat, i.e., the set of electronic components required to drive and read the electrochemical sensor. Several circuits have been proposed for this purpose, which are usually bulky and power-hungry, limiting their application in the surgery room, and they lack smart data processing and display.

This PhD thesis presents the first-ever realized smart electronic pen for continuous monitoring of anaesthetics, which is the technology required to keep track of the infusion of anaesthetics in real-time and with high accuracy to overcome all the limitations mentioned above. In this thesis, the following goals are achieved:

- **Portability** improves mobility into the surgery room, which is the target environment of use for the proposed system. For this reason, the proposed electronic pen features a wireless-Bluetooth® and battery-operated embedded device in a pen-shape case of size 130 mm×30 mm×30 mm which consumes one-fifth of the power consumption with respect to the state-of-the-art. This is achieved by developing a novel Quasi Digital (QD) potentiostat circuit, which reduced the power consumption of 95% and the size of 92% (w.r.t the state-of-the-art) with the help of an event-based design approach. Moreover, the Sample Rate Optimization (SRO) and Total Charge Detection in Cyclic voltammetry (TCDC) method, first introduced in this thesis, enhanced the system's portability, optimizing the sample rate and reducing to its minimum the data processing respectively.

- **Real-time monitoring** is necessary for continuous TDM. The first needle-shaped sensor for detecting the propofol in situ is here presented for online monitoring of propofol. This sensor features a Limit of Detection (LOD) of $3.80 \pm 1.37\,\mu M$ directly in undiluted human serum at 37 °C, supporting requirements of the medical application. Its audio jack connector makes it directly ready to be connected with the here presented smart electronic pen.

- **Continuous monitoring** is required by the target medical application. The capability of continuous monitoring is achieved in this thesis with the combination of the proposed sensor, novel measurement methods, and a dedicated electronic device. In this thesis, for the first time, a machine learning algorithm helps compensate the propofol fouling, which alters the sensor's sensitivity in time. In particular, the here introduced Propofol Fouling Machine-learning (PFM) method discriminates 10 µM concentration of propofol with 100 % classification accuracy, directly in human serum at body temperature, continuously up to ten minutes.

- **Smart and Automatic** operations reduce the effort of the medical staff in the analysis of the results. In this thesis, SRO, TCDC, and PFM novel methods enhance intelligent and automatic detection of drugs. The PFM classifier, together with the smart electronic pen, makes it possible for the anaesthesiologist to follow up with eyesight the infusion of anaesthetics.

Future works will include the beginning of clinical trials of the proposed technology. This will start with tests of the sensor performance in whole blood. Later, clinical trials will enter the operation theatre monitoring aside the concentration of propofol on patients under general anaesthesia. One major challenge is the study of possible interference not taken into account until now, like uncommon drugs and unique therapeutics. The first step towards the realization and the approval of the technology will also be a detailed analysis related to the biocompatibility of

the system and the sensor. A catheter-like needle may resolve the issue related to the low biocompatibility of the material composing the sensor. Sterilization and similar consideration may be avoided since the interchangeability of the sensor, and its low-cost design will help the direct disposal of the whole sensor after each use. Moreover, the system is suitable for continuous monitoring of anaesthetics in veterinary applications, where few are the information that we have on the physiological response to anaesthetics infusion.

Bibliography

[1] S. Mathur and J. Sutton, "Personalized medicine could transform healthcare," *Biomedical Reports*, vol. 7, no. 1, pp. 3–5, 2017.

[2] W. Sadée and Z. Dai, "Pharmacogenetics/genomics and personalized medicine," *Human Molecular Genetics*, vol. 14, pp. R207–R214, 2005.

[3] F. Stradolini, "IoT bio-electronic multi-panel device for on-line monitoring of anaesthesia delivery," Ph.D. dissertation, 2018.

[4] J.-S. Kang and M.-H. Lee, "Overview of therapeutic drug monitoring," *The Korean Journal of Internal Medicine*, vol. 24, no. 1, p. 1, 2009.

[5] A. Simalatsar, M. Guidi, P. Roduit, and T. Buclin, "Robustness analysis of personalised delivery rate computation for iv administered anesthetic," *Smart Health*, vol. 9, pp. 101–114, 2018.

[6] S. K. Balani, G. T. Miwa, L.-S. Gan, J.-T. Wu, and F. W. Lee, "Strategy of utilizing in vitro and in vivo ADME tools for lead optimization and drug candidate selection," *Current Topics in Medicinal Chemistry*, vol. 5, no. 11, pp. 1033–1038, 2005.

[7] T. N. Tozer and M. Rowland, *Introduction to pharmacokinetics and pharmacodynamics: the quantitative basis of drug therapy.* Lippincott Williams & Wilkins, 2006.

[8] B. Meibohm and H. Derendorf, "Basic concepts of pharmacokinetic/pharmacodynamic (PK/PD) modelling," *International Journal of Clinical Pharmacology and Therapeutics*, vol. 35, no. 10, pp. 401–413, 1997.

[9] M. A. Felmlee, M. E. Morris, and D. E. Mager, "Mechanism-based pharmacodynamic modeling," in *Computational Toxicology.* Springer, 2012, pp. 583–600.

[10] L. B. Sheiner, H. Halkin, C. Peck, B. Rosenberg, and K. L. Melmon, "Improved computer-assisted digoxin therapy: a method using feedback of measured serum digoxin concentrations," *Annals of Internal Medicine*, vol. 82, no. 5, pp. 619–627, 1975.

[11] M. H. Ensom, G. A. Davis, C. D. Cropp, and R. J. Ensom, "Clinical pharmacokinetics in the 21st century," *Clinical Pharmacokinetics*, vol. 34, no. 4, pp. 265–279, 1998.

[12] A. Fuchs, C. Csajka, Y. Thoma, T. Buclin, and N. Widmer, "Benchmarking

therapeutic drug monitoring software: a review of available computer tools," *Clinical Pharmacokinetics*, vol. 52, no. 1, pp. 9–22, 2013.

[13] A. Meneghello, S. Tartaggia, M. D. Alvau, F. Polo, and G. Toffoli, "Biosensing technologies for therapeutic drug monitoring," *Current Medicinal Chemistry*, vol. 25, no. 34, pp. 4354–4377, 2018.

[14] C. J. Landmark, I. Fløgstad, A. Baftiu, M. Syvertsen, U. Enger, J. Koht, and S. I. Johannessen, "Long-term follow-up with therapeutic drug monitoring of antiepileptic drugs in patients with juvenile myoclonic epilepsy," *Epilepsy Research*, vol. 155, p. 106148, 2019.

[15] P. G. Cojutti, M. Merelli, L. Allegri, G. Damante, M. Bassetti, and F. Pea, "Successful and safe long-term treatment of cerebral aspergillosis with high-dose voriconazole guided by therapeutic drug monitoring," *British Journal of Clinical Pharmacology*, vol. 85, no. 1, pp. 266–269, 2019.

[16] T. Buclin, Y. Thoma, N. Widmer, P. André, M. Guidi, C. Csajka, and L. A. Decosterd, "The steps to therapeutic drug monitoring: A structured approach illustrated with imatinib," *Frontiers in Pharmacology*, vol. 11, p. 177, 2020.

[17] J. J. Lee, J. H. Beumer, and E. Chu, "Therapeutic drug monitoring of 5-fluorouracil," *Cancer Chemotherapy and Pharmacology*, vol. 78, no. 3, pp. 447–464, 2016.

[18] D. C. Richter, O. Frey, A. Röhr, J. A. Roberts, A. Köberer, T. Fuchs, N. Papadimas, M. Heinzel-Gutenbrunner, T. Brenner, C. Lichtenstern *et al.*, "Therapeutic drug monitoring-guided continuous infusion of piperacillin/tazobactam significantly improves pharmacokinetic target attainment in critically ill patients: a retrospective analysis of four years of clinical experience," *Infection*, vol. 47, no. 6, pp. 1001–1011, 2019.

[19] R. J. Nies, C. Müller, R. Pfister, P. S. Binder, N. Nosseir, F. S. Nettersheim, K. Kuhr, M. H. Wiesen, M. Kochanek, and G. Michels, "Monitoring of sedation depth in intensive care unit by therapeutic drug monitoring? A prospective observation study of medical intensive care patients," *Journal of Intensive Care*, vol. 6, no. 1, pp. 1–8, 2018.

[20] A. C. Cartwright and N. A. Armstrong, *A History of the Medicines We Take: From Ancient Times to Present Day.* Pen and Sword History, 2020.

[21] D. Lee-Parritz, "Animal care and maintenance," in *Surgical Research.* Academic Press, 2001, pp. 47–61.

[22] T. D. Egan, "Total intravenous anesthesia versus inhalation anesthesia: a drug delivery perspective," *Journal of Cardiothoracic and Vascular Anesthesia*, vol. 29, pp. S3–S6, 2015.

[23] C. D. Kent and K. B. Domino, "Depth of anesthesia," *Current Opinion in Anesthesiology*, vol. 22, no. 6, pp. 782–787, 2009.

[24] R. D. Miller, L. Eriksson, L. A. Fleisher, J. P. Wiener-Kronish, and W. L. Young, "Miller's anesthesia," in *Miller's Anesthesia*, 2010, pp. 2827–2827.

[25] J. Kanto and E. Gepts, "Pharmacokinetic implications for the clinical use of propofol," *Clinical Pharmacokinetics*, vol. 17, no. 5, pp. 308–326, 1989.

[26] Y. Ishizawa, "Mechanisms of anesthetic actions and the brain," *Journal of Anesthesia*, vol. 21, no. 2, pp. 187–199, 2007.

[27] M. M. Sahinovic, M. M. Struys, and A. R. Absalom, "Clinical pharmacokinetics and pharmacodynamics of propofol," *Clinical Pharmacokinetics*, vol. 57, no. 12, pp. 1539–1558, 2018.

[28] K. Peng, H.-Y. Liu, S.-R. Wu, H. Liu, Z.-C. Zhang, and F.-H. Ji, "Does propofol anesthesia lead to less postoperative pain compared with inhalational anesthesia?: a systematic review and meta-analysis," *Anesthesia and Analgesia*, vol. 123, no. 4, pp. 846–858, 2016.

[29] D. M. Philbin, C. E. Rosow, R. C. Schneider, G. Koski, and M. N. D'Ambra, "Fentanyl and sufentanil anesthesia revisited: How much is enough?" *Anesthesiology: The Journal of the American Society of Anesthesiologists*, vol. 73, no. 1, pp. 5–11, 1990.

[30] G. G. Graham and K. F. Scott, "Mechanism of action of paracetamol," *American Journal of Therapeutics*, vol. 12, no. 1, pp. 46–55, 2005.

[31] H. Borazan, T. B. Erdem, M. Kececioglu, and S. Otelcioglu, "Prevention of pain on injection of propofol: a comparison of lidocaine with different doses of paracetamol," *European Journal of Anaesthesiology*, vol. 27, no. 3, pp. 253–257, 2010.

[32] Y.-T. Jeon, A.-Y. Oh, S.-H. Park, J.-W. Hwang, and H.-P. Park, "Optimal remifentanil dose for lightwand intubation without muscle relaxants in healthy patients with thiopental coadministration: a prospective randomised study," *European Journal of Anaesthesiology*, vol. 29, no. 11, pp. 520–523, 2012.

[33] E. Kirmeier, L. I. Eriksson, H. Lewald, M. J. Fagerlund, A. Hoeft, M. Hollmann, C. Meistelman, J. M. Hunter, K. Ulm, M. Blobner *et al.*, "Post-anaesthesia pulmonary complications after use of muscle relaxants (POPULAR): a multicentre, prospective observational study," *The Lancet Respiratory Medicine*, vol. 7, no. 2, pp. 129–140, 2019.

[34] R. Goldman, "Michael Jackson had 'lethal levels' of propofol before death," *ABC News*, 24 Aug 2009.

[35] C. C. Apfel, E. Läärä, M. Koivuranta, C.-A. Greim, and N. Roewer, "A simplified risk score for predicting postoperative nausea and vomiting conclusions from cross-validations between two centers," *Anesthesiology: The Journal of the American Society of Anesthesiologists*, vol. 91, no. 3, pp. 693–693, 1999.

[36] S. A. K. Craig and R. Kitson, "Risks associated with anaesthesia," *Anaesthesia and Intensive Care Medicine*, vol. 11, no. 11, pp. 464–468, 2010.

[37] M. J. Murray, S. H. Rose, D. J. Wedel, C. T. Wass, B. A. Harrison, J. T. Mueller, and T. L. Trentman, *Faust's anesthesiology review E-book: expert consult*. Elsevier Health Sciences, 2014.

[38] G. T. Carter, V. Duong, S. Ho, K. C. Ngo, C. L. Greer, and D. L. Weeks, "Side effects of commonly prescribed analgesic medications," *Physical Medicine and Rehabilitation Clinics*, vol. 25, no. 2, pp. 457–470, 2014.

[39] D. Ranum, H. Ma, F. E. Shapiro, B. Chang, and R. D. Urman, "Analysis of patient injury based on anesthesiology closed claims data from a major malpractice insurer," *Journal of Healthcare Risk Management*, vol. 34, no. 2, pp. 31–42, 2014.

[40] L. Chang, Q. Luo, Y. Chai, and H. Shu, "Accidental awareness while under general anaesthesia," *Bioscience Trends*, vol. 13, no. 4, pp. 364–366, 2019.

[41] H. Vulser and G. Lebeau, "Post-traumatic stress disorder following intraoperative awareness," in *General Anesthesia Research*. Springer, 2020, pp. 97–107.

[42] A. Argo, S. Zerbo, A. Lanzarone, R. Buscemi, R. Roccuzzo, and S. B. Karch, "Perioperative and anesthetic deaths: toxicological and medico legal aspects," *Egyptian Journal of Forensic Sciences*, vol. 9, no. 1, p. 20, 2019.

[43] J. Hendrickx and A. De Wolf, "Special aspects of pharmacokinetics of inhalation anesthesia," in *Modern Anesthetics*. Springer, 2008, pp. 159–186.

[44] A. R. Absalom and K. P. Mason, *Total intravenous anesthesia and target controlled infusions*. Springer, 2017.

[45] Z. Al-Rifai and D. Mulvey, "Principles of total intravenous anaesthesia: basic pharmacokinetics and model descriptions," *Bja Education*, vol. 16, no. 3, pp. 92–97, 2016.

[46] H.-C. Lee, H.-G. Ryu, E.-J. Chung, and C.-W. Jung, "Prediction of bispectral index during target-controlled infusion of propofol and remifentanil," *Anesthesiology*, vol. 128, no. 3, pp. 492–501, 2018.

[47] R. Eyres, "Update on TIVA," *Pediatric Anesthesia*, vol. 14, no. 5, pp. 374–379, 2004.

[48] R. Shalbaf, H. Behnam, and H. J. Moghadam, "Monitoring depth of anesthesia using combination of EEG measure and hemodynamic variables," *Cognitive Neurodynamics*, vol. 9, no. 1, pp. 41–51, 2015.

[49] J.-L. Casteleiro-Roca, J. L. Calvo-Rolle, J. A. Méndez Pérez, N. Roqueni Gutierrez, and F. J. de Cos Juez, "Hybrid intelligent system to perform fault detection on BIS sensor during surgeries," *Sensors*, vol. 17, no. 1, p. 179, 2017.

[50] J. C. Sigl and N. G. Chamoun, "An introduction to bispectral analysis for the electroencephalogram," *Journal of Clinical Monitoring*, vol. 10, no. 6, pp. 392–404, 1994.

[51] A. Arslan, B. Şen, F. V. Çelebi, M. Peker, and A. But, "A comparison of different classification algorithms for determining the depth of anesthesia level on a new set of attributes," in *2015 International Symposium on Innovations Intelligent Systems and Applications (INISTA)*, Madrid, Spain, 2015, pp. 1–7.

[52] S. D. Kelley, *Monitoring consciousness using the bispectral index during anesthesia. A pocket guide for clinicians.* Covidien, 2007.

[53] Z. Hajat, N. Ahmad, and J. Andrzejowski, "The role and limitations of EEG-based depth of anaesthesia monitoring in theatres and intensive care," *Anaesthesia*, vol. 72, pp. 38–47, 2017.

[54] S. K. Metkar and K. Girigoswami, "Diagnostic biosensors in medicine–a review," *Biocatalysis and Agricultural Biotechnology*, vol. 17, pp. 271–283, 2019.

[55] M. Cuartero, G. Crespo, T. Cherubini, N. Pankratova, F. Confalonieri, F. Massa, M.-L. Tercier-Waeber, M. Abdou, J. Schäfer, and E. Bakker, "In situ detection of macronutrients and chloride in seawater by submersible electrochemical sensors," *Analytical Chemistry*, vol. 90, no. 7, pp. 4702–4710, 2018.

[56] B. Meshram, A. Agrawal, S. Adil, S. Ranvir, and K. Sande, "Biosensor and its application in food and dairy industry: A review," *International Journal of Current Microbiology and Applied Sciences*, vol. 7, pp. 3305–3324, 2018.

[57] N. Bhalla, P. Jolly, N. Formisano, and P. Estrela, "Introduction to biosensors," *Essays in biochemistry*, vol. 60, no. 1, p. 8, 2016.

[58] F.-G. Banica, *Chemical sensors and biosensors: fundamentals and applications*. John Wiley & Sons, 2012.

[59] A. Tuoheti, S. Aiassa, F. Criscuolo, F. Stradolini, I. Tzouvadaki, S. Carrara, and D. Demarchi, "New approach for making standard the development of biosensing devices by a modular multi-purpose design," *IEEE Transactions on NanoBioscience*, vol. 19, no. 3, pp. 339–346, 2020.

[60] A. Shafiee, E. Ghadiri, J. Kassis, and A. Atala, "Nanosensors for therapeutic drug monitoring: implications for transplantation," *Nanomedicine*, no. 0, 2019.

[61] K. Malpartida-Cardenas, N. Miscourides, J. Rodriguez-Manzano, L.-S. Yu, N. Moser, J. Baum, and P. Georgiou, "Quantitative and rapid plasmodium falciparum malaria diagnosis and artemisinin-resistance detection using a CMOS lab-on-chip platform," *Biosensors and Bioelectronics*, vol. 145, p. 111678, 2019.

[62] C. Dincer, R. Bruch, E. Costa-Rama, M. T. Fernández-Abedul, A. Merkoçi, A. Manz, G. A. Urban, and F. Güder, "Disposable sensors in diagnostics, food, and environmental monitoring," *Advanced Materials*, vol. 31, no. 30, p. 1806739, 2019.

[63] S. Sang, W. Zhang, and Y. Zhao, "State of the art in biosensors-general aspects," in *Review on the design art of biosensors*, T. Rinken, Ed. Intech, 2013, pp. 89–110.

[64] A. J. Bard, L. R. Faulkner, J. Leddy, and C. G. Zoski, "Potential sweep method," in *Electrochemical Methods: Fundamentals and Applications*, 2nd ed. New York: Wiley, 1980, pp. 226–260.

[65] Y. Q. Fu, J. Luo, N.-T. Nguyen, A. Walton, A. J. Flewitt, X.-T. Zu, Y. Li,

G. McHale, A. Matthews, E. Iborra *et al.*, "Advances in piezoelectric thin films for acoustic biosensors, acoustofluidics and lab-on-chip applications," *Progress in Materials Science*, vol. 89, pp. 31–91, 2017.

[66] R. B. Schasfoort, *Handbook of surface plasmon resonance*. Royal Society of Chemistry, 2017.

[67] S. A. Pidenko, N. A. Burmistrova, A. A. Shuvalov, A. A. Chibrova, Y. S. Skibina, and I. Y. Goryacheva, "Microstructured optical fiber-based luminescent biosensing: Is there any light at the end of the tunnel?-a review," *Analytica Chimica Acta*, vol. 1019, pp. 14–24, 2018.

[68] O. Simoska, M. Sans, M. D. Fitzpatrick, C. M. Crittenden, L. S. Eberlin, J. B. Shear, and K. J. Stevenson, "Real-time electrochemical detection of pseudomonas aeruginosa phenazine metabolites using transparent carbon ultramicroelectrode arrays," *ACS Sensors*, vol. 4, no. 1, pp. 170–179, 2018.

[69] Q. He, Y. Tian, Y. Wu, J. Liu, G. Li, P. Deng, and D. Chen, "Electrochemical sensor for rapid and sensitive detection of tryptophan by a Cu2O nanoparticles-coated reduced graphene oxide nanocomposite," *Biomolecules*, vol. 9, no. 5, p. 176, 2019.

[70] M. La, C. Chen, X. Xia, and J. Z. B. Zhou, "Electrochemical, photoelectrochemical and electrochemiluminescent biosensors for the detection of beta-amyloid peptides and their aggregates," *International Journal of Electrochemical Science*, vol. 14, pp. 5547–5562, 2019.

[71] M. Puiu, A. Idili, D. Moscone, F. Ricci, and C. Bala, "A modular electrochemical peptide-based sensor for antibody detection," *Chemical Communications*, vol. 50, no. 64, pp. 8962–8965, 2014.

[72] L. Guo, Z. Yang, S. Zhi, Z. Feng, C. Lei, and Y. Zhou, "A sensitive and innovative detection method for rapid c-reactive proteins analysis based on a micro-fluxgate sensor system," *PloS One*, vol. 13, no. 3, p. e0194631, 2018.

[73] S. Carrara, D. Sacchetto, M.-A. Doucey, C. Baj-Rossi, G. De Micheli, and Y. Leblebici, "Memristive-biosensors: A new detection method by using nanofabricated memristors," *Sensors and Actuators B: Chemical*, vol. 171, pp. 449–457, 2012.

[74] I. Tzouvadaki, P. Jolly, X. Lu, S. Ingebrandt, G. De Micheli, P. Estrela, and S. Carrara, "Label-free ultrasensitive memristive aptasensor," *Nano Letters*, vol. 16, no. 7, pp. 4472–4476, 2016.

[75] T. Kilic, A. Erdem, M. Ozsoz, and S. Carrara, "microRNA biosensors: opportunities and challenges among conventional and commercially available techniques," *Biosensors and Bioelectronics*, vol. 99, pp. 525–546, 2018.

[76] S. Aiassa, R. Terracciano, S. Carrara, and D. Demarchi, "Biosensors for biomolecular computing: a review and future perspectives," *BioNanoScience*, vol. 10, no. 3, pp. 554–563, 2020.

[77] E. Witkowska Nery, M. Kundys, P. S. Jeleń, and M. Jönsson-Niedziółka,

"Electrochemical glucose sensing: Is there still room for improvement?" *Analytical Chemistry*, vol. 88, no. 23, pp. 11 271–11 282, 2016.

[78] H. Teymourian, A. Barfidokht, and J. Wang, "Electrochemical glucose sensors in diabetes management: an updated review (2010–2020)," *Chemical Society Reviews*, 2020.

[79] G. L. Barbruni, P. Motto Ros, S. Aiassa, D. Demarchi, and S. Carrara, "Body dust: Ultra-low power ook modulation circuit for wireless data transmission in drinkable sub-100µm-sized biochips," arXiv:1912.02670 [physics.ins-det], arXiv, 2019.

[80] N. Aliakbarinodehi, G. De Micheli, and S. Carrara, "Optimized electrochemical detection of anti-cancer drug by carbon nanotubes or gold nanoparticles," in *2015 11th Conference on Ph. D. Research in Microelectronics and Electronics (PRIME)*. Glasgow, Scotland: IEEE, 2015, pp. 25–28.

[81] F. M. Zahed, B. Hatamluyi, F. Lorestani, and Z. Es'haghi, "Silver nanoparticles decorated polyaniline nanocomposite based electrochemical sensor for the determination of anticancer drug 5-fluorouracil," *Journal of Pharmaceutical and Biomedical Analysis*, vol. 161, pp. 12–19, 2018.

[82] N. P. Shetti, S. J. Malode, D. S. Nayak, T. M. Aminabhavi, and K. R. Reddy, "Nanostructured silver doped TiO2/CNTs hybrid as an efficient electrochemical sensor for detection of anti-inflammatory drug, cetirizine," *Microchemical Journal*, vol. 150, p. 104124, 2019.

[83] S. Ansari, M. S. Ansari, S. Satsangee, and R. Jain, "WO3 decorated graphene nanocomposite based electrochemical sensor: a prospect for the detection of anti-anginal drug," *Analytica Chimica Acta*, vol. 1046, pp. 99–109, 2019.

[84] M. Elfiky, N. Salahuddin, A. Hassanein, A. Matsuda, and T. Hattori, "Detection of antibiotic ofloxacin drug in urine using electrochemical sensor based on synergistic effect of different morphological carbon materials," *Microchemical Journal*, vol. 146, pp. 170–177, 2019.

[85] T. E. Chiwunze, V. N. Palakollu, A. A. Gill, F. Kayamba, N. B. Thapliyal, and R. Karpoormath, "A highly dispersed multi-walled carbon nanotubes and poly (methyl orange) based electrochemical sensor for the determination of an anti-malarial drug: Amodiaquine," *Materials Science and Engineering: C*, vol. 97, pp. 285–292, 2019.

[86] S. Szabó and I. Bakos, "Reference electrodes in metal corrosion," *International Journal of Corrosion*, vol. 2010, 2010.

[87] A. Bard, *Electrochemical methods: fundamentals and applications*. New York: Wiley, 2001.

[88] F. G. Cottrell, "Der reststrom bei galvanischer polarisation, betrachtet als ein diffusionsproblem," *Zeitschrift für Physikalische Chemie*, vol. 42, no. 1, pp. 385–431, 1903.

[89] N. Elgrishi, K. J. Rountree, B. D. McCarthy, E. S. Rountree, T. T. Eisenhart, and J. L. Dempsey, "A practical beginner's guide to cyclic voltammetry,"

Journal of Chemical Education, vol. 95, no. 2, pp. 197–206, 2018.

[90] J. E. B. Randles, "A cathode ray polarograph. Part II.–The current-voltage curves," *Transactions of the Faraday Society*, vol. 44, pp. 327–338, 1948.

[91] A. Ševčík, "Oscillographic polarography with periodical triangular voltage," *Collection of Czechoslovak Chemical Communications*, vol. 13, pp. 349–377, 1948.

[92] L. Busoni, M. Carla, and L. Lanzi, "A comparison between potentiostatic circuits with grounded work or auxiliary electrode," *Review of Scientific Instruments*, vol. 73, no. 4, pp. 1921–1923, 2002.

[93] Metrohm, *Basic overview of the working principle of a potentiostat/galvanostat (PGSTAT) – Electrochemical cell setup*, accessed on: 22 Sept 2020. [Online]. Available: https://www.metrohm.com/en-gb/applications/AN-EC-008.

[94] G. Lavanya, M. Sunil, M. Eswarudu, M. C. Eswaraiah, K. Harisudha, and B. N. Spandana, "Analytical method validation: An updated review," *International Journal of Pharmaceutical Sciences and Research*, vol. 4, no. 4, p. 1280, 2013.

[95] K. L. Baker, F. B. Bolger, M. M. Doran, and J. P. Lowry, "Characterisation of a platinum-based electrochemical biosensor for real-time neurochemical analysis of choline," *Electroanalysis*, vol. 31, no. 1, pp. 129–136, 2019.

[96] D. R. Thévenot, K. Toth, R. A. Durst, and G. S. Wilson, "Electrochemical biosensors: recommended definitions and classification," *Biosensors and Bioelectronics*, vol. 16, no. 1-2, pp. 121–131, 2001.

[97] O. B. da Silva and S. A. Machado, "Evaluation of the detection and quantification limits in electroanalysis using two popular methods: application in the case study of paraquat determination," *Analytical Methods*, vol. 4, no. 8, pp. 2348–2354, 2012.

[98] S. Aiassa, S. Yilmaz, S. Carrara, and D. Demarchi, "Pencil graphite needle-shaped biosensor for anaesthetic monitoring in human serum," in *2020 IEEE Sensors*, Rotterdam, Nederland, 2020, pp. 1–4.

[99] S. Aiassa, S. Carrara, and D. Demarchi, "Optimized sampling rate for voltammetry-based electrochemical sensing in wearable and IoT applications," *IEEE Sensors Letters*, vol. 3, no. 6, pp. 1–4, 2019.

[100] S. Aiassa, J. D. Martínez González, D. Demarchi, and S. Carrara, "New measurement method in drug sensing by direct total-charge detection in voltammetry," in *2020 IEEE International Symposium on Medical Measurements and Applications (MeMeA)*, Bari, Italy, 2020, pp. 1–6.

[101] S. Aiassa, I. Ny Hanitra, G. Sandri, T. Totu, F. Grassi, F. Criscuolo, G. De Micheli, S. Carrara, and D. Demarchi, "Continuous monitoring of propofol in human serum with fouling compensation by support vector classifier," *Biosensors and Bioelectronics*, vol. 171, p. 112666, 2021.

[102] S. Aiassa, F. Stradolini, A. Tuoheti, S. Carrara, and D. Demarchi, "Quasi-digital biosensor-interface for a portable pen to monitor anaesthetics delivery," in *2019 15th Conference on Ph.D Research in Microelectronics and Electronics (PRIME)*, Lausanne, Switzerland, 2019, pp. 265–268.

[103] S. Aiassa, F. Grassi, R. Terracciano, S. Carrara, and D. Demarchi, "Live demonstration: Quasi-digital portable pen to monitor anaesthetics delivery," in *2019 IEEE Biomedical Circuits and Systems Conference (BioCAS)*, Nara, Japan, 2019, p. 1.

[104] S. Aiassa, S. Carrara, and D. Demarchi, "Event-based portable pen for monitoring anaesthetics delivery," EasyChair Preprint no. 2841, EasyChair, 2020.

[105] S. Aiassa, P. Motto Ros, M. I. Ny Hanitra, D. Tunzi, M. Martina, S. Carrara, and D. Demarchi, "Smart portable pen for continuous classification of anaesthetics concentration in human serum with machine learning," *IEEE Transactions on Biomedical Circuits and Systems*, pp. 1–4, 2021.

[106] V. L. D. S. N. Button, "Chapter 1 - introduction to biomedical variables transducing," in *Principles of Measurement and Transduction of Biomedical Variables*, V. L. D. S. N. Button, Ed. Oxford: Academic Press, 2015, pp. 1 – 24.

[107] E. Naghian, E. M. Khosrowshahi, E. Sohouli, F. Ahmadi, M. Rahimi-Nasrabadi, and V. Safarifard, "A new electrochemical sensor for the detection of fentanyl lethal drug by a screen-printed carbon electrode modified with the open-ended channels of Zn (ii)-MOF," *New Journal of Chemistry*, 2020.

[108] S. H. Youssef, D. Mohamed, M. A. Hegazy, and A. Badawey, "Green liquid chromatographic methods with ultraviolet and tandem mass spectrometry detection: an application to ternary mixture of paracetamol, pseudoephedrine, and cetirizine in capsules," *Journal of AOAC International*, vol. 103, no. 1, pp. 148–155, 2020.

[109] P. Prajapati, H. Shah, and S. A. Shah, "Implementation of QRM and DoE-Based quality by design approach to VEER chromatography method for simultaneous estimation of multiple combined dosage forms of paracetamol," *Journal of Pharmaceutical Innovation*, pp. 1–17, 2020.

[110] M. Y. Fares, N. S. Abdelwahab, M. M. Abdelrahman, and H. M. Abdel-Rahman, "Determination of sofosbuvir with two co-administered drugs; paracetamol and DL-methionine by two chromatographic methods. application to a pharmacokinetic study," *Bioanalysis*, vol. 11, no. 05, pp. 349–364, 2019.

[111] E. Ziemons, J. Mantanus, P. Lebrun, E. Rozet, B. Evrard, and P. Hubert, "Acetaminophen determination in low-dose pharmaceutical syrup by NIR spectroscopy," *Journal of Pharmaceutical and Biomedical Analysis*, vol. 53, no. 3, pp. 510–516, 2010.

[112] R. Szostak and S. Mazurek, "Quantitative determination of acetylsalicylic acid and acetaminophen in tablets by FT-Raman spectroscopy," *Analyst*, vol.

127, no. 1, pp. 144–148, 2002.

[113] P. Fanjul-Bolado, P. J. Lamas-Ardisana, D. Hernández-Santos, and A. Costa-García, "Electrochemical study and flow injection analysis of paracetamol in pharmaceutical formulations based on screen-printed electrodes and carbon nanotubes," *Analytica Chimica Acta*, vol. 638, no. 2, pp. 133–138, 2009.

[114] S.-F. Wang, F. Xie, and R.-F. Hu, "Carbon-coated nickel magnetic nanoparticles modified electrodes as a sensor for determination of acetaminophen," *Sensors and Actuators B: Chemical*, vol. 123, no. 1, pp. 495–500, 2007.

[115] F. Stradolini, T. Elboshra, A. Biscontini, G. De Micheli, and S. Carrara, "Simultaneous monitoring of anesthetics and therapeutic compounds with a portable multichannel potentiostat," in *2016 IEEE International Symposium on Circuits and Systems (ISCAS)*, Montreal, Canada, 2016, pp. 834–837.

[116] R. Jain and R. K. Yadav, "Voltammetric behavior of sedative drug midazolam at glassy carbon electrode in solubilized systems," *Journal of Pharmaceutical Analysis*, vol. 2, no. 2, pp. 123–129, 2012.

[117] M. V. Antunes, M. F. Charão, and R. Linden, "Dried blood spots analysis with mass spectrometry: potentials and pitfalls in therapeutic drug monitoring," *Clinical biochemistry*, vol. 49, no. 13-14, pp. 1035–1046, 2016.

[118] J. Yarbrough, R. Harvey, and S. Cox, "Determination of propofol using high performance liquid chromatography in whole blood with fluorescence detection," *Journal of Chromatographic Science*, vol. 50, no. 3, pp. 162–166, 2012.

[119] F. Vaiano, G. Serpelloni, M. Focardi, A. Fioravanti, F. Mari, and E. Bertol, "LC–MS/MS and GC–MS methods in propofol detection: Evaluation of the two analytical procedures," *Forensic Science International*, vol. 256, pp. 1–6, 2015.

[120] D. Parriott, *A practical guide to HPLC detection*. Academic Press, 2012.

[121] G. Brandhorst, M. Oellerich, G. Maine, P. Taylor, G. Veen, and P. Wallemacq, "Liquid chromatography–tandem mass spectrometry or automated immunoassays: what are the future trends in therapeutic drug monitoring?" *Clinical Chemistry*, vol. 58, no. 5, pp. 821–825, 2012.

[122] G. Harrison, A. Critchley, C. Mayhew, and J. Thompson, "Real-time breath monitoring of propofol and its volatile metabolites during surgery using a novel mass spectrometric technique: a feasibility study," *British Journal of Anaesthesia*, vol. 91, no. 6, pp. 797–799, 2003.

[123] W. Miekisch, P. Fuchs, S. Kamysek, C. Neumann, and J. K. Schubert, "Assessment of propofol concentrations in human breath and blood by means of HS-SPME–GC–MS," *Clinica Chimica Acta*, vol. 395, no. 1-2, pp. 32–37, 2008.

[124] H. Dong, F. Zhang, Y. Wang, F. Wang, J. Chen, K. G. Muhammad, and X. Chen, "Sniffing sevoflurane and propofol in exhalation from patients during balanced anesthesia," in *2017 ISOCS/IEEE International Symposium on Olfaction and Electronic Nose (ISOEN)*, Montreal, Canada, 2017, pp. 1–3.

[125] T. Perl, E. Carstens, A. Hirn, M. Quintel, W. Vautz, J. Nolte, and M. Jünger, "Determination of serum propofol concentrations by breath analysis using ion mobility spectrometry," *British Journal of Anaesthesia*, vol. 103, no. 6, pp. 822–827, 2009.

[126] F. Zhang, H. Dong, X. Zhang, J. Guo, Y. Liu, C. Zhou, X. Zhang, J. Liu, M. Yan, and X. Chen, "A non-invasive monitoring of propofol concentration in blood by a virtual surface acoustic wave sensor array," *Analytical Sciences*, vol. 33, no. 11, pp. 1271–1277, 2017.

[127] S.-Z. Fan, H.-Y. Yu, Y.-L. Chen, and C.-C. Liu, "Propofol concentration monitoring in plasma or whole blood by gas chromatography and high-performance liquid chromatography," *Anesthesia and Analgesia*, vol. 81, no. 1, pp. 175–178, 1995.

[128] F. Kivlehan, F. Garay, J. Guo, E. Chaum, and E. Lindner, "Toward feedback-controlled anesthesia: voltammetric measurement of propofol (2, 6-diisopropylphenol) in serum-like electrolyte solutions," *Analytical Chemistry*, vol. 84, no. 18, pp. 7670–7676, 2012.

[129] F. Stradolini, T. Kilic, A. Di Consiglio, M. Ozsoz, G. De Micheli, and S. Carrara, "Long-term monitoring of propofol and fouling effect on pencil graphite electrodes," *Electroanalysis*, vol. 30, no. 7, pp. 1363–1369, 2018.

[130] H. Purushothama, Y. A. Nayaka, M. Vinay, P. Manjunatha, R. Yathisha, and K. Basavarajappa, "Pencil graphite electrode as an electrochemical sensor for the voltammetric determination of chlorpromazine," *Journal of Science: Advanced Materials and Devices*, vol. 3, no. 2, pp. 161–166, 2018.

[131] A. Özcan and Y. Şahin, "Preparation of selective and sensitive electrochemically treated pencil graphite electrodes for the determination of uric acid in urine and blood serum," *Biosensors and Bioelectronics*, vol. 25, no. 11, pp. 2497–2502, 2010.

[132] Metrohm DropSens, *Screen-Printed Carbon Electrodes Refs. 110, C110, C11L*, accessed on: 7 May 2019. [Online]. Available: http://www.dropsens.com/en/pdfs_productos/new_brochures/ 110-c110-c11l.pdf.

[133] S. Carrara, *Bio/CMOS Interfaces and Co-Design*, 1st ed. New York: Springer Science & Business Media, 2013.

[134] J. Langmaier, F. Garay, F. Kivlehan, E. Chaum, and E. Lindner, "Electrochemical quantification of 2, 6-diisopropylphenol (propofol)," *Analytica Chimica Acta*, vol. 704, no. 1-2, pp. 63–67, 2011.

[135] B. Heyne, S. Kohnen, D. Brault, A. Mouithys-Mickalad, F. Tfibel, P. Hans, M.-P. Fontaine-Aupart, and M. Hoebeke, "Investigation of singlet oxygen reactivity towards propofol," *Photochemical and Photobiological Sciences*, vol. 2, no. 9, pp. 939–945, 2003.

[136] F. Stradolini, T. Kilic, I. Taurino, G. De Micheli, and S. Carrara, "Cleaning strategy for carbon-based electrodes: Long-term propofol monitoring in

human serum," *Sensors and Actuators B: Chemical*, vol. 269, pp. 304–313, 2018.

[137] X. Yang, J. Kirsch, J. Fergus, and A. Simonian, "Modeling analysis of electrode fouling during electrolysis of phenolic compounds," *Electrochimica Acta*, vol. 94, pp. 259–268, 2013.

[138] G. W. Muna, M. Partridge, H. Sirhan, B. VerVaet, N. Guerra, and H. Garner, "Electrochemical detection of steroid hormones using a nickel-modified glassy carbon electrode," *Electroanalysis*, vol. 26, no. 10, pp. 2145–2151, 2014.

[139] I. Tzouvadaki, N. Aliakbarinodehi, D. D. Pineda, G. De Micheli, and S. Carrara, "Graphene nanowalls for high-performance chemotherapeutic drug sensing and anti-fouling properties," *Sensors and Actuators B: Chemical*, vol. 262, pp. 395–403, 2018.

[140] P. Puthongkham and B. J. Venton, "Nanodiamond coating improves the sensitivity and antifouling properties of carbon fiber microelectrodes," *ACS Sensors*, vol. 4, no. 9, pp. 2403–2411, 2019.

[141] M. Daramola, O. Sadare, O. Oluwasina, and S. Iyuke, "Synthesis and application of functionalized carbon nanotube infused polymer membrane (fCNT/PSF/PVA) for treatment of phenol-containing wastewater," *Journal of Membrane Science and Research*, vol. 5, no. 4, pp. 310–316, 2019.

[142] Y. S. Singh, L. E. Sawarynski, P. D. Dabiri, W. R. Choi, and A. M. Andrews, "Head-to-head comparisons of carbon fiber microelectrode coatings for sensitive and selective neurotransmitter detection by voltammetry," *Analytical Chemistry*, vol. 83, no. 17, pp. 6658–6666, 2011.

[143] I. S. da Silva, B. Capovilla, K. H. G. Freitas, and L. Angnes, "Strategies to avoid electrode fouling for nimesulide detection using unmodified electrodes," *Analytical Methods*, vol. 5, no. 14, pp. 3546–3551, 2013.

[144] X. Wang, J. Che, M. Wu, Y. Shi, M. Li, J. Shan, and L. Liu, "The antifouling effect of surfactants and its application for electrochemical detection of bisphenol A," *Journal of The Electrochemical Society*, vol. 165, no. 16, pp. B814–B823, 2018.

[145] F. Kivlehan, E. Chaum, and E. Lindner, "Propofol detection and quantification in human blood: the promise of feedback controlled, closed-loop anesthesia," *Analyst*, vol. 140, no. 1, pp. 98–106, 2015.

[146] C.-C. Hong, C.-C. Lin, C.-L. Hong, Z.-X. Lin, M.-H. Chung, and P.-W. Hsieh, "Handheld analyzer with on-chip molecularly-imprinted biosensors for electrical detection of propofol in plasma samples," *Biosensors and Bioelectronics*, vol. 86, pp. 623–629, 2016.

[147] F. Stradolini, A. Tuoheti, T. Kilic, S. L. Ntella, N. Tamburrano, Z. Huang, G. De Micheli, D. Demarchi, and S. Carrara, "An IoT solution for online monitoring of anesthetics in human serum based on an integrated fluidic bioelectronic system," *IEEE Transactions on Biomedical Circuits and Systems*, vol. 12, no. 5, pp. 1056–1064, 2018.

[148] C. A. Knibbe, K. P. Zuideveld, L. P. Aarts, P. F. Kuks, and M. Danhof, "Allometric relationships between the pharmacokinetics of propofol in rats, children and adults," *British journal of clinical pharmacology*, vol. 59, no. 6, pp. 705–711, 2005.

[149] A. Kumar, B. Purohit, P. K. Maurya, L. M. Pandey, and P. Chandra, "Engineered nanomaterial assisted signal-amplification strategies for enhancing analytical performance of electrochemical biosensors," *Electroanalysis*, vol. 31, no. 9, pp. 1615–1629, 2019.

[150] K. Mahato, P. K. Maurya, and P. Chandra, "Fundamentals and commercial aspects of nanobiosensors in point-of-care clinical diagnostics," *3 Biotech*, vol. 8, no. 3, p. 149, 2018.

[151] S. Nayak, N. R. Blumenfeld, T. Laksanasopin, and S. K. Sia, "Point-of-care diagnostics: Recent developments in a connected age," *Analytical Chemistry*, vol. 89, no. 1, pp. 102–123, Jan 2017.

[152] I. Ny Hanitra, L. Lobello, F. Stradolini, A. Tuoheti, F. Criscuolo, T. Kilic, D. Demarchi, S. Carrara, and G. De Micheli, "A flexible front-end for wearable electrochemical sensing," in *2018 IEEE International Symposium on Medical Measurements and Applications (MeMeA)*, Rome, Italy, 2018, pp. 1–6.

[153] X. Xuan, H. S. Yoon, and J. Y. Park, "A wearable electrochemical glucose sensor based on simple and low-cost fabrication supported micro-patterned reduced graphene oxide nanocomposite electrode on flexible substrate," *Biosensors and Bioelectronics*, vol. 109, pp. 75 – 82, 2018.

[154] M. W. Shinwari, D. Zhitomirsky, I. A. Deen, P. R. Selvaganapathy, M. J. Deen, and D. Landheer, "Microfabricated reference electrodes and their biosensing applications," *Sensors*, vol. 10, no. 3, pp. 1679–1715, 2010.

[155] F. Scholz, "Voltammetric techniques of analysis: the essentials," *ChemTexts*, vol. 1, no. 4, p. 17, Sep 2015.

[156] F. Stradolini, A. Tuoheti, P. Motto Ros, D. Demarchi, and S. Carrara, "Raspberry Pi based system for portable and simultaneous monitoring of anesthetics and therapeutic compounds," in *2017 New Generation CAS (NGCAS)*, Genova, Italy, 2017, pp. 101–104.

[157] A. Ainla, M. P. S. Mousavi, M.-N. Tsaloglou, J. Redston, J. G. Bell, M. T. Fernández-Abedul, and G. M. Whitesides, "Open-source potentiostat for wireless electrochemical detection with smartphones," *Analytical Chemistry*, vol. 90, no. 10, pp. 6240–6246, 2018.

[158] I. Siegl, C. Kollegger, C. Rabl, C. Steffan, and W. Pribyl, "NFC powered cyclic voltammetry with dynamic output voltage range exploitation," in *2018 12th International Conference on Sensing Technology (ICST)*, Limerick, Ireland, 2018, pp. 407–412.

[159] G. Ozcelikay, L. Karadurmus, S. I. Kaya, N. K. Bakirhan, and S. A. Ozkan, "A review: New trends in electrode systems for sensitive drug and biomolecule analysis," *Critical Reviews in Analytical Chemistry*, pp. 1–14, 2019.

[160] C. Baj-Rossi, G. De Micheli, and S. Carrara, "Electrochemical detection of anti-breast-cancer agents in human serum by cytochrome P450-coated carbon nanotubes," *Sensors*, vol. 12, no. 5, pp. 6520–6537, 2012.

[161] M. Esteban, C. Ariño, and J. Díaz-Cruz, "Chemometrics for the analysis of voltammetric data," *Trends in Analytical Chemistry*, vol. 25, no. 1, pp. 86–92, 2006.

[162] S. De Vito, E. Esposito, M. Salvato, O. Popoola, F. Formisano, R. Jones, and G. Di Francia, "Calibrating chemical multisensory devices for real world applications: An in-depth comparison of quantitative machine learning approaches," *Sensors and Actuators B: Chemical*, vol. 255, pp. 1191–1210, 2018.

[163] T. Wang, Y. Lu, Z. Cao, L. Shu, X. Zheng, A. Liu, and M. Xie, "When sensor-cloud meets mobile edge computing," *Sensors*, vol. 19, no. 23, p. 5324, 2019.

[164] M. del Valle, "Materials for electronic tongues: Smart sensor combining different materials and chemometric tools," in *Materials for Chemical Sensing*. Springer, 2017, pp. 227–265.

[165] C. Pérez-Ràfols, N. Serrano, C. Ariño, M. Esteban, and J. M. Díaz-Cruz, "Voltammetric electronic tongues in food analysis," *Sensors*, vol. 19, no. 19, p. 4261, 2019.

[166] M. del Valle, "Bioelectronic tongues employing electrochemical biosensors," in *Trends in Bioelectroanalysis*. Springer, 2016, pp. 143–202.

[167] Y.-L. He, Z.-Q. Geng, and Q.-X. Zhu, "Data driven soft sensor development for complex chemical processes using extreme learning machine," *Chemical Engineering Research and Design*, vol. 102, pp. 1–11, 2015.

[168] L. Rentería-Gutiérrez, F. F. González-Navarro, M. Stilianova-Stoytcheva, L. A. Belanche-Muñoz, B. L. Flores-Ríos, and J. E. Ibarra-Esquer, "Glucose oxidase biosensor modeling by machine learning methods," in *Mexican International Conference on Artificial Intelligence*, Tuxtla Gutierrez, Mexico, 2014, pp. 464–473.

[169] Y. Sheng, W. Qian, J. Huang, B. Wu, J. Yang, T. Xue, Y. Ge, and Y. Wen, "Electrochemical detection combined with machine learning for intelligent sensing of maleic hydrazide by using carboxylated PEDOT modified with copper nanoparticles," *Microchimica Acta*, vol. 186, no. 8, p. 543, 2019.

[170] I. M. Apetrei and C. Apetrei, "Voltammetric e-tongue for the quantification of total polyphenol content in olive oils," *Food Research International*, vol. 54, no. 2, pp. 2075–2082, 2013.

[171] X. Cetó, J. M. Gutiérrez, M. Gutiérrez, F. Céspedes, J. Capdevila, S. Mínguez, C. Jiménez-Jorquera, and M. del Valle, "Determination of total polyphenol index in wines employing a voltammetric electronic tongue," *Analytica Chimica Acta*, vol. 732, pp. 172–179, 2012.

[172] N. Maleki, S. Kashanian, E. Maleki, and M. Nazari, "A novel enzyme based

biosensor for catechol detection in water samples using artificial neural network," *Biochemical Engineering Journal*, vol. 128, pp. 1–11, 2017.

[173] X. Zhu, P. Liu, Y. Ge, R. Wu, T. Xue, Y. Sheng, S. Ai, K. Tang, and Y. Wen, "MoS2/MWCNTs porous nanohybrid network with oxidase-like characteristic as electrochemical nanozyme sensor coupled with machine learning for intelligent analysis of carbendazim," *Journal of Electroanalytical Chemistry*, vol. 862, p. 113940, 2020.

[174] Z. Li, S. Huang, and J. Chen, "A novel method for total chlorine detection using machine learning with electrode arrays," *RSC Advances*, vol. 9, no. 59, pp. 34 196–34 206, 2019.

[175] P. Puthongkham and B. J. Venton, "Recent advances in fast-scan cyclic voltammetry," *Analyst*, 2020.

[176] K. Aoki, J. Osteryoung, and R. A. Osteryoung, "Differential normal pulse voltammetry-theory," *Journal of Electroanalytical Chemistry and Interfacial Electrochemistry*, vol. 110, no. 1, pp. 1–18, 1980.

[177] A. Tobola, F. J. Streit, C. Espig, O. Korpok, C. Sauter, N. Lang, B. Schmitz, C. Hofmann, M. Struck, C. Weigand, H. Leutheuser, B. M. Eskofier, and G. Fischer, "Sampling rate impact on energy consumption of biomedical signal processing systems," in *2015 IEEE 12th International Conference on Wearable and Implantable Body Sensor Networks (BSN)*, Cambridge, MA, USA, 2015, pp. 1–6.

[178] A. N. Amos, J. G. Roberts, L. Qi, L. A. Sombers, and G. S. McCarty, "Reducing the sampling rate of biochemical measurements using fast-scan cyclic voltammetry for in vivo applications," *IEEE Sensors Journal*, vol. 14, no. 9, pp. 2975–2980, Sep. 2014.

[179] C. A. Lee, L. Qi, A. Amos, K. Blanton, G. S. McCarty, and L. A. Sombers, "Reducing data density in fast-scan cyclic voltammetry measurements of dopamine dynamics," *Journal of The Electrochemical Society*, vol. 165, no. 12, pp. 3042–3050, 2018.

[180] B. M. Kile, P. L. Walsh, Z. A. McElligott, E. S. Bucher, T. S. Guillot, A. Salahpour, M. G. Caron, and R. M. Wightman, "Optimizing the temporal resolution of fast-scan cyclic voltammetry," *ACS Chemical Neuroscience*, vol. 3, no. 4, pp. 285–292, 2012.

[181] Metrohm, *NOVA User manual*, accessed on: 4 Mar 2019. [Online]. Available: metrohm-autolab.com/download/NovaSoftware/User_manual_1.10.pdf.

[182] P. He, "Conversion of staircase voltammetry to linear sweep voltammetry by analog filtering," *Analytical Chemistry*, vol. 67, no. 5, pp. 986–992, 1995.

[183] F. Criscuolo, I. Ny Hanitra, S. Aiassa, I. Taurino, N. Oliva, S. Carrara, and G. De Micheli, "Wearable multifunctional sweat-sensing system for efficient healthcare monitoring," *Sensors and Actuators B: Chemical*, vol. 328, p. 129017, 2021.

[184] M. Schirmer, F. Stradolini, S. Carrara, and E. Chicca, "FPGA-based approach for automatic peak detection in cyclic voltammetry," in *2016 IEEE International Conference on Electronics, Circuits and Systems (ICECS)*, Monte Carlo, Monaco, 2016, pp. 65–68.

[185] P. Bezuidenhout, S. Smith, K. Land, and T. . Joubert, "A low-cost potentiostat for point-of-need diagnostics," in *2017 IEEE AFRICON*, Cape Town, South Africa, 2017, pp. 83–87.

[186] M. Capra, R. Peloso, G. Masera, M. Ruo Roch, and M. Martina, "Edge computing: A survey on the hardware requirements in the internet of things world," *Future Internet*, vol. 11, no. 4, p. 100, 2019.

[187] I. Anshori and H. Suzuki, "Electrochemical microdevices for proteins based on coulometry coupled with silver metallization," in *2017 19th International Conference on Solid-State Sensors, Actuators and Microsystems (TRANSDUCERS)*, Kaohsiung, Taiwan, 2017, pp. 1555–1558.

[188] C. Baj-Rossi, T. R. Jost, A. Cavallini, F. Grassi, G. De Micheli, and S. Carrara, "Continuous monitoring of naproxen by a cytochrome P450-based electrochemical sensor," *Biosensors and Bioelectronics*, vol. 53, pp. 283–287, 2014.

[189] S. Tumati, "Design of large time constant switched-capacitor filters for biomedical applications," Ph.D. dissertation, Texas A&M University, 2005.

[190] K. Nagaraj, "A parasitic-insensitive area-efficient approach to realizing very large time constants in switched-capacitor circuits," *IEEE Transactions on Circuits and Systems*, vol. 36, no. 9, pp. 1210–1216, 1989.

[191] H. G. Barrow, T. L. Naing, R. A. Schneider, T. O. Rocheleau, V. Yeh, Z. Ren, and C. T. Nguyen, "A real-time 32.768-kHz clock oscillator using a 0.0154-mm^2 micromechanical resonator frequency-setting element," in *2012 IEEE International Frequency Control Symposium Proceedings*, Baltimore, MD, USA, 2012, pp. 1–6.

[192] A. Hastings, *The Art of Analog Layout*. New Jersey: Pearson Prentice Hall, 2006, vol. 2.

[193] C. Cortes and V. Vapnik, "Support-vector networks," *Machine Learning*, vol. 20, no. 3, pp. 273–297, 1995.

[194] F. Pedregosa, G. Varoquaux, A. Gramfort, V. Michel, B. Thirion, O. Grisel, M. Blondel, P. Prettenhofer, R. Weiss, V. Dubourg, J. Vanderplas, A. Passos, D. Cournapeau, M. Brucher, M. Perrot, and E. Duchesnay, "Scikit-learn: Machine learning in Python," *Journal of Machine Learning Research*, vol. 12, pp. 2825–2830, 2011.

[195] C. C. Chang and C. J. Lin, "LIBSVM: A Library for support vector machines," *ACM Transactions on Intelligent Systems and Technology*, vol. 2, no. 3, pp. 1–39, 2011.

[196] F. Rainey, F. Kivlehan, E. Chaum, and E. Lindner, "Toward feedback controlled anesthesia: Automated flow analytical system for electrochemical

monitoring of propofol in serum solutions," *Electroanalysis*, vol. 26, no. 6, pp. 1295–1303, 2014.

[197] P. Motto Ros, M. Crepaldi, A. Damilano, and D. Demarchi, "Integrated bio-inspired systems: An event-driven design framework," in *2014 10th International Conference on Innovations in Information Technology (IIT)*, Abu Dhabi, United Arab Emirates, 2014, pp. 48–53.

[198] D. A. F. Guzman, S. Sapienza, B. Sereni, and P. Motto Ros, "Very low power event-based surface EMG acquisition system with off-the-shelf components," in *2017 IEEE Biomedical Circuits and Systems Conference (BioCAS)*, Turin, Italy, 2017, pp. 1–4.

[199] S. Aiassa, P. Motto Ros, G. Masera, and M. Martina, "A low power architecture for AER event-processing microcontroller," in *2017 IEEE Biomedical Circuits and Systems Conference (BioCAS)*, Turin, Italy, 2017, pp. 1–4.

[200] P. Motto Ros, A. Sanginario, M. Crepaldi, and D. Demarchi, "Quality-energy trade-off and bio-inspired electronic systems," in *2018 IEEE International Conference on the Science of Electrical Engineering in Israel (ICSEE)*, Eilat, Israel, 2018, pp. 1–5.

[201] A. Damilano, P. Motto Ros, A. Sanginario, A. Chiolerio, S. Bocchini, I. Roppolo, C. F. Pirri, S. Carrara, D. Demarchi, and M. Crepaldi, "A robust capacitive digital read-out circuit for a scalable tactile skin," *IEEE Sensors Journal*, vol. 17, no. 9, pp. 2682–2695, 2017.

[202] O. L. Nuzumlali, "Detailed noise analysis of current-to-frequency converters for precision analog accelerometers," in *2016 IEEE/ION Position, Location and Navigation Symposium (PLANS)*, Savannah, Georgia, USA, 2016, pp. 898–904.

[203] N. V. Kirianaki, S. Y. Yurish, N. O. Shpak, and V. P. Deynega, *Signal Processing in Quasi-Digital Smart Sensors*. John Wiley & Sons, Ltd, 2002, ch. 6, pp. 129–142.

[204] P. Motto Ros, M. Crepaldi, A. Bonanno, and D. Demarchi, "Wireless multichannel quasi-digital tactile sensing glove-based system," in *2013 Euromicro Conference on Digital System Design (DSD)*, Los Alamitos, CA, USA, 2013, pp. 673–680.

[205] M. Crepaldi, M. Stoppa, P. Motto Ros, and D. Demarchi, "An analog-mode impulse radio system for ultra-low power short-range audio streaming," *IEEE Transactions on Circuits and Systems I: Regular Papers*, vol. 62, no. 12, pp. 2886–2897, 2015.

[206] H. S. Narula and J. G. Harris, "A time-based VLSI potentiostat for ion current measurements," *IEEE Sensors Journal*, vol. 6, no. 2, pp. 239–247, 2006.

[207] S. Sapienza, M. Crepaldi, P. Motto Ros, A. Bonanno, and D. Demarchi, "On integration and validation of a very low complexity ATC UWB system for muscle force transmission," *IEEE Transactions on Biomedical Circuits and Systems*, vol. 10, no. 2, pp. 497–506, 2015.

[208] H. Khouadja, H. Arnous, K. Tarmiz, D. Beletaifa, A. Brahim, W. Brahem, J. Sakhri, and K. B. Jazia, "Pain on injection of propofol: efficacy of paracetamol and lidocaine," *Open Journal of Anesthesiology*, vol. 2014, 2014.

[209] M. M. Ahmadi and G. A. Jullien, "Current-mirror-based potentiostats for three-electrode amperometric electrochemical sensors," *IEEE Transactions on Circuits and Systems I: Regular Papers*, vol. 56, no. 7, pp. 1339–1348, 2008.

[210] N. Qiao and G. Indiveri, "An auto-scaling wide dynamic range current to frequency converter for real-time monitoring of signals in neuromorphic systems," in *2016 IEEE Biomedical Circuits and Systems Conference (BioCAS)*, Shanghai, China, 2016, pp. 160–163.

[211] MiNES Group, *Anaesthetics Monitoring Pen Demo*, Youtube, [Online]. Available: https://youtu.be/7JL_vAfjIrY.

[212] Nordic® Semiconductor, *nRF52840 Product Specification, v1.1*, accessed on: 4 June 2019. [Online]. Available: https://infocenter.nordicsemi.com/pdf/nRF52840_PS_v1.1.pdf.

[213] F. Rossi, P. Motto Ros, R. M. Rosales, and D. Demarchi, "Embedded biomimetic system for functional electrical stimulation controlled by event-driven sEMG," *Sensors*, vol. 20, no. 5, p. 1535, 2020.

[214] D. Tunzi, "Portable embedded system for continuous monitoring of anaesthetics," Master's thesis, Politecnico di Torino, Turin, Italy, 2019.

[215] SEGGER Microcontroller GmbH, *SEGGER Embedded Studio for ARM*, accessed on: 1 May 2019. [Online]. Available: https://studio.segger.com/home.htm.

[216] MiNES, *Micro and Nano Electronic Systems (MiNES) website*, accessed on: 11 Jan 2021. [Online]. Available: http://mines.polito.it.